EarthArXiv preprint

Satellite Embeddings: A Review

Longhao Wang

Key Laboratory of Water Cycle and Related Land Surface Processes, Institute of Geographic Sciences and Natural Resources Research, Chinese Academy of Sciences, Beijing 100101, China

University of Chinese Academy of Sciences, Beijing 100049, China

Correspondence: wanglonghao0857@igsnrr.ac.cn

ORCID: https://orcid.org/0000-0002-4642-4701

Peer review status

This manuscript is a non-peer-reviewed preprint submitted to EarthArXiv.

This version has not been accepted for publication in a peer-reviewed journal.

Journal submission status: This version has not yet been submitted to a peer-reviewed journal.

Version date: 18 October 2026

Satellite Embeddings: A Review

Longhao Wang

Key Laboratory of Water Cycle and Related Land Surface Processes, Institute of Geographic Sciences and Natural Resources Research, Chinese Academy of Sciences, Beijing 100101, China

University of Chinese Academy of Sciences, Beijing 100049, China

Corresponding author: wanglonghao0857@igsnrr.ac.cn

Abstract

Earth observation satellites acquire vast multi-sensor archives, but translating them into reliable environmental maps remains constrained by scarce field labels, sensor heterogeneity, and processing costs. Foundation models alleviate these bottlenecks by learning transferable representations, enabling reusable feature spaces termed satellite embeddings. Beyond traditional model weights, these representations are increasingly distributed as coordinate-based location encoders and precomputed global embedding products. Existing surveys primarily examine model architectures and pretraining objectives; operational geographic reuse also demands rigorous attention to spatial and temporal support, access contracts, and condition-controlled baseline comparisons. This review provides a structured critical synthesis and empirical evaluation of satellite embeddings for environmental mapping. We introduce a release-based taxonomy separating image encoders, location encoders, and precomputed embedding products, characterized across orthogonal facets of inputs, learning signals, and deployment attributes. Experimentally, we conduct a two-tiered evaluation across a global multi-target benchmark against matched classical baselines and a localized Wuhan case study probing spatial granularity and native-grid readouts, complemented by analyses of representation geometry and computational efficiency. Results reveal that while foundation representations achieve substantial gains for specific targets, their advantages are strongly conditioned on baseline strength, readout capacity, and geographic domain shift, with location encoders providing regional context rather than real-time spectral observations. Finally, we synthesize key challenges in spatio-temporal alignment, label independence, and lifecycle maintenance for operational Earth observation workflows.

Keywords

Satellite embeddings; Earth observation; Remote sensing foundation models; Representation learning; Geospatial benchmarks; Model evaluation

Highlights

- A release-based taxonomy separates encoders from precomputed embedding products.
- Fifteen image encoders and SatCLIP are tested against six baseline variants.
- Global cohorts contain 4,409 single-scene and 3,014 monthly-series locations.
- Baseline gains vary with target, readout, label budget and geographic holdout.
- Wuhan controls separate local split sensitivity from independent transfer.

1. Introduction

Environmental mapping requires features that remain useful when the target, region or available labels change. A land-cover classifier, a biomass estimator and a flood map can use related satellite observations, yet each asks a different question of those observations. Land-cover classes summarize surface composition, biomass requires information about vegetation structure, and flood mapping depends on when water was observed. These differences make representation reuse an empirical question. A compact feature vector is useful only if it retains the information needed at the spatial and temporal support of the intended prediction. For users, the relevant outcome is a defensible environmental estimate with an affordable and reproducible workflow.

Satellite embeddings offer reusable features for these mapping problems. Open satellite constellations and long-running archives have made it possible to pretrain encoders on data volumes that are much larger than the labelled datasets used for any one mapping task. Self-supervised, multimodal, temporal, and vision–language methods now expose reusable features in addition to task heads, while product providers increasingly distribute spatially indexed embedding layers that can be queried without rerunning a large encoder (Brown et al., 2025; Fang et al., 2026; Feng, Atzberger, et al., 2026; Huang et al., 2025; Huo et al., 2025; Klemmer et al., 2026; Lu et al., 2025; Xiao et al., 2025; Zhu et al., 2026). Their usefulness depends on which observations they summarize and how the resulting features can be reused.

The distinction matters because two objects called an “embedding” can retain different information. A pooled vector, a dense token grid, a coordinate representation, and an annual feature field differ in spatial support, temporal meaning, and access path. The same encoder can produce different objects after pooling, temporal aggregation, quantization, or modality routing. Conversely, systems trained with different objectives can expose similar downstream interfaces. Existing remote-sensing foundation-model surveys organize architectures,

pretraining, and downstream tasks (Huang et al., 2025; Huo et al., 2025; Lu et al., 2025; Xiao et al., 2025; Zhou et al., 2025). Product-oriented work further identifies incompatible formats, resolutions, and access interfaces as barriers to reuse (Fang et al., 2026). Building on these accounts, this review makes version, support, access, update, and fixed-feature evaluation explicit selection criteria for a geographic workflow (Francis & Czerkawski, 2024; Gomes et al., 2025; Klemmer et al., 2025; R. Ramachandran et al., 2025).

An embedding-centred review must also preserve the longer history of remote sensing representation learning. Hand-crafted indices and texture descriptors were followed by transferable convolutional features, seasonal and contrastive pretraining, masked image modelling, and modality-aware transformers (Bazi et al., 2021; Castelluccio et al., 2015; C. Cheng et al., 2026; Cong et al., 2022; Dosovitskiy et al., 2021; Hong et al., 2024; Jean et al., 2019; Mañas et al., 2021; Noman et al., 2024; Reed et al., 2023). Recent systems extend this line with wavelength-conditioned inputs, multimodal or temporal routing, image–text alignment, and precomputed products (Astruc et al., 2025; H. Bi et al., 2026; Brown et al., 2025; Feng, Atzberger, et al., 2026; Fuller et al., 2023; Jakubik et al., 2023; X. Li et al., 2026; Liu et al., 2024; Szwarcman et al., 2026; Tseng et al., 2025; Wang et al., 2023; Wang, Xiong, et al., 2025; Xiong et al., 2024). These developments are not a single mutually exclusive family tree. They are design choices that can be combined, omitted, or exposed through different deployment forms.

The move from task-specific models to reusable features also changes where decisions are made. With an image encoder, users choose observations and reproduce the released preprocessing and extraction procedure. With a location encoder, they query a learned function of geographic position. With a precomputed product, they inherit the provider's observation window, grid and feature definition. Each route can reduce repeated work, but each exposes different controls over the information supplied to a downstream model. The

practical comparison therefore starts with the delivered representation and its documented use, before considering model size or the name of a pretraining method. This motivates the release taxonomy used throughout this review.

Evaluation must then distinguish predictive information from the conditions that make it accessible. A frozen linear probe asks what a simple readout can recover; a nonlinear readout asks a different question. A gain over raw observations may change with the label budget or geographic split, and a strong score against a reference map may partly reflect shared source information. Comparisons also become ambiguous when one representation summarizes a year of observations and another sees a single image. Matching locations alone cannot resolve these differences. We therefore connect the literature review to explicit tests of baseline-relative gain, readout sensitivity, spatial support and geographic transfer, while keeping reference-product prediction separate from independent environmental validation.

Global and local evidence play complementary roles in this design. Geographically distributed samples test whether observed advantages persist across environmental settings and held-out regions. A local window makes spatial structure, mixed land cover and sensitivity to neighbouring training samples easier to examine. The two settings cannot be pooled into one ranking when their inputs, labels and extraction procedures differ. Our global experiment therefore provides the controlled comparisons, while the historical Wuhan case illustrates local representation and readout behaviour under its recorded conditions. This division allows the review to address practical selection questions without treating local interpolation as independent geographic replication.

The paper makes two contributions. First, it provides a structured critical synthesis of reusable Earth-observation representations, organized by release object, model facets and deployment attributes. The 20-entry rs-embed catalogue is an executable subset of the literature. Second, it tests fifteen frozen image encoders within controlled input subgroups

against six classical baseline variants and evaluates one coordinate-only location encoder on the same cohorts, using 4,409 annual single-scene and 3,014 monthly-composite locations. The completed benchmark spans reference targets, geographic holdouts, readouts, feature dimensions, label budgets and footprint supports. Four product or coarse systems remain explicitly unavailable where equivalent input controls cannot be established. A complementary 567-tile Wuhan case retains its historical local comparisons and support limitations. Independent dense validation and future-year transfer are outside the evidence provided here. This distinction connects reusable representations with the requirements of maintained geospatial products (Cui et al., 2026; Fang et al., 2026; Klemmer et al., 2026).

Section 2 introduces the review methods, embedding concepts and release taxonomy. Section 3 examines models, representation mechanisms and benchmarks. Section 4 connects task requirements and evidence quality to the evaluation design, and Section 5 presents the global experiments and Wuhan case study. Section 6 discusses remaining challenges and research priorities, followed by the conclusion in Section 7. The Supplementary Material provides detailed methods, historical diagnostics and source records.

2. Foundations

2.1 Review methods

The review asks five linked questions: which reusable representations are available; how their release objects, inputs and support differ; how utility has been evaluated; which forms of dependence, transfer and deployment limit the evidence; and what records are needed for fair comparison. These questions distinguish the literature synthesis from the executable benchmark subset.

This structured critical review addresses these questions through reproducible capped searches and purposive synthesis. Reports are the evidence units, linked to their models,

checkpoints and products. We assess conditions supporting environmental and deployment claims, without estimating field-wide prevalence or ranking all representations.

The cutoff for the frozen discovery and screening route is 31 August 2026. A separate descriptive bibliographic snapshot was frozen on 7 October 2026; later purposive source checks and citation additions are documented separately and are not included in the frozen screening denominators. The discovery expression combines Earth-observation terms with reusable-representation terms:

(remote sensing OR Earth observation OR satellite OR geospatial) AND (foundation model OR pretrained model OR self-supervised representation OR representation learning OR embedding OR vision-language model OR masked autoencoder).

Provider-native queries, responses, dates and deduplication rules are archived in Supplementary Methods S2. Crossref, partial OpenAlex searches, the existing corpus and citation leads remain distinct discovery routes. Broad queries did not primarily use model names. Scopus and Web of Science exports were unavailable; ranking caps and unresolved retrievals preclude systematic coverage or source-saturation claims.

After duplicate/version reconciliation, Crossref yielded 1,911 candidates; 587 required retrieval, with 45 verified local PDFs and 542 unresolved. These are route counts, not independently verified study counts. Scale-MAE, Galileo and FoMo used a separate discovery route. Sixteen completed OpenAlex queries added 512 provider-deduplicated metadata leads without changing frozen Crossref decisions or full-text counts. Supplementary Methods S2 records the route-specific screening and source-independence distinctions. Figure 1 summarizes these distinct screening and retrieval routes.

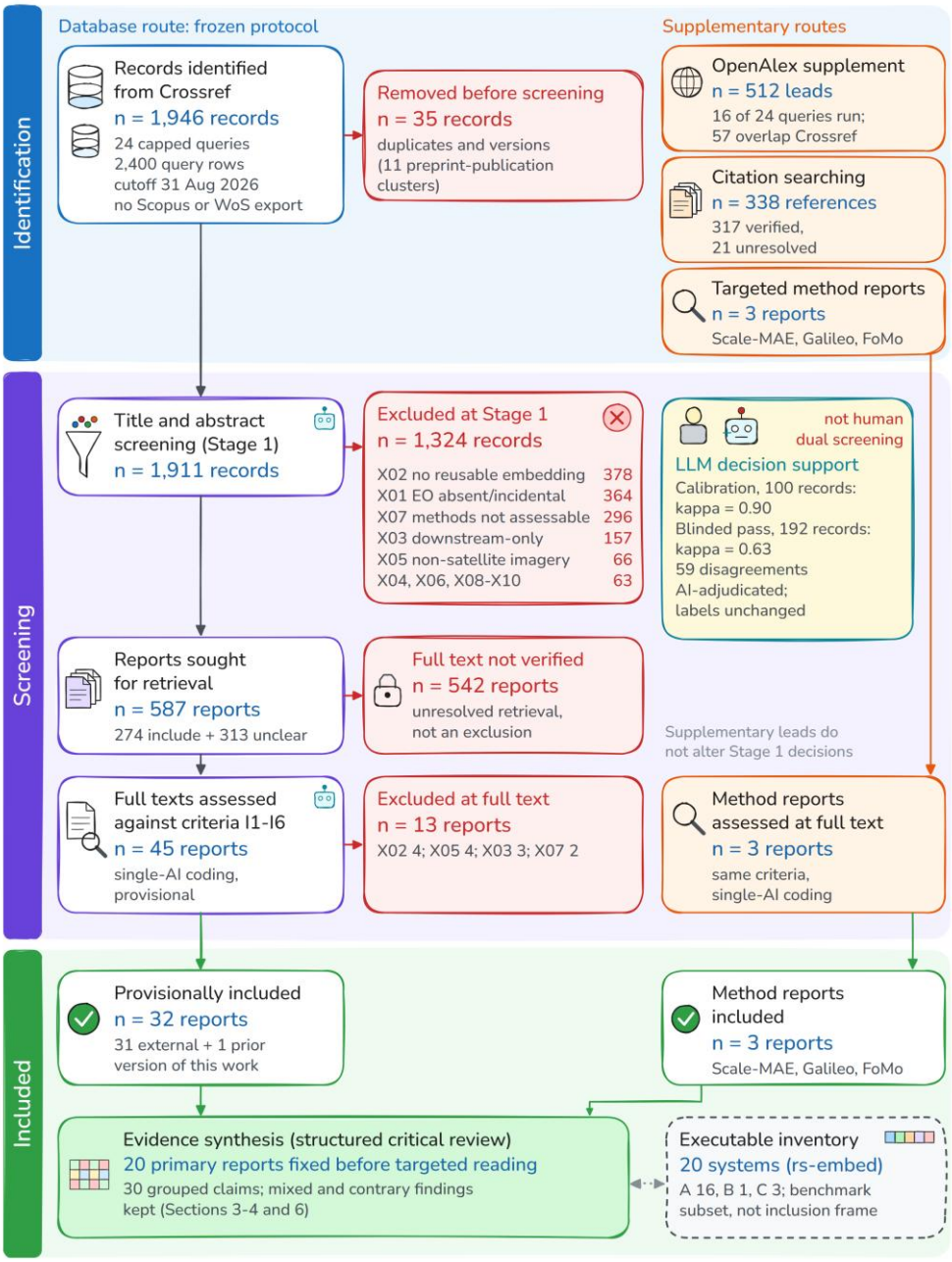


Figure 1. PRISMA 2020-style flow of literature identification, screening and provisional inclusion (literature cutoff 31 August 2026). The frozen database route (24 capped Crossref queries) is separated from supplementary citation leads (OpenAlex metadata and backward citation searching) and from targeted method reports; the leads did not alter frozen Stage 1 decisions. The 542 reports without verified full text are unresolved retrievals, not scientific exclusions. Robot icons mark AI-assisted steps; these decision-support passes (kappa = 0.90 on 100 calibration records and 0.63 on a 192-record blinded second pass, with 59 AI-adjudicated disagreements) are not independent human dual screening. Scopus and Web of Science exports were unavailable, so the counts describe capped

discovery routes rather than systematic coverage or study-level PRISMA totals. Exclusion codes X01-X10 are defined in Supplementary Methods S2. The 20-system rs-embed inventory is a benchmark subset selected for executability, not the inclusion frame. Icons are schematic. Diagram construction used AI-assisted coding with OpenAI Codex and Anthropic Claude Code (October 2026 workflow); the editable artwork and provenance are retained.

Eligible primary reports introduce, distribute or independently evaluate reusable learned representations central to satellite Earth observation, with identifiable construction, access or evaluation. Coordinate representations require an explicit Earth-observation application. Cutoff-bound counts require public availability by the cutoff. Reviews, perspectives and interface documentation are distinguished from primary evidence; reviews cannot independently corroborate their cited studies. Failed retrieval remains unresolved, not a scientific exclusion.

Purposive cases contrast observations with supervision, fixed features with adaptation, annual with acquisition-level support, output spacing with effective support, and environmental observations with map labels. They require assessable primary sources and include mixed or contrary findings. They are not a representative field sample. Repository support does not determine eligibility; the 20-entry executable inventory is a separate subset.

Twenty primary reports were selected for a focused challenge of the central comparisons in Sections 3 and 4. Their assessed versions were checked for the target, comparator, validation design and limitations supporting each comparison, alongside selected contrary evidence and citation leads. This purposive reading supplements the capped discovery routes; it neither resolves the remaining retrieval queue nor establishes source saturation. The retained reef preprint under its original title is used as a purposive application case and is not added retrospectively to the frozen database counts.

Extraction records assessed versions, training/inference inputs, support, geometry, adaptation, targets, splits, baselines, uncertainty, access and conflicts. Provenance

distinguishes reported_primary, reported_official, verified_artifact, derived, secondary and unknown. Model releases, report revisions and delivered products remain separate; a matching title or current webpage does not establish assessed-version identity.

The claim matrix links primary passages to tasks, geography, targets, comparators, adaptation and uncertainty. Fold variation, seed dispersion and geographic confidence intervals are distinguished. Unmatched observations, support, label ancestry or adaptation preclude pooled rankings. Missing details restrict claims; mixed and negative findings remain visible. Proposed evaluation rules are identified separately from cited empirical findings.

Screening, extraction and claim checks were AI-assisted. Blinded repeated LLM assessments and separate AI checks provide a diagnostic record, not independent human dual screening or experimental replication. Historical quality scores were not used to weight effects or estimate field-wide evidence quality. Retrieval availability, search ranking and purposive selection constrain the review's coverage. Supplementary Methods S2 records the screening, agreement, version and challenge procedures.

2.2 Embedding concepts

We use *satellite embedding* for a learned representation intended or demonstrated to support reuse beyond a single task head and sample set. Reuse may involve transfer, retrieval, prompting, reconstruction or a released geospatial product. The term includes pooled vectors, dense token grids, temporal sequences, coordinate-linked representations and precomputed layers. It excludes task-specific logits, hand-crafted indices and an ordinary classifier backbone without evidence of representation reuse (Cui et al., 2026; Fang et al., 2026; Stewart et al., 2026). A documented interface and explicit spatial and temporal support determine whether a representation can be deployed or compared under a given contract. Missing documentation is retained as unknown and limits that comparison; it does not by itself exclude an otherwise eligible report.

Table 1. Entity vocabulary used for screening and synthesis. A study may link to several model entities and releases; an embedding product is not synonymous with the encoder that generated it.

Entity	Operational meaning
Study/report	Scholarly or technical work that reports a method, product, benchmark, or application.
Model family	Named lineage containing architectures, checkpoints, products, papers, or releases.
Encoder/checkpoint	Executable parameters and preprocessing that transform imagery or coordinates into a reusable representation.
Representation/embedding	Vector, token grid, feature map, or sequence emitted for reuse before distribution packaging.
Embedding dataset	Finite released vectors tied to samples and metadata; sampled embedding collections belong to product class C2.
Embedding product	Spatially indexed precomputed vectors distributed as gridded fields (C1) or sampled collections (C2), with version and support records.
Service/client	Access mechanism, API, or catalogue; not a representation method by itself.
Downstream artifact	Probe, decoder, index, prediction map, or retrieval database built from an embedding.

Pooled encoder outputs require documented extraction and reuse. Dense products remain products when their generators are unavailable; location encoders require explicit Earth-observation roles and evaluation. Products retain independent version, support, quantization, update, access and licence records (Czerkawski et al., 2024; Fang et al., 2026; Francis & Czerkawski, 2024).

Figure 2 contrasts checkpoint inference with precomputed products. Release classes describe the delivered object; model facets describe its support.

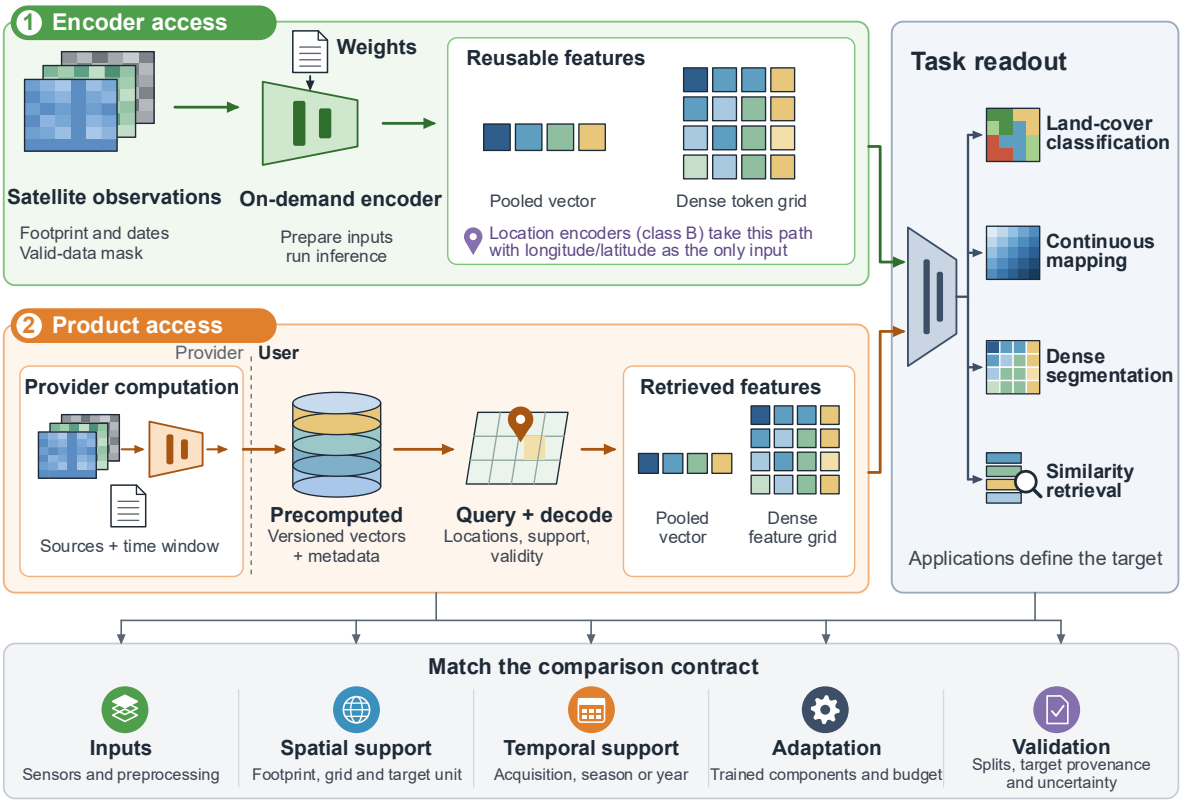


Figure 2. Two access paths from Earth observations to reusable representations and downstream applications. (1) On-demand inference requires observations, preprocessing and model weights; (2) a precomputed product exposes provider-generated features through a versioned query and decoding interface. Location encoders (class B) follow path 1 with longitude and latitude as the only query input. Input information, spatial and temporal support, adaptation, and validation define the comparison conditions; sharing a readout alone does not make the two paths equivalent. The depicted features and maps are schematic vector artwork and contain no measured or predicted research data. Diagram construction used AI-assisted coding with OpenAI Codex and Anthropic Claude Code (October 2026 workflow); the editable artwork and provenance are retained.

2.3 Release taxonomy

We classify each release by what the user receives and must supply. Class A, image encoders, delivers model weights: the user supplies satellite pixels (RGB, multispectral or time series) and runs inference. Class B, location encoders, delivers a lightweight network that maps longitude and latitude to a vector without query-time imagery. Class C,

precomputed embedding products, delivers spatially indexed vectors retrieved by bounding-box or point query. Image encoders are subdivided by the input contract of the evaluated configuration into RGB (A1), fixed-schema multispectral (A2), channel-adaptive (A3) and multitemporal sequence (A4) encoders; the temporal contract takes precedence. Products are subdivided by spatial completeness into gridded embedding fields (C1) and sampled tile, chip or patch collections (C2); temporal indexing is recorded as a facet. A model lineage may expose several releases in different classes. Four orthogonal facets describe inference modality, learning signal, temporal support, and spatial support with output geometry; pretraining modality is recorded separately. Adaptation and access or governance are deployment attributes. Unknown or unreported values remain explicit. These descriptors connect the release taxonomy to recent multimodal surveys and foundation-model capability benchmarks (Hong et al., 2026; Yang et al., 2025; Zhu et al., 2026).

Table 2. Evidence-coded descriptors used in the model/product dossier. Input, learning signal, temporal support, and spatial support with output geometry are model facets; adaptation and access describe deployment. Nominal resolution, receptive footprint, and output spacing are recorded separately.

Axis	Values recorded and interpretation
Release object	A image encoder weights; B location-encoder network; C precomputed embedding products, comprising C1 gridded fields and C2 sampled collections. A hosted service is an access mechanism, not a release class.
Input modality	RGB, multispectral, hyperspectral, SAR, LiDAR/height, elevation, climate/weather, coordinates/vector context, text/metadata; inputs used in pretraining are separated from inputs required at inference.
Learning signal	Masked reconstruction; contrastive or cross-view alignment; distillation or representation prediction; generative token/modality prediction; image–text alignment; supervised; fixed/random; or hybrid objective.
Temporal support	Single acquisition, paired/seasonal views, fixed or variable time series, annual/seasonal composite, static product, or temporally queryable product; supported inference years are explicit.
Spatial support	Native ground sampling distance, receptive footprint, output stride/cell, support unit, geographic coverage, projection/grid, and edge or resampling behavior.

Axis	Values recorded and interpretation
Output geometry	Pooled vector, patch-token grid, dense raster, multiscale features, or shared image–text/location space; dimension, normalization, pooling, quantization, and compression are recorded.
Access/governance	Code, weights, data, API, and licence separately; authentication, quota, cost, coverage, update/deprecation, versioning, and offline-cache status.
Adaptation regime	Zero-shot retrieval, nearest neighbour, frozen probe, adapter/parameter-efficient tuning, full fine-tuning, dense decoder, or no published downstream adaptation.

Axis values are descriptors, not causal explanations. For example, a contrastive objective does not by itself establish better transfer, and a multimodal input contract does not guarantee robustness when one source is missing. Mechanistic interpretations require matched data and ablations (Doerksen & Kerner, 2026; X. Li et al., 2025; Simumba et al., 2026).

Figure 3 characterizes the embedding literature through title terms, release relationships and cumulative growth with representative releases. Its merged bibliographic corpus is broader than the cutoff-bound screened evidence. Figure 4 organizes the review by the three release classes and places representative releases on a timeline; the facets and deployment attributes remain distinct from that primary classification.

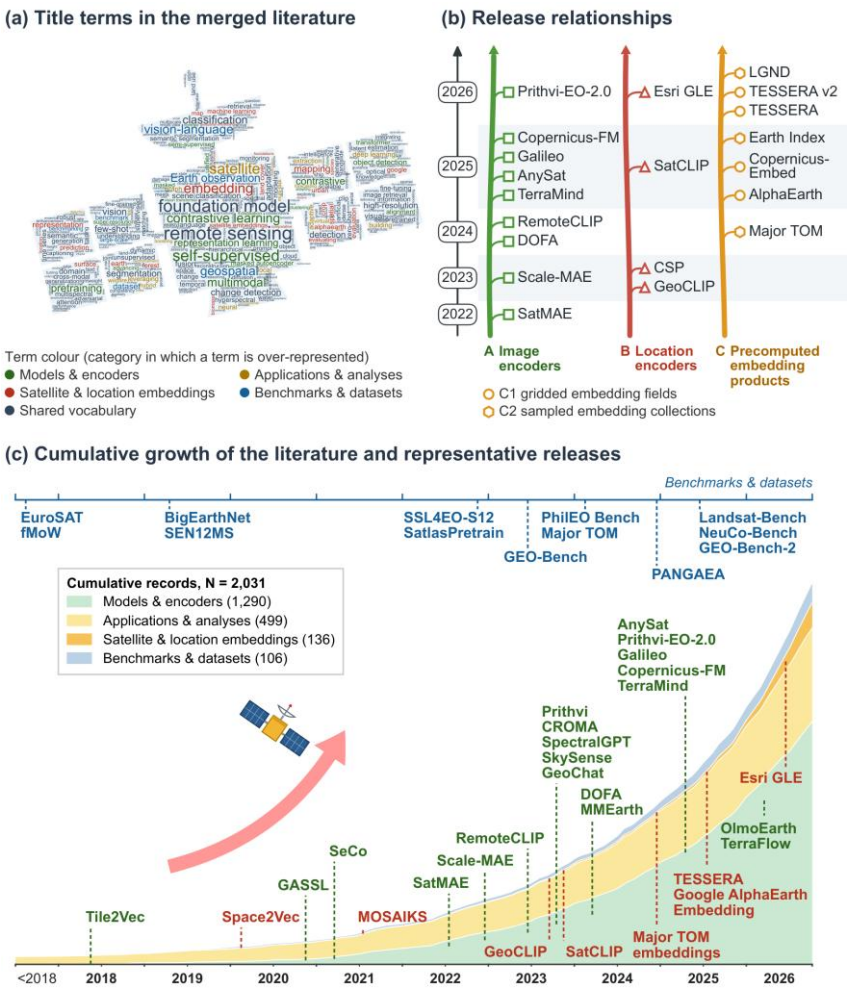


Figure 3. Bibliometric overview of the embedding literature, captured on 7 October 2026. The corpus merges the Zotero AI/Embedding collection (400 records), the reference list of Cui et al. (335 titled references) and an OpenAlex title query for remote-sensing foundation models, embeddings, self-supervised pretraining, location encoders and vision-language models (2018 to 7 October 2026). Records were deduplicated by normalized title, leaving 2,032 records, 2,031 of them dated. (a) Title word cloud in a satellite silhouette. Text size is the number of titles containing each normalized term; a few long or very frequent terms that cannot fit the silhouette at that size are drawn smaller, so size ranks are approximate at the top. Colour marks the category in which a term is clearly over-represented; other terms are shown as shared vocabulary. The silhouette is decorative. (b) Nineteen selected model and product records plus the Esri Global Location Encoder (Esri GLE; ArcGIS release, June 2026), by release class (A, image encoders; B, location encoders; C, precomputed embedding products, with circles for C1 gridded embedding fields and hexagons for C2 sampled embedding

collections) and Zotero record year. Years follow the Zotero metadata rather than independently established first-release dates (Esri GLE: first public release year); records within a year are stacked for legibility, so vertical spacing is not to scale. Lane colours follow the category colours of (a) and (c); branches group releases and do not denote inheritance or citation. (c) Cumulative records by first-release month, stacked by a lexical title classification: models and encoders (1,290), applications and analyses (499), satellite and location embeddings (136), and benchmarks and datasets (106). Dates come from arXiv identifiers where available, then from Crossref, Zotero or OpenAlex. Year-only dates (604 records) are spread evenly within their year, and records before 2018 enter at the origin. Labelled releases have verified first-release months. Dashed leaders mark the release month; stacked names were released within five months of it. Benchmarks hang from the top axis. The arrow and satellite icon are decorative. 2026 is partial through 7 October. The counts describe this merged corpus. They do not measure the size of the field, citation influence or a systematic-screening yield.

2.4 Comparison principles

Five proposed comparison cells draw on capability evaluation (Simumba et al., 2026) and GEO-Bench (Lacoste et al., 2023). The encoder-observation cell matches encoder observations, footprint, time window, locations and probe budgets, while recording checkpoint-specific normalization, outputs and pooling. The product cell matches products by location, target year, native-support aggregation and missingness policy. The baseline cell supplies raw observations, PCA, indices or spatial controls with the encoder-observation cell's splits and budgets. The dense-output cell aligns dense outputs and target resolution. The operational-cost cell measures latency, bytes, VRAM, requests, failures and temporal flexibility under common accounting. Our experiments populate a restricted encoder–control comparison and execution measurements, not every cell; cross-cell ranks do not establish superiority.

Every model–target pair carries dependence flags for any target or source family used in pretraining, pseudo-label overlap, temporal/geographic overlap, related supervised signals,

and target-as-input cases. A flagged pair can be useful for measuring information retention or product reuse, but it is not treated as independent transfer evidence (Doerksen & Kerner, 2026; Plas et al., 2026).

3. Models and Benchmarks

The source-linked cases organize this synthesis by release object (Figure 4). The 20 rs-embed model identifiers, comprising 16 image encoders, one location encoder (SatCLIP) and three products, form an executable subset; repository support does not determine review inclusion. Each release has one primary class, while studies and model lineages can connect multiple checkpoints, representations and products.

The release taxonomy describes the object available to users, not an architectural family. One model lineage can supply both an executable checkpoint and a precomputed product, while similar interfaces can expose representations built by different mechanisms. The A1-A4 and C1-C2 subclasses refine input contract and spatial completeness within their respective release classes. Separate technical descriptors record tokenization, metadata encoding, backbone topology, spatial and temporal interaction, modality fusion, learning objectives and exported feature geometry. Architectural and training claims refer to identified configurations and versions, rather than being inferred from a release class or model name.

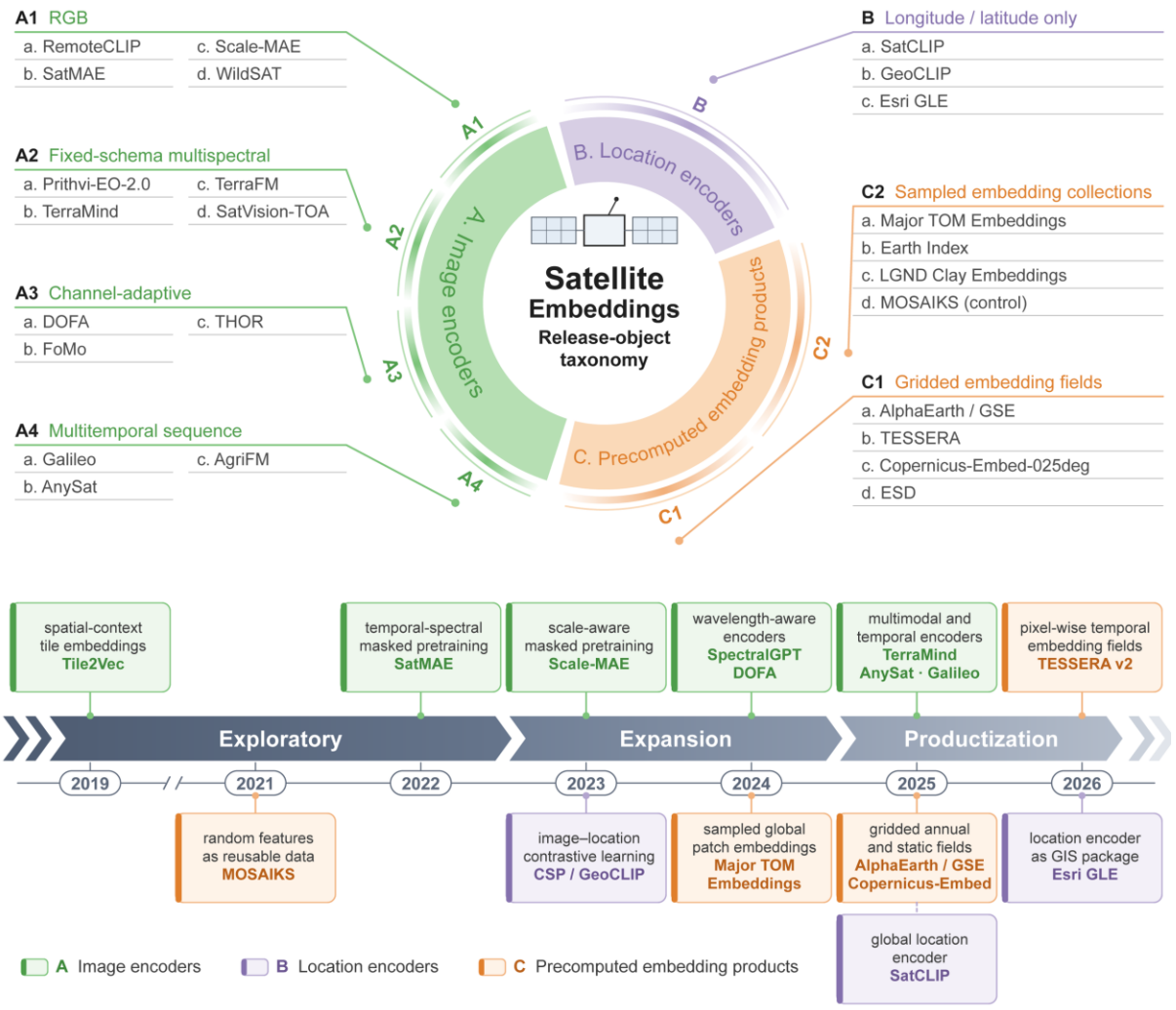


Figure 4. Review overview organized by the object delivered to users, with representative releases on a 2019–2026 timeline. A, image encoders expose weights for on-demand inference and are subdivided by the evaluated input contract: A1 RGB, A2 fixed-schema multispectral, A3 channel-adaptive and A4 multitemporal sequence. B, location encoders return representations from longitude and latitude without query-time imagery. C, precomputed embedding products are distributed as gridded embedding fields (C1) or sampled embedding collections (C2). Callouts list the exemplars assigned in the frozen release taxonomy; MOSAIKS is a non-learned control. Timeline cards are coloured by release class and dated by formal publication year or, for releases without a paper, first public release year. Columns are equally spaced; 2020, with no selected release, is shown as an axis break. The exploratory, expansion and productization phases are descriptive groupings, not measured breakpoints. Inference input, learning signal, temporal support, and spatial support/output geometry are orthogonal facets. Classification applies to release objects; one model lineage can span multiple classes. Sector

and arc sizes are schematic, not publication shares. Diagram construction used AI-assisted coding with OpenAI Codex and Anthropic Claude Code (October 2026 workflow); the editable artwork and provenance are retained.

3.1 Model development

Remote-sensing representation learning progressed from spectral and texture descriptors through transferable convolutional features, temporal and masked-image self-supervision, to multimodal, wavelength-aware, vision–language and productized systems (Astruc et al., 2025; Bazi et al., 2021; Brown et al., 2025; Castelluccio et al., 2015; Cong et al., 2022; Dosovitskiy et al., 2021; Feng, Atzberger, et al., 2026; Hong et al., 2024; Jakubik et al., 2023; Jean et al., 2019; Liu et al., 2024; Mañas et al., 2021; Noman et al., 2024; Reed et al., 2023; Szwarcman et al., 2026; Tseng et al., 2025; Wang et al., 2023; Wang, Xiong, et al., 2025; Xiong et al., 2024). Chronology is not a taxonomy: multimodal encoders can use masked reconstruction, specialized models general objectives, and products any encoder. The primary classes describe release objects. Model facets record inputs, learning signals, temporal support, spatial support and output geometry; adaptation and access remain deployment attributes. Dossier provenance and evidence grades distinguish reported facts from inferred mechanisms.

Within this progression, self-supervised objectives exploited geographic and temporal structure through geography-aware contrastive pairs (Ayush et al., 2021) and change-aware sampling (Mall et al., 2023). Later encoders widened sensor and temporal coverage: USat models bands with different ground sampling distances from several sensors (Irvin et al., 2023), SkySense factorizes optical and SAR spatiotemporal sequences (Guo et al., 2024), Presto encodes pixel time series with a lightweight transformer (Tseng et al., 2023), MMEarth explores multimodal pretext tasks (Nedungadi et al., 2025), TerraMind pretrains an any-to-any generative model over nine geospatial modalities (Jakubik et al., 2025), TerraFM fuses Sentinel-1 and Sentinel-2 through modality-specific patch embeddings (Danish et al.,

2026), and OlmoEarth and TerraFlow target multimodal, multitemporal learning (Herzog et al., 2026; Puriy et al., 2026). Supervision broadened in parallel: WildSAT aligns imagery with wildlife observations (Daroya et al., 2025), GeoChat and RS5M couple imagery with language (Kuckreja et al., 2024; Zhang et al., 2024), and DiffusionSat adds generative pretraining for satellite imagery (Khanna et al., 2024). Evaluation resources moved from large labelled archives such as BigEarthNet and SatlasPretrain (Bastani et al., 2023; Sumbul et al., 2019) to foundation-model benchmarks, including PhilEO Bench, Landsat-Bench and NeuCo-Bench (Corley et al., 2025; Fibaek et al., 2024; Vinge et al., 2026). Position papers and syntheses frame these developments from complementary perspectives (Dalei et al., 2025; Lane & Karimzadeh, 2026; Mai et al., 2024; Rolf et al., 2024, 2025; Tuia et al., 2020).

Figure 5 summarizes the thematic and collaborative structure of the 400-record collection with keyword co-occurrence and co-authorship networks. Communities describe shared vocabulary or co-authorship within this curated collection; they do not measure citation influence, study quality or model performance.

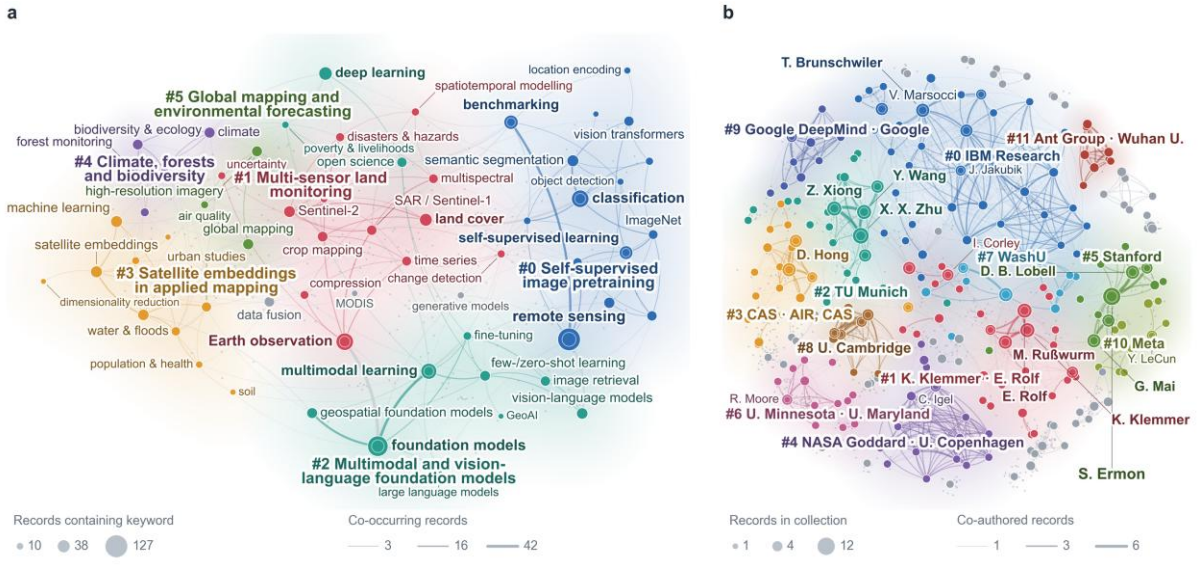
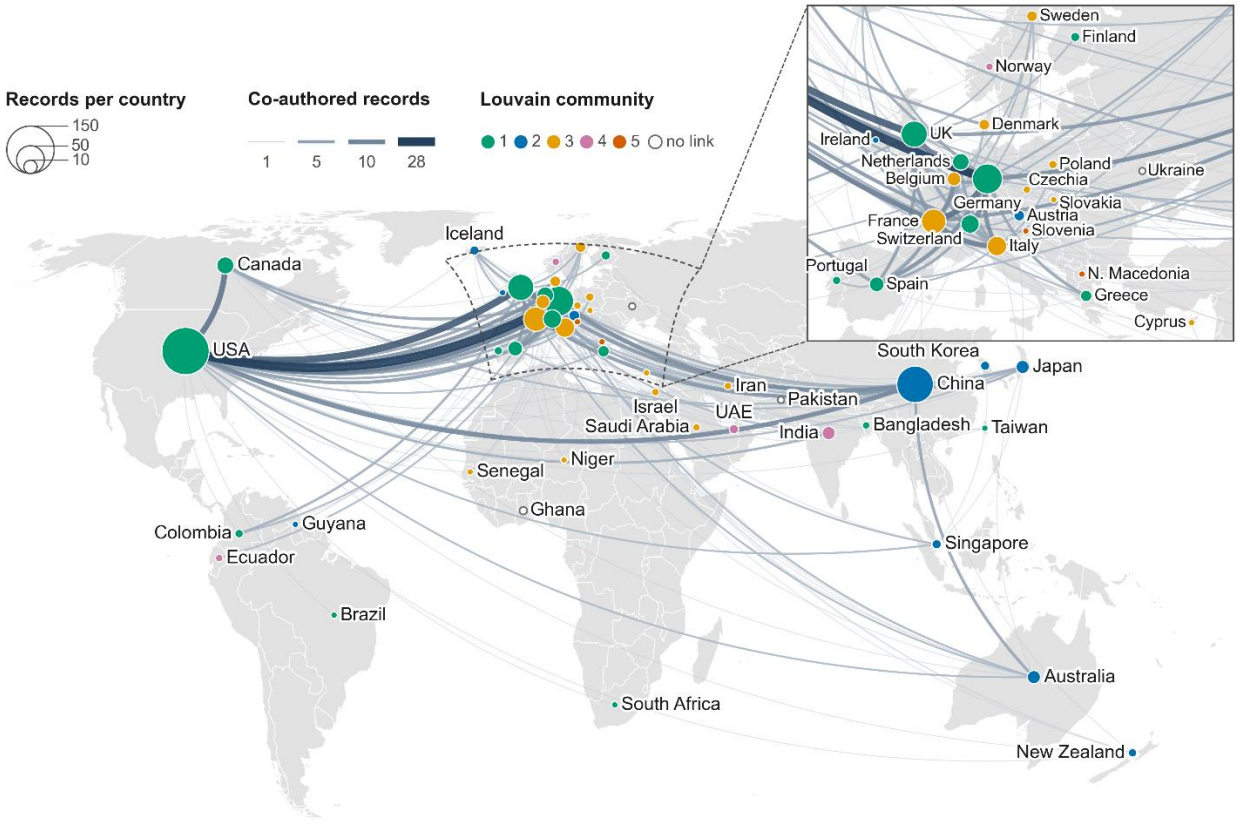


Figure 5. Keyword co-occurrence (a) and co-authorship (b) networks of the 400-record Zotero AI/Embedding collection. (a) Keywords come from a controlled vocabulary of 74 terms with merged synonyms, matched in titles and, for the 183 records that have one, in the Zotero abstract; 354 records contain at least one term. Circles are the 63 keywords found in at least 5 records, with area

proportional to the number of records. Links form the network backbone: keyword pairs that co-occur in at least 3 records and are among each keyword's five strongest associations (association strength); line width shows the number of shared records. Small grey dots place each record at the inverse-frequency-weighted centroid of its keywords. Community names are descriptive labels written by the authors. Because abstracts are available for fewer than half of the records, keyword frequencies partly reflect metadata coverage. (b) Authorships come from OpenAlex author identifiers for 376 matched records. Circles are the 262 authors with at least 2 records, and links join co-authors, with width showing the number of shared records. Layout and communities use fractional counting (1/(n-1) per record with n authors) so that large-team papers do not dominate. Strong gravity brings the 24 disconnected components into one frame, so distances between unconnected groups carry no meaning. Each community is labelled with the institutions shared by at least 30% of its members, otherwise with its two most prolific authors. Small grey dots are the 906 co-authors who appear in only one record. In both panels, positions come from ForceAtlas2, colours and halos mark Louvain communities (seed 20261007), grey circles are members of small groups, and rings mark the most frequent nodes. Proximity reflects shared vocabulary or co-authorship within this curated collection, not citation, influence or field-wide collaboration.

Figure 6 adds the geographic distribution of international co-authorship within the same collection. Country affiliations are available for 351 of its 400 records; the map therefore describes the documented collaboration network of this curated snapshot, not field-wide participation or the geographic coverage of model training and evaluation.



404

405 **Figure 11.** International co-authorship network of the literature in the Zotero AI/Embedding
406 collection (Equal Earth projection), with the European sub-network enlarged in the inset (Lambert
407 azimuthal equal-area; same node scale as the main map). Countries are taken from the authors'
408 affiliations: OpenAlex institution metadata, plus the affiliations printed on the first page of the PDF
409 when OpenAlex had none. This covers 351 of the 400 records; most of the 49 records without a
410 country are web pages, datasets or items with no resolvable affiliation. Circle area shows how many
411 records include at least one author from that country (full counting; Hong Kong is counted with
412 China). Link width and shade show how many records were co-authored by both countries (1-28).
413 Colours show Louvain communities of the weighted country graph; hollow circles mark countries
414 with no international co-authorship in the collection. The network shows co-authorship only, not
415 citations or model lineage.

416

3.2 Inputs and support

Optical RGB and multispectral Sentinel-2, Landsat and harmonized archives provide repeated broad coverage. SAR adds all-weather backscatter and structure, with speckle, geometry and co-registration concerns. Hyperspectral or wavelength-conditioned encoders extend spectral coverage; coarse inputs such as MODIS change support before encoding. Elevation, canopy height, climate, coordinates, text and ecological observations used in pretraining or supervision are distinct from query inputs (H. Bi et al., 2026; Do et al., 2025; Fuller et al., 2023; Schmitt et al., 2019; Waldmann et al., 2025; Wang, Xiong, et al., 2025).

AgriFM pretrains on unpaired sensor streams with GLC_FCS30D land-cover fractions and teacher consistency: 25.24 million images form approximately 0.734 million temporal sequences (W. Li et al., 2026). This creates target-family dependence, without audited exact evaluation-label reuse. Crop classification also uses previous-year crop patterns; source and sequence-length comparisons do not test geographic exclusion. ALISE's source datacube is multimodal, but its assessed encoder uses only Sentinel-2 sequences (Dumeur et al., 2025).

AlphaEarth's reported inference uses Sentinel-2, Landsat 8/9 and Sentinel-1; elevation, GEDI relative heights, climate, land cover and text supply training targets (Brown et al., 2025). Its annual product uses v2.1, whereas main evaluations use v2.0; v2.1 adds USDA Cropland Data Layer targets through 2023 and changes inference sampling. Dependence is release-specific and alone does not prove leakage. Tessera v1 uses Sentinel-1 and Sentinel-2 temporal branches with self-supervision from independently sampled views of annual pixel series (Feng, Atzberger, et al., 2026). Its 10-m grid does not imply 10-m observations for every band. Pixel-series encoding and AlphaEarth's buffered spatial tiles provide different context despite equal output spacing.

Single acquisitions, irregular sequences and annual products require explicit dates and aggregation rules. ALISE's authors avoid the foundation-model designation: its irregular

Sentinel-2 sequences yield ten learned temporal features per pixel, not ten dates (Dumeur et al., 2025). The default 10×64 representation and trained linear readout differ from a pooled single-date adapter. European pretraining includes evaluation years; qualitative reconstruction does not establish forecasting, and larger temporal-view discrepancies can degrade performance. Annual products and other sequence encoders have distinct time semantics (Feng, Jaffer, et al., 2026; Qin et al., 2025; Szwarcman et al., 2026; Wang et al., 2023).

Native ground sampling distance, receptive footprint and output spacing are distinct. Pooling can enlarge a 10-m input's support; resampling a 1-km or 0.25-degree product cannot recover fine boundaries. Edge handling, projection, grid origin and categorical/continuous aggregation affect neighborhoods. The dossier distinguishes nominal from verified support: a common target grid does not equalize upstream information (Dumeur et al., 2025; Feng, Jaffer, et al., 2026; Simumba et al., 2026).

Quality masking, temporal compositing, and learned sequence aggregation perform different operations. Masking removes observations identified as invalid; compositing combines retained observations into a summary image; sequence encoding processes dated observations before producing features. Compositing can reduce contamination and sampling variability, but can also attenuate short events or obscure the timing of phenological transitions. An annual embedding generated from a dated sequence may retain aspects of seasonal dynamics and should not be equated with an embedding of an annual mean image. Nevertheless, an annual output does not by itself expose acquisition-level timing or guarantee that a downstream predictor can recover every transient event. Temporal support must therefore describe both the observations supplied to the generator and the information exposed by its output.

3.3 Architectures and objectives

3.3.1 Architectures

Satellite embedding systems do not share a single Transformer architecture. Even among Transformer-based models, the computational unit, attention structure, positional information and extraction layer differ. Architectural comparison must distinguish the backbone from input adapters, temporal aggregators, modality-fusion modules and training heads. Table 3 summarizes representative configurations across the release classes, and Figure 7 illustrates image encoders, a pixel time-series product generator, location encoders and the MOSAIKS control.

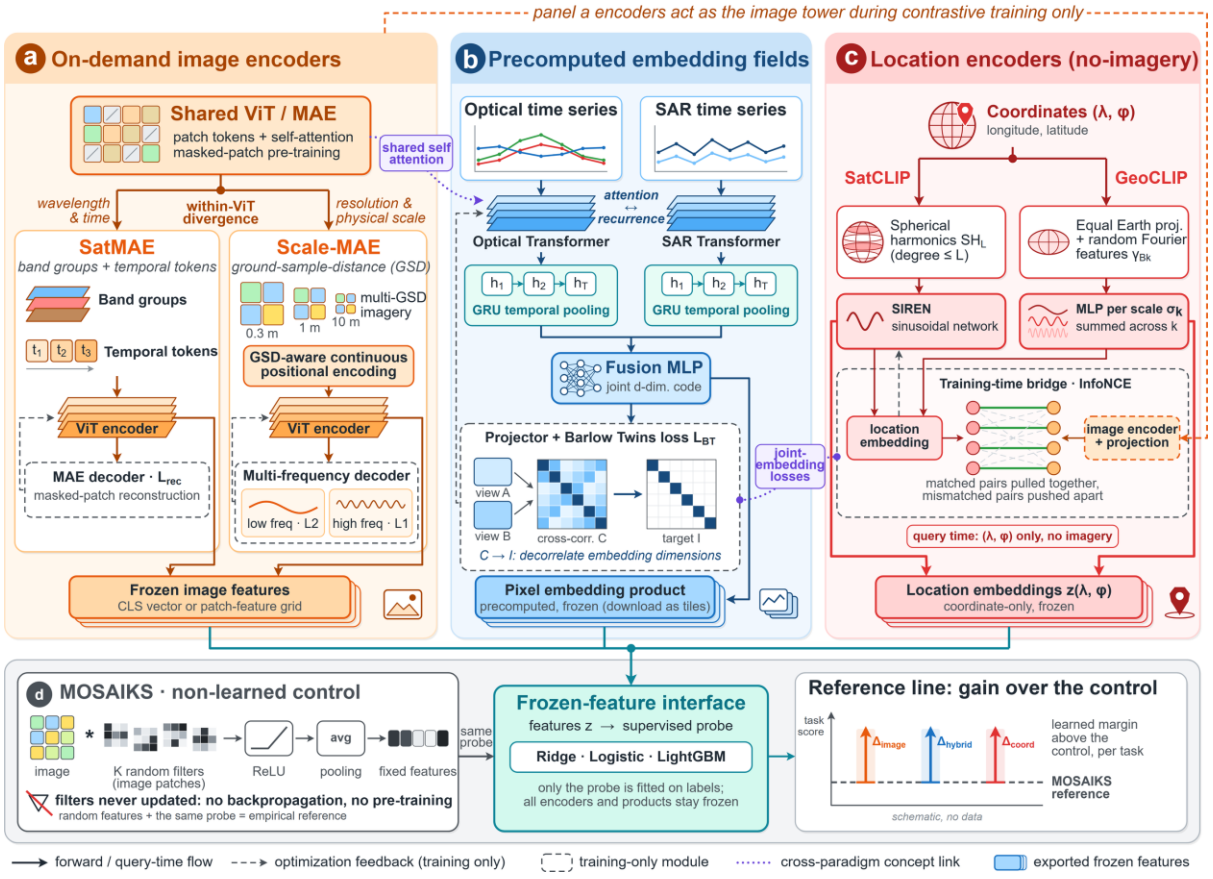


Figure 7. Architectural foundations and connected model families. (a) SatMAE and Scale-MAE share a ViT/MAE foundation but alter different parts of the representation pipeline: SatMAE has temporal and spectral-group configurations, whereas Scale-MAE incorporates physical ground scale through GSD-aware positional encoding and low-/high-frequency reconstruction with L2/L1 losses,

respectively. (b) TESSERA v1's reported main-text configuration combines optical and SAR Transformers, GRU temporal pooling, and a fusion MLP; a separate projector supports Barlow Twins training on augmented temporal views. The report also describes attention pooling in Appendix A.2, so the illustrated GRU configuration must be reconciled against each checkpoint. (c) SatCLIP uses spherical harmonics and a SIREN network, while GeoCLIP uses an Equal Earth projection, multiscale random Fourier features, and MLPs. Their contrastive image–location training bridges are applied separately, and the image branches are unnecessary for coordinate-only feature queries. (d) MOSAIKS provides an empirical reference control using fixed random convolutional features without feature-extractor backpropagation. The common downstream interface expresses feature reuse, not architectural identity or equivalent performance; the reference-line panel is schematic and contains no data. Dotted connections denote conceptual affinity or control comparison; solid and dashed arrows denote forward flow and optimization feedback, respectively. Diagram construction used AI-assisted coding with OpenAI Codex and Anthropic Claude Code (October 2026 workflow); the editable artwork and provenance are retained.

SatMAE illustrates variation within a common backbone family. Its temporal formulation associates spatial patch tokens with acquisition-time encodings, whereas its multispectral formulation uses separate patch projections for spectral groups and encodes group identity. These are distinct configurations; an RGB checkpoint does not automatically inherit the temporal and multispectral capabilities of the complete model family (Cong et al., 2022).

Scale-MAE also uses a ViT-based masked autoencoder, but introduces ground-sampling-distance-aware positional encoding and a decoder that reconstructs low-frequency structure and high-frequency residuals. Its reconstruction objectives include L2 and L1 terms, respectively. Consequently, its distinction from SatMAE involves the physical scale represented by positional information and the reconstruction targets, not simply the presence of self-attention (Reed et al., 2023).

TESSERA v1's reported main-text architecture instead processes optical and radar pixel time series through separate Transformer branches, GRU temporal pooling, and a fusion MLP. A separate, larger MLP projector supports Barlow Twins training. It is therefore a pixel time-series encoder rather than a spatial patch ViT (Feng, Atzberger, et al., 2026).

Location encoders provide a clearer departure from Transformer-only descriptions. SatCLIP combines spherical-harmonic positional encoding with a sinusoidal representation network, or SIREN. GeoCLIP uses an Equal Earth projection, multiscale random Fourier features, and MLPs. Their location-query networks must be distinguished from the image encoders used during pretraining (Cepeda et al., 2023; Klemmer et al., 2025). Operational releases follow the same pattern: the Esri Global Location Encoder (Sentinel-2) packages a SatCLIP-based location network, trained on 2024 Sentinel-2 Level-2A imagery, as an ArcGIS deep-learning package that returns embeddings for point features (Esri, 2026).

MOSAIKS supplies a complementary control: its feature extractor applies fixed random convolutional filters and spatial aggregation, while downstream regression coefficients are fitted using labels. It is therefore recorded as a non-learned feature-extraction control, rather than a pretrained neural encoder, even when its features are distributed as a precomputed collection (Rolf et al., 2021).

These distinctions motivate task-specific interpretation. Spatial token interactions can encode relationships among neighboring surfaces; temporal aggregation can encode seasonal trajectories; location encoders represent location-dependent information learned from their training pairs. Pooling and projection determine which of these signals remain accessible to a downstream readout. These mechanisms motivate comparisons, but their individual effects cannot be identified from unmatched cross-model scores.

SatMAE masks patches across time and separately encodes spectral band groups (Cong et al., 2022); SatMAE++ reconstructs multiple scales (Noman et al., 2024). Scale-MAE

conditions positional encoding on ground sampling distance and tests artificially downsampled RGB images (Reed et al., 2023). Its resolution evidence does not establish robustness to new sensors or future years. Frozen kNN, linear probing and fine-tuning differ, with some comparisons favoring competitors.

RemoteCLIP aligns images and text, including box- and mask-derived captions, and distinguishes retrieval, zero-shot and supervised evaluations (Liu et al., 2024). AnySat combines joint embedding prediction and scale-adaptive spatial encoders (Astruc et al., 2025). Its HLS probe trains a new modality projector and readout; familiar-input probes can use smaller heads. All PASTIS imagery enters unlabelled pretraining, making that evaluation transductive in imagery.

Galileo combines global/local contrastive losses, separating frozen kNN and linear probes from classification fine-tuning (Tseng et al., 2025). Breizhcrops holds out administrative regions without establishing their pretraining exclusion. Dynamic World and WorldCereal provide semantic pretraining inputs, and WorldCover informs site selection: these warrant dependence checks, not a conclusion of direct leakage. Aggregate ranks imply neither universal nor future-year superiority. DOFA uses a wavelength-conditioned dynamic hypernetwork (Xiong et al., 2024). FoMo-Net's band-flexible reuse uses supervised fine-tuning; its benchmark's frozen linear probes belong to PolyNet (Bountos et al., 2025). FoMo-Bench includes satellite and aerial/UAV tasks; point-cloud experiments use specialists. TalloS regions are spatially separated, but pretraining overlap and temporal extrapolation remain unresolved. Frequent specialist wins limit advantage claims; the assessed author PDF lacks referenced appendices.

FG-MAE reconstructs HOG and multispectral indices from one seasonal image, rather than a sequence (Wang, Hernandez Hernandez, et al., 2025). EuroSAT-SAR uses approximately time-matched observations, random splits and non-unified orbit directions;

gains remain conditional on these choices. Cross-paper descriptions cannot isolate learning-signal effects without matched architectures, observations, support and readout budgets.

Early fusion concatenates/projects inputs before a shared backbone; intermediate fusion exchanges tokens or cross-attention features; late fusion combines representations at readout. Wavelength tokenizers and missing-modality training are additional choices affecting parameter sharing, missing-source tolerance, per-frame compute and dense-output alignment.

Table 3. Representative technical characteristics across release categories. Rows describe identified architectural configurations rather than mutually exclusive model families. Training-only modules are distinguished from modules required to reproduce the exported representation. Product category refers to the delivered artifact, while architecture refers to its generator. The selection spans the literature beyond the executable inventory; it is not a census or a performance ranking. MOSAIKS is included as a non-learned feature-extraction control.

Model / version	Release object	Input and feature topology	Architecture	Learning signal	Export boundary
SatMAE	Image encoder	Spatial patches; temporal or spectral-group encodings according to variant	ViT encoder with training decoder	Masked reconstruction	Encoder features; reconstruction decoder omitted for feature extraction
Scale-MAE	Image encoder	Spatial patches with GSD-aware positions	ViT with multiscale reconstruction decoder	Low-frequency L2 and high-frequency L1 reconstruction	Encoder features; physical scale metadata remains relevant
TESSERA v1	Precomputed annual embeddings; generator described separately	Per-pixel optical and radar sequences	Transformer branches, reported GRU pooling, fusion MLP (1)	Barlow Twins with additional regularization	Fusion features retained; training projector omitted
SatCLIP	Location encoder	Spherical-harmonic location features	SIREN location network; separate image-training branch	Symmetric image-location contrast	Location network queried without imagery
GeoCLIP	Location encoder	Projected coordinates with multiscale Fourier features	MLP location branches; separate image-training branch	Image-location contrast with augmented locations and queued negatives	Location features; aligned image branch retained when performing image geolocation
MOSAIKS	Precomputed feature collection / control	Convolutional responses aggregated over an image	Fixed random filters	No gradient-trained feature extractor; supervised downstream regression	Fixed feature vector and separately fitted predictor

3.3.2 Learning objectives

Let x_i denote the observations and associated metadata for sample i, f_θ an encoder, $h_i = f_\theta(x_i)$ its intermediate representation, and p_ψ an optional training projector. The exported embedding $z_i = r(h_i)$ is defined by a specified extraction operation r, which may include layer selection, projection, normalization, or pooling. The representation constrained by a pretraining loss need not be identical to the representation distributed to users.

Masked reconstruction. For visible patch indices $\mathcal{V}_i$ and masked indices $\mathcal{M}_i$, a decoder d_ω predicts masked content from the visible-token representation. A canonical masked-autoencoding objective is

$$\mathcal{L}_{\mathrm{MAE}} = \frac{1}{N}\sum_{i=1}^{N}\frac{1}{|\mathcal{M}_i|}\sum_{p\in\mathcal{M}_i}\frac{\left\|[d_\omega(f_\theta(x_{i,\mathcal{V}_i}))]_p - \tilde{x}_{i,p}\right\|_2^2}{D_p}.$$

Here, $\tilde{x}_{i,p}$ is the specified reconstruction target and D_p is its number of scalar components. Target normalization, masking geometry, and whether prediction concerns pixels, spectral indices, or latent features must be documented. The expression describes canonical pixel-MSE reconstruction; it does not replace the frequency-specific objectives of Scale-MAE or the targets of other reconstruction variants. For feature extraction, a training-only reconstruction decoder is ordinarily omitted (He et al., 2022).

Contrastive alignment. Let u_i and v_i be unit-normalized representations of a matched pair, such as two views, an image and a caption, or an image and its location. With temperature $\tau > 0$, an in-batch InfoNCE objective is

$$\mathcal{L}_{\mathrm{InfoNCE}}(U,V) = -\frac{1}{N}\sum_{i=1}^{N}\log\frac{\exp(u_i^\top v_i/\tau)}{\sum_{j=1}^{N}\exp(u_i^\top v_j/\tau)}.$$

The symmetric CLIP form is

$$\mathcal{L}_{\mathrm{CLIP}} = \frac{1}{2}[\mathcal{L}_{\mathrm{InfoNCE}}(U,V) + \mathcal{L}_{\mathrm{InfoNCE}}(V,U)].$$

CLIP-style alignment is thus a particular contrastive formulation rather than a separate, mutually exclusive learning category. Pair construction determines the information encouraged by the objective, while negative sampling determines which observations are treated as alternatives. Image-text pairing supplies different supervision from temporal-view or image-location pairing, even when the mathematical loss has the same form (Radford et al., 2021).

Redundancy reduction. For two augmented views, let $q_i^a = p_\psi(f_\theta(x_i^a))$ and $q_i^b = p_\psi(f_\theta(x_i^b))$. With $\overline{q}$ denoting batch-centered components, define

$$C_{kl} = \frac{\sum_{i=1}^{N} \overline{q}_{ik}^{a}\, \overline{q}_{il}^{b}}{\sqrt{\sum_i (\overline{q}_{ik}^{a})^2}\sqrt{\sum_i (\overline{q}_{il}^{b})^2}}.$$

The Barlow Twins objective is

$$\mathcal{L}_{\mathrm{BT}} = \sum_k (1 - C_{kk})^2 + \lambda_{\mathrm{BT}} \sum_k \sum_{l \neq k} C_{kl}^2.$$

The diagonal term aligns corresponding components across views; the off-diagonal term discourages redundancy between components. Unlike InfoNCE, this formulation does not explicitly classify other samples as negatives (Zbontar et al., 2021).

TESSERA constructs views by independently sampling valid observations from a pixel's annual series and supplements this objective with mix-based regularization. Its exported feature precedes the training projector; the fusion MLP remains part of the encoder (Feng, Atzberger, et al., 2026).

These objectives describe different constraints on representation learning, not guaranteed downstream capabilities. Reconstruction can retain information unnecessary for a particular target, whereas alignment can suppress differences treated as invariant during pretraining. Interpretation therefore requires the loss, its targets and augmentations, and the exported feature to be considered together.

3.3.3 Location representations

Continuous location encoding replaces a fixed set of geographic classes with a function evaluated at geographic coordinates. For longitude λ and latitude φ, a location on the unit sphere is

$$s(\lambda, \varphi) = (\cos\varphi\cos\lambda, \cos\varphi\sin\lambda, \sin\varphi) \in \mathbb{S}^2.$$

A schematic SatCLIP location encoder is

$$g_\phi(s) = SIREN_\phi(SH_L(s)),$$

where SH_L denotes spherical-harmonic features at a specified truncation level. For paired imagery x_i and locations s_i, normalized image and location features enter the symmetric contrastive objective:

$$\mathcal{L}_{\text{coord}}^{\text{SatCLIP}} = \mathcal{L}_{\text{CLIP}}\left(\{norm(f_\theta(x_i))\}_{i=1}^N, \{norm(g_\phi(s_i))\}_{i=1}^N\right).$$

The spherical domain and harmonic basis provide architectural structure; they do not imply that training minimizes geographic distance or enforces a universal spatial-smoothness penalty (Klemmer et al., 2025).

Location encoding has a broader lineage than these two models. Space2Vec uses multi-scale sinusoidal grid-cell representations (Mai et al., 2020), Sphere2Vec extends multi-scale encoding to the spherical surface (Mai, Xuan, et al., 2023), and CSP pretrains location encoders contrastively with geotagged images (Mai, Lao, et al., 2023). Spatial implicit neural representations estimate species ranges directly from coordinates (Cole et al., 2023). More recent designs concentrate capacity regionally with spherical Slepian functions (Rao, Crasto, et al., 2026) or learnable spherical Voronoi partitions (Cher et al., 2026), recover visual detail through retrieval augmentation (Dhakal et al., 2025), enforce continuity for out-of-sample queries (Hao et al., 2025), or centre the representation on climate rasters, OpenStreetMap graphs or human-mobility graphs rather than satellite imagery alone (Dollinger et al., 2025; Michail et al., 2026; Wen et al., 2026). Because these encoders differ in supervision and

effective resolution, the content of a location embedding must be established empirically rather than inferred from its coordinate input.

For GeoCLIP, let a be the projected and normalized coordinate. Its multiscale encoding can be summarized as

$$\gamma_{B_k}(a) = \begin{bmatrix}\cos(2\pi B_k a)\\ \sin(2\pi B_k a)\end{bmatrix}, g_\phi(a) = \sum_{k=1}^{K} MLP_{\phi_k}(\gamma_{B_k}(a)),$$

where the fixed random matrices B_k represent different frequency scales. GeoCLIP uses image-to-location contrastive training with coordinate augmentation and additional queued negatives, rather than precisely the symmetric in-batch objective above. Its original training images are geotagged photographs, a distinction from SatCLIP's satellite supervision that must remain explicit when interpreting Earth-observation applications (Cepeda et al., 2023).

A further distinction concerns the geometry of latent embeddings. A unit-normalized d-dimensional representation lies on $\mathbb{S}^{d-1}$, which is not the geographic sphere $\mathbb{S}^2$. For example, AlphaEarth uses a von Mises-Fisher bottleneck,

$$q(z \mid x) = C_d(\kappa)\exp(\kappa\mu_\theta(x)^\top z), z, \mu_\theta(x) \in \mathbb{S}^{d-1},$$

where $C_d(\kappa)$ is the normalizing constant and κ controls concentration. This distribution describes a latent bottleneck, not a standalone coordinate-learning loss. AlphaEarth combines source reconstruction, embedding-uniformity, teacher-student consistency, and text-alignment terms. Geographic input geometry, latent geometry, and optimization objective should therefore be recorded separately (Brown et al., 2025).

3.4 Feature extraction

Compact pooled vectors support classification, regression and retrieval but can erase boundaries and rare-class mixtures. Dense grids and feature pyramids retain local structure when stride and alignment are known. Location-query spaces are not image embeddings without an explicit Earth-observation link. Products add indexing, quantization, compression and versioning: equal dimensions in annual integer layers and floating-point scene vectors

need not imply equal precision or update semantics (Corley et al., 2026; Fang et al., 2026; Gomes et al., 2025; Hackel et al., 2026).

Upstream model construction and product generation are distinct from user-side inference. The three pathways converge on reusable features, but allocate computation and constrain user choices differently. Figure 8 traces the three pathways from upstream construction across the public release boundary to a shared frozen-feature readout.

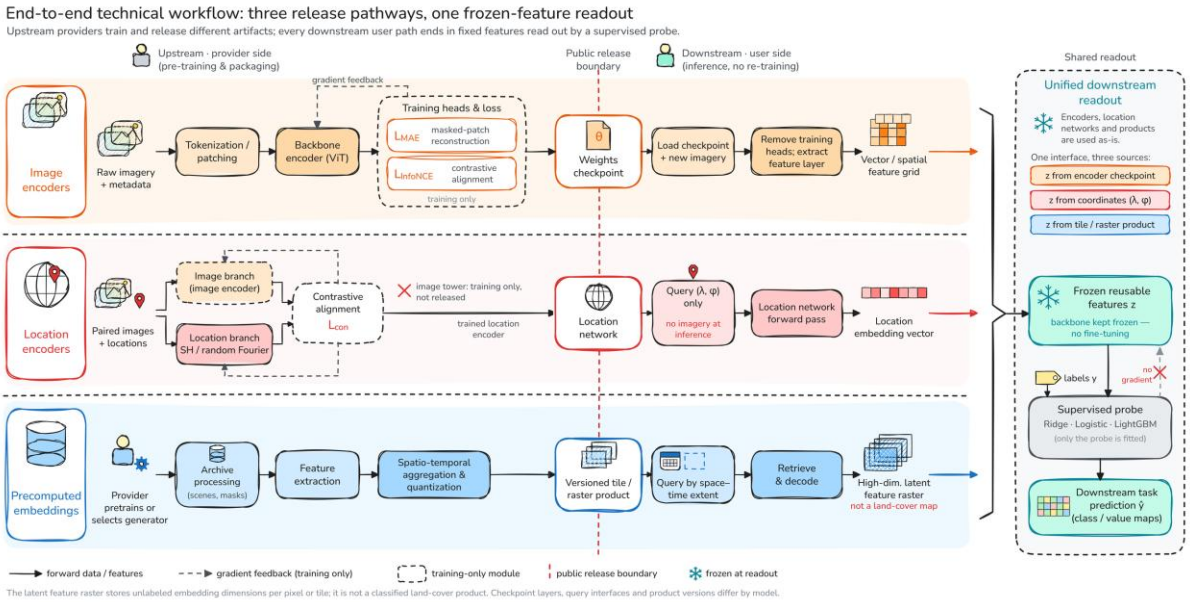


Figure 8. From upstream construction to frozen downstream readout for the three release classes. Image encoders (top lane) are trained on imagery and metadata; users load the released checkpoint and select the documented feature-extraction layer for new observations. Training-only heads are omitted, whereas projections required to define the exported space are retained. Location encoders (middle lane) learn from paired images and locations through model-specific contrastive training; the released location network produces an embedding from coordinates without query-time imagery. For precomputed embedding products (bottom lane), providers apply a generator to an observation archive and package features as versioned tile or raster products, with aggregation and quantization where applicable; users retrieve and decode latent channels rather than land-cover classifications. All pathways supply fixed features to a supervised readout trained with labels; the backbone or feature generator is not fine-tuned. The red dashed line marks the public release boundary. Solid arrows denote forward data or feature flow, dashed arrows optimization feedback, and dashed outlines

modules used only during upstream training. Diagram construction used AI-assisted coding with OpenAI Codex and Anthropic Claude Code (October 2026 workflow); the editable artwork and provenance are retained.

Image encoders. Upstream training combines prepared observations, tokenization, an encoder, and the heads required by its learning objectives. User-side extraction begins by loading the selected checkpoint and reproducing its band ordering, radiometric scaling, normalization, metadata encoding, and spatial or temporal sampling. The user then selects the documented extraction layer and readout. A pooled representation has the form $z \in \mathbb{R}^d$; a spatial feature grid has the form $Z \in \mathbb{R}^{H' \times W' \times d}$. Temporal or multiscale outputs require additional indexing. These forms are not interchangeable: averaging spatial tokens changes support and removes their explicit arrangement.

Location encoders. Pretraining uses paired locations and observations, with the trainability of each branch specified by the model. At deployment, the location pathway evaluates the coordinate transform and location network to produce $z = g_\phi(s)$. No imagery is required at the queried location. This avoids new image acquisition and preprocessing, but the resulting feature expresses information learned during pretraining rather than a fresh observation of current surface conditions. A coordinate-only model without a temporal input cannot resolve changes at the same location merely by repeating the query.

Precomputed embedding products. The provider trains or selects a generator, applies it to an observation archive, and packages the extracted features into a versioned collection or geospatial layer. Spatial or temporal aggregation, quantization, and indexing occur where specified by that product's construction process. Users retrieve features by location and, where supported, time; decode stored values; apply validity masks; and align feature support with the target. They do not ordinarily load or rerun the generator. A dense embedding raster contains latent feature channels, not land-cover classes or calibrated class probabilities.

Exported heads and downstream training. Removing training heads is conditional on their role. Reconstruction decoders and redundancy-reduction projectors may be omitted during feature extraction, whereas a projection defining a shared contrastive space must be retained when that space is the intended output. Removing every module named "projection" would therefore change some representations rather than merely simplify inference. The extraction record must identify the retained modules, output layer, normalization, and feature dimension.

For a frozen linear probe, feature extraction is fixed and only predictor parameters are fitted:

$$(W^*, b^*) = \underset{W,b}{argmin}\left[\frac{1}{n_{\mathrm{tr}}}\sum_{i\in\mathcal{D}_{\mathrm{tr}}} \ell\left(Wz_i + b, y_i\right) + \lambda_{\mathrm{probe}}\|W\|_F^2\right].$$

Here, ℓ is chosen for the downstream task and no encoder parameter is updated. Standardization, dimensionality reduction, and predictor selection are fitted using the designated training and validation partitions. Training an adapter, updating the backbone, or fitting a spatial decoder constitutes a different adaptation regime and must be identified accordingly. Product retrieval eliminates user-side embedding generation, but does not eliminate the need to fit or validate a downstream mapping model.

Adaptation spans zero-shot retrieval, frozen probes, trainable adapters and full fine-tuning. DEFLECT freezes its backbone but trains adapters and heads; reported tuning percentages exclude the segmentation head (Thoreau et al., 2025). Some adapters trail full fine-tuning. The Billion-scale study fully fine-tunes detection/segmentation systems after unequal pretraining durations (Cha et al., 2026), isolating neither parameter count nor frozen-embedding rank. Low-label results are not uniformly monotonic with size; an unresolved LoveDA background-class discrepancy limits cross-paper effect comparisons. Our cells fix readout budgets and record every trained component.

SITS-BERT jointly fine-tunes its transformer and classifier. Its cross-region tests support temporal pretraining with supervised adaptation; random within-area train/validation pixels leave spatially blocked generalization unresolved (Yuan & Lin, 2021). SatDiFuser freezes a diffusion backbone but trains fusion components with a linear classifier or UPerNet decoder (Jia et al., 2025); unspecified normalization boundaries leave train-only fitting uncertain. Its RemoteCLIP-labelled comparison cites a different ground–remote alignment paper, leaving the pairwise model identity unresolved.

RemoteCLIP tests zero-shot prompting, retrieval, linear classification and nearest-neighbour readout (Liu et al., 2024). Annotation-derived captions provide semantic supervision; image-hash deduplication establishes neither geographic nor temporal independence. Some datasets show zero-shot declines relative to CLIP. None of these studies supplies the matched observations, adaptation, readout and geographic validation needed to rank our catalogue.

GEO-Bench-2's main results use end-to-end fine-tuning; freezing encoders while training heads or UNet decoders reorders over 20% of model pairs (Simumba et al., 2026). Adding SAR lowers PASTIS scores for DOFA, Clay and TerraMind, improves BioMassters and yields mixed BigEarthNet V2 outcomes. Ranks therefore depend on observations and trained components. Bootstrap summaries resample seed repeats within datasets, establishing neither geographic confidence intervals nor calibrated predictive uncertainty. Supplementary Methods S2 identifies assessed versions.

3.5 Benchmark inventory

Table 4 links the executable inventory to the release taxonomy. Its configuration-specific input, support and output descriptors identify what was evaluated; they do not define the literature inclusion frame. The archived evidence matrix records source versions and distinguishes documented attributes from unknowns.

Table 4. Executable inventory and configuration-specific descriptors. The 20 entries comprise 16 image encoders, one location encoder and three precomputed products, with frozen release labels A1-A4, B and C1. Repository support is separate from review eligibility. Input, support, output and deployment descriptors identify the assessed configurations and do not imply matched performance across rows. Historical Wuhan adapters and the controlled global input protocol are distinguished where their configurations differ.

Model	Year / venue	Class / object	Architecture and learning signal	Training and inference observations	Spatial and temporal support	Configured output
TESSERA v1.1 (global product)	2026 / arXiv v7	C1 · precomputed annual product	Dual temporal encoders with Transformer/GRU pooling; Barlow Twins self-supervision	Sentinel-1/2 annual pixel series upstream; current adapter reads precomputed embeddings	10 m precomputed embedding tiles; annual lookup over product years	128; pooled or grid
GSE (AlphaEarth Foundations v2.1 annual)	2025 / arXiv	C1 · precomputed annual product	Space Time Precision encoder; multi-source prediction, teacher–student learning and text alignment	Sentinel-2, Landsat 8/9 and Sentinel-1 observations upstream; current adapter reads annual embeddings	10 m annual product; strict yearly query	64; pooled or grid
Copernicus-Embed-025deg	2025 / ICCV	C1 · precomputed 0.25° field	Precomputed features exported by Copernicus-FM; the encoder checkpoint and distributed feature product are distinct releases	Copernicus product stack	0.25 degree precomputed grid; static in current adapter (2021 only)	768; pooled or grid
RemoteCLIP	2024 / IEEE TGRS	A1 · image encoder	CLIP / ViT-B-32; vision–language satellite embedding; contrastive image–text alignment (InfoNCE)	Sentinel-2 RGB at inference; captions and UAV imagery in pretraining	Shared 640 m footprint; RGB from one 2021 Sentinel-2 L2A acquisition; full-extent resizing; source band GSD 10 m	512 pooled (global); historical grid export differs
SatMAE	2022 / NeurIPS	A1 · image encoder	ViT-MAE; masked autoencoding with temporal and spectral positional encoding	Sentinel-2 RGB at inference; temporal and multispectral configurations are distinct releases in the original work	Shared 640 m footprint; RGB from one 2021 Sentinel-2 L2A acquisition; full-extent resizing; source band GSD 10 m	1024; pooled or grid

Model	Year / venue	Class / object	Architecture and learning signal	Training and inference observations	Spatial and temporal support	Configured output
SatMAE++ RGB	2024 / CVPR	A1 · image encoder	ViT-L / SatMAE++; revised masked autoencoding for multispectral imagery	Sentinel-2 RGB at inference; multispectral Sentinel-2 in the paper	Shared 640 m footprint; RGB from one 2021 Sentinel-2 L2A acquisition; full-extent resizing; source band GSD 10 m	1024; pooled or grid
SatMAE++ S2	2024 / CVPR	A2 · image encoder	ViT-L / grouped-channel SatMAE++; grouped-channel multispectral masking	Sentinel-2 SR 10-band at inference	Shared 640 m footprint from one 2021 Sentinel-2 L2A acquisition on a 10 m lattice; native band subset and preprocessing retained	1024; pooled or grid
Scale-MAE	2023 / ICCV	A1 · image encoder	ViT-L / MAE; scale-aware masked autoencoding with resolution conditioning	Sentinel-2 RGB at inference; multiscale EO imagery in the paper	Shared 640 m footprint; RGB from one 2021 Sentinel-2 L2A acquisition; full-extent resizing; source band GSD 10 m	1024; pooled or grid
AnySat	2025 / CVPR	A4 · image encoder	Versatile JEPA-style encoder; generalist multi-resolution multimodal self-supervised representation learning	Sentinel-2, Sentinel-1, aerial/ VHR, and other modalities in the original work; Sentinel-2 sequence in current adapter	Shared 640 m footprint; twelve 2021 calendar-month clear-pixel composites with ten common bands and month identifiers	768 pooled (global); 1,536 pooled in historical Wuhan
Galileo	2025 / ICML	A4 · image encoder	Transformer with global/ local branches; multimodal time-series self-supervision	Sentinel-2 time series and multiple remote-sensing modalities in the original work	Shared 640 m footprint; twelve 2021 calendar-month clear-pixel composites with ten common bands and month identifiers	128; pooled or grid
WildSAT	2025 / ICCV	A1 · image encoder	ViT-B/16 with native 256-dimensional image head; wildlife-aligned representation learning	Sentinel-2 RGB at inference; wildlife observations as supervision	Shared 640 m footprint; RGB from one 2021 Sentinel-2 L2A acquisition; full-extent resizing; source band GSD 10 m	256 pooled with native image head (global); historical grid export differs

Model	Year / venue	Class / object	Architecture and learning signal	Training and inference observations	Spatial and temporal support	Configured output
Prithvi-EO-2.0-100M-TL	2026 / IEEE TGRS (EO-2.0 report)	A2 · image encoder	ViT / masked-autoencoder lineage; self-supervised geospatial pretraining	Sentinel-2 six-band input; checkpoint-required location and time encodings retained; HLS pretraining	Shared 640 m footprint from one 2021 Sentinel-2 L2A acquisition on a 10 m lattice; native band subset and preprocessing retained	768; pooled or grid
TerraFM	2026 / ICLR	A2 · image encoder	Multisensor transformer; unified multisensor pretraining	Sentinel-2 and Sentinel-1; current adapter selects one sensor path	Shared 640 m footprint from one 2021 Sentinel-2 L2A acquisition on a 10 m lattice; native band subset and preprocessing retained	768; pooled or grid
TerraMind	2025 / ICCV	A2 · image encoder	Generative multimodal transformer; large-scale generative multimodal learning	Sentinel-2 SR 12-band at inference; wider multimodal EO stack in the paper	Shared 640 m footprint from one 2021 Sentinel-2 L2A acquisition on a 10 m lattice; native band subset and preprocessing retained	384; pooled or grid
DOFA	2024 / arXiv	A3 · image encoder	Wavelength-aware transformer with dynamic wavelength handling; self-supervised multimodal EO modelling	Multispectral and hyperspectral-style inputs; Sentinel-2 path in current adapter	Shared 640 m footprint from one 2021 Sentinel-2 L2A acquisition on a 10 m lattice; native band subset and preprocessing retained	768; pooled or grid
FoMo	2025 / AAAI	A3 · image encoder	Band-flexible transformer; masked spectral/spatial reconstruction	Sentinel-2 SR 12-band at inference; multiple scales and tasks in original work	Shared 640 m footprint from one 2021 Sentinel-2 L2A acquisition on a 10 m lattice; native band subset and preprocessing retained	768; pooled or grid
THOR	2026 / arXiv	A3 · image encoder	Versatile transformer for climate and society; foundation pretraining	Sentinel-2 SR 10-band	Shared 640 m footprint from one 2021 Sentinel-2 L2A acquisition on a 10 m lattice; native band subset and preprocessing retained	768; pooled or grid

Model	Year / venue	Class / object	Architecture and learning signal	Training and inference observations	Spatial and temporal support	Configured output
AgriFM	2026 / RSE	A4 · image encoder	Video Swin Transformer; supervised land-cover-fraction pretraining with EMA teacher	Sentinel-2 at inference; Sentinel-2, Landsat-8/9, and MODIS in original work	Shared 640 m footprint; twelve 2021 calendar-month clear-pixel composites with ten common bands and month identifiers	1024; pooled or grid
SatVision-TOA	2024 / arXiv	A2 · image encoder	SwinV2-style coarse-resolution foundation model; all-sky MODIS pretraining	MODIS 14-band TOA	1000 m; single coarse-resolution window	4096; pooled or grid
SatCLIP (ViT16-L40 location branch)	2025 / AAAI	B · location encoder	Spherical-harmonic encoding (L = 40) with SIREN network; image–location contrastive pretraining with a ViT-16 image tower used only in training	Longitude/latitude only at inference; Sentinel-2 multispectral tiles (S2-100K) in pretraining	Global; spatial detail limited by harmonic degree; no temporal input	256; pooled (centre query) or coordinate grid

Table 5. Examples of axis-level contrasts and the evidence needed before a mechanistic interpretation. The rows are comparison questions, not rankings.

Comparison question	Observable design difference	Required interpretation check
Product versus checkpoint	Queryable annual/tiled layer versus user-run encoder with selectable inputs	Report version, update cadence, latency, storage, missingness, and temporal flexibility alongside predictive scores.
Optical versus optical–SAR	One sensor stream versus fused or routed streams with different availability and noise	Match the observed inputs and test a missing-modality condition before attributing a gain to fusion.
Single date versus sequence	One acquisition/composite versus date-aware multi-frame representation	Align target time and compare event-sensitive and persistent targets separately.
Pooled versus dense readout	One vector versus token grid or multiscale map	Match output stride and target geometry; do not infer local boundary quality from a pooled score.
Native versus reduced dimension	Full vector versus train-only PCA or truncation	Report dimension curves and fit transforms on training data only.

Product performance combines upstream observations, labels, aggregation and quantization with encoding; downstream scores additionally depend on decoders, labels and splits. Section 5 controls source inputs and evaluation within declared cells (Lacoste et al., 2023; X. Li et al., 2025; Simumba et al., 2026). These compare particular frozen checkpoints without isolating causal effects of architecture, pretraining data, objectives or pooling.

4. Task Requirements and Evaluation Design

An embedding is useful when its retained information, observation support and access conditions fit a defined prediction problem. The literature on reusable models and products makes these requirements explicit (Brown et al., 2025; Fang et al., 2026; Feng, Atzberger, et al., 2026; Klemmer et al., 2026; Lu et al., 2025; R. Ramachandran et al., 2025; Xiao et al., 2025). This section uses that evidence to explain the comparisons in Section 5; it does not claim new experiments for every application domain.

Figure 9 connects application requirements with release contracts and summarizes the baseline-relative results examined in Sections 5 and 6. The following synthesis distinguishes

what a task requires, what a published score establishes and what our experimental design can test. A shared storage format alone does not align feature spaces or observation support.

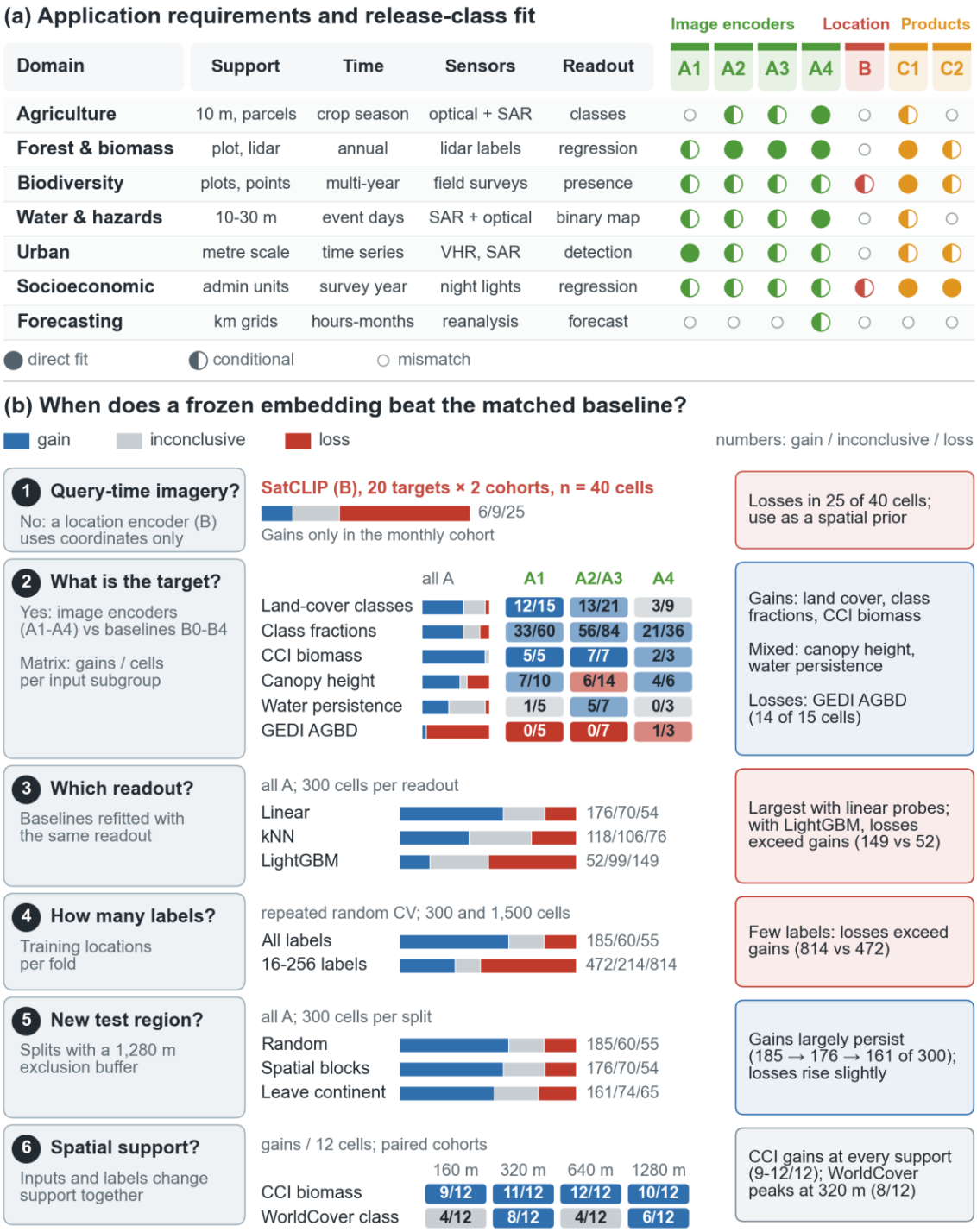


Figure 9. Application requirements and the conditions under which frozen embeddings outperformed matched baselines. (a) Synthesis of Section 4: required spatial support, temporal contract, sensors and labels, and readout for each application domain, and whether the delivered contract of each release class (A1–A4 image encoders, B location encoders, C1 gridded embedding fields, C2 sampled

embedding collections) meets the requirement directly, only after dates, support or sensors are checked, or not at all. The symbols summarize illustrative requirements, not class-wide capabilities or measured performance; each specific release still requires checks of sensors, dates, support and label availability. (b) Decision sequence over the Part I (2021) cells. Bars count embedding-system × target cells whose 95% paired-bootstrap interval of Δ (embedding minus the strongest of the six baseline variants B0, B1, B2, B3-1024, B3-4096 and B4, reselected in each of 999 draws) lies wholly above zero (gain), includes zero (inconclusive) or lies wholly below zero (loss). Unless stated otherwise, cells use 640 m support, native features, linear readouts, all training labels and spatial CV in the annual (G2a, G3) and monthly (G2b) cohorts. Step 4 uses repeated random CV with nested budgets of 16–256 training locations per fold; step 6 uses the paired footprint cohorts, in which inputs and labels change support together. For kNN and LightGBM, the baselines are refitted with the same readout. Intervals are per cell and not simultaneous, and the references are map products or sparse GEDI-derived targets rather than independent field inventories. GSE, TESSERA, SatVision-TOA and Copernicus-Embed were not eligible for controlled prediction. The counts describe this design, not universal rules. The separate GSE/TESSERA predictive extension appears in Figures 13–16 and is not included in these controlled-design counts.

4.1 Access and observation support

The access path determines which observations a user can control. Image encoders require weights, sensor-specific preprocessing and inference; location encoders accept coordinates; finite embedding datasets provide fixed samples; and gridded products add spatial indexing, versions and update policies. Services mediate access rather than defining another learning objective (Czerkawski et al., 2024; Fang et al., 2026; Francis & Czerkawski, 2024; Ye et al., 2026).

Release metadata must distinguish output spacing from observation support. AlphaEarth and Tessera provide annual products on 10 m grids (Brown et al., 2025; Feng, Atzberger, et al., 2026), whereas Major TOM distributes patch embeddings with timestamps, footprints and

source identifiers (Czerkawski et al., 2024). Annual aggregation does not recover event timing, and a fine grid does not establish fine effective support. Quantization, validity masks and decoding rules also remain release-specific.

Tessera v2 describes variable-length inference and learned nested feature prefixes (Feng, Jaffer, et al., 2026). These capabilities cannot be assigned to v1 or inferred from arbitrary truncation, and the assessed global annual release remains planned. Documented capability and an available product are separate requirements.

Table 6. Deployment information that accompanies a representation. Predictive quality must be assessed alongside these operational records.

Field	Required record
Identity and version	Study, model/checkpoint or product release, source URL, retrieval date, checksum, and relation to prior versions.
Input contract	Required sensors/bands, dates or sequence length, cloud and nodata handling, projection, footprint, and resampling.
Output contract	Pooled or dense geometry, stride/support, dimension, layer, normalization, quantization, compression, and ordering.
Access and governance	Code, weights, vectors, and data licences separately; authentication, quota, cost, geographic restrictions, update and deprecation policy, and offline-cache status.
Operational cost	Latency, GPU/CPU memory, network requests, bytes transferred, local storage, failure rate, and reproducible environment.

Table 6 records the information required to reproduce feature access and reuse. A locally available adapter may expose less information than the released model supports. Inaccessible artifacts remain unresolved rather than receiving zero scores or being excluded from the literature.

Search introduces another access contract. Copernicus embedding datasets support semantic and similarity queries (Augustyn et al., 2026), while language proxies can retrieve locations from frozen Clay features (Walsh et al., 2026). Such neighbourhood-based results require a retrieval evaluation and do not establish the calibrated mapping performance tested here.

Reuse can mean a fixed feature table, as in MOSAIKS (Rolf et al., 2021); adaptation across tasks, as in METEOR (Rußwurm et al., 2024); or semantically structured multimodal pretraining, as in SkySense++ (Wu et al., 2025). These mechanisms share the broader motivation discussed by Zhu et al. (2026), but require different controls when compared.

Deployment comparisons must account jointly for predictive quality, uncertainty, latency, memory, transfer, licences and version stability (Fang et al., 2026; Gomes et al., 2025; Ye et al., 2026). Pretraining, feature production, retrieval and downstream fitting have different cost boundaries (Brown et al., 2025; Czerkawski et al., 2024; Feng, Atzberger, et al., 2026; Feng, Jaffer, et al., 2026). Our encoder measurements address only their recorded inference stage, not lifecycle efficiency.

4.2 Task definitions and validation evidence

The prediction unit determines the readout. Classification tests separation between classes, regression tests continuous information, and dense mapping requires spatially located features and aligned labels. Image-text retrieval, exemplified by RemoteCLIP (Liu et al., 2024), asks a different question from supervised mapping. Performance cannot be transferred between these tasks without testing the relevant output and support (Lacoste et al., 2023; X. Li et al., 2025; Simumba et al., 2026).

For continuous targets, the perspective of Xue and Zhu (2026) motivates testing vision-language representations, but proposed mechanisms and uncertainty methods still require primary empirical validation.

Persistent land cover may be represented by annual summaries; flood timing and crop development require observations that resolve the event or season. Likewise, footprint fractions, point measurements and dense labels have different spatial meanings. Resampling cannot restore information removed by pooling or temporal aggregation. These distinctions determine the target units and support controls in Section 5.

Even within vegetation mapping, forest change (Hansen et al., 2013), individual-tree occurrence (Brandt et al., 2020) and carbon stocks (C. Tucker et al., 2023) define different targets. Features that retain texture or cover need not retain structural or biophysical information. Our separate land-cover, height and biomass targets test this distinction without treating one outcome as a proxy for all vegetation tasks.

Ecological validation must preserve both measurement support and target definition. Canopy height (Lang et al., 2023), mangrove structure (Simard et al., 2019), degradation (Bourgoin et al., 2024) and waveform complexity (de Conto et al., 2024) have distinct observation and supervision footprints. BioSCape (Cardoso et al., 2025), Reef Cover (Kennedy et al., 2021) and oil-palm monitoring (Payne, 2021) likewise show why field evidence, class definitions and image access must accompany a mapped label. A training product cannot also be assumed to provide independent validation.

Temporal support separates state mapping from event detection. Dynamic World (Brown et al., 2022) and the long-term surface-water record (Pekel et al., 2016) describe different observation windows from flood-exposure mapping (Tellman et al., 2021) and radar flood archives (Misra et al., 2025). Red-snow (Engstrom & Quarmby, 2023) and rainfall-erosivity studies (Dai et al., 2023) further depend on event-sensitive information. The annual water-persistence target used here therefore cannot validate flood timing or operational early warning.

Agricultural evidence links evaluation to phenology. Studies of management and yield (Ma et al., 2026), Senegalese crops (Lisaius et al., 2026), cropland (Zvonkov et al., 2026), tomato fields (Narimani et al., 2026) and rice events (Brinkhoff & McGavin, 2026) use different labels and observation windows. Feature distillation (Jing et al., 2026), Presto fine-tuning (Butsko et al., 2025) and cross-continent crop transfer (Chang et al., 2025) also change

the adaptation contract. Within-season information remains central (Weiss et al., 2020); our annual targets and monthly inputs do not constitute crop-event or yield validation.

A useful evaluation reports label provenance, observation years, geographic partitions, baselines, adaptation, uncertainty and computation. Capability-based assessment (Simumba et al., 2026) must therefore be accompanied by source-dependence checks. Matching raw observations, splits and tuning budgets helps distinguish representation gain from additional input information.

Existing benchmarks cover complementary parts of this record: sensor and temporal diversity in PANGAEA (Marsocci et al., 2026), environmental targets and geographic splits in MMEarth-Bench (Gordon et al., 2026), and standardized downstream or embedding protocols in PhilEO Bench and NeuCo-Bench (Fibaek et al., 2024; Vinge et al., 2026). Calibration (Wei, 2026), spatial uncertainty (Johnson, 2026) and geographically concentrated failures (Gonzalez-Calabuig et al., 2026) require additional diagnostics beyond aggregate accuracy.

Absolute accuracy and relative robustness need separate interpretation. In REOBench, ScaleMAE retained higher segmentation accuracy under corruption than GeoRSCLIP (Zhang et al., 2024), despite suffering a larger proportional loss (X. Li et al., 2025). Training exposure and adaptation also differed across assessed systems. A robustness score is therefore meaningful only alongside clean performance and the evaluation contract.

Published cases show how support and controls qualify a result. Joseph et al. (2026) related pooled Clay features to Brazilian forest-inventory occurrences using spatial folds. The absence of matched raw-observation controls, differences between imagery and inventory dates, and gaps in biome coverage limit what the comparison establishes about representation gain and transfer.

Li and Yu (2026) map China's crop patterns for 2018–2021 at 10 m using annual AlphaEarth vectors and crop-specific random forests (Breiman, 2001). More than 20 existing crop maps supply consensus labels; cropland masks and cropping-intensity products further constrain the output. The reported 92.60% overall accuracy and F1 of 0.7584 describe a 70/30 split of consensus-map samples, while an administrative-area R^2 of 0.849 assesses aggregated crop-area agreement. These different support-level checks do not establish independent field validity, matched raw-band/time-series advantage, regional exclusion or future prediction. Correlated source errors and minority-crop coverage constrain this scalable mapping product.

Cropp (2026) evaluated reef-cover prediction from annual AlphaEarth features using in-water observations, spatial buffers and site-year exclusions. Stronger exclusions reduced reported agreement, optical controls remained competitive for some targets, and effective support exceeded nominal grid spacing. Together with the crop-mapping case, this demonstrates why independent labels, matched observations and temporal holdouts must accompany an application score. These studies inform validation requirements; their scores cannot be pooled into a model ranking.

Target validity is especially important when observable surface patterns proxy social quantities. Consumption (Jean et al., 2016), economic well-being (Yeh et al., 2020), development rankings (Ahn et al., 2023), settlement-light indicators (McCallum et al., 2022), human-development estimates (Sherman et al., 2026) and mobility (Y. Xu et al., 2025) use different labels and aggregation units. As Burke et al. (2021) emphasize, satellite inference complements ground measurement. Survey support, label construction and subgroup errors therefore remain part of validation.

Embedding-based GDP (Yue et al., 2026), survey-wealth (Pettersson & Daoud, 2026) and urban economic predictions (Hou et al., 2026) further depend on fusion inputs and

geographic partitions. Built-environment and mobility representations can also encode vector or graph information (Choudhury et al., 2026; Wen et al., 2026). Their reported gains do not establish that a satellite-only representation transfers between these targets. These tasks are outside our experimental scope.

Object detection and process measurement also require different evidence. Inventories of solar facilities (Kruitwagen et al., 2021), oil and gas infrastructure (N. Ramachandran et al., 2024) and offshore activity (Paolo et al., 2024) locate objects or activity, whereas methane-release assessment (Lauvaux et al., 2022) requires atmospheric information and attribution. Spatial completeness, timing and missed objects cannot be replaced by an aggregate land-cover score.

Air-quality studies illustrate the same boundary: embeddings used in Quito (Alvarez et al., 2025) and alongside TROPOMI over Europe (Alvarez et al., 2026) provide surface context, while methane quantification requires dedicated atmospheric benchmarks (Radman et al., 2023). These uses motivate checking complementary inputs and ground calibration; they are not validated by our surface-reference experiments.

Forest studies span plot biomass (Jin et al., 2026), geolocation-corrected inventories (Sohrabi, 2026), incremental gains over environmental covariates (Watt et al., 2026) and species classification (Ball et al., 2026). Forest and tree-crop extent (Paluba et al., 2026), planted mangroves (Sun et al., 2026), plantations (Cava et al., 2026), dead-tree fractions (Chowdhury et al., 2026) and communities (Gao et al., 2025) add different label definitions; operational forestry adds deployment constraints (Mura et al., 2026). This diversity calls for target-specific controls and explicit label provenance, rather than transferring a reported advantage across forest tasks.

The same caution applies to steppe species (Strelnikov et al., 2025), fish diversity (Qi et al., 2026), soil biodiversity (Cerna et al., 2026), carbon exchange (Du et al., 2026), peatland

carbon and water-table depth (Koch et al., 2026), and canopy chemistry (Alam & Milas, 2025). Field sampling, predictor fusion and regional validation differ across these studies. Recovering a target locally does not by itself establish geographic transfer or an advantage over matched observations.

Published embedding studies examine streamflow (Ou & Zheng, 2025), discharge correction (Lin et al., 2026), inundation (Betz et al., 2026), landslide susceptibility (Y. Cheng et al., 2026), landslide change (Leonardi et al., 2025), fire severity (Mahato et al., 2026) and burned area (Silva & Gonçalves, 2026). Rock glaciers (Khajuria et al., 2026), surface temperature (Lee-Burkhart et al., 2026) and evapotranspiration (Jiang et al., 2026) introduce further temporal and physical constraints. Land-cover comparisons with spectral indices (Khan & Ahmad, 2025), alternative classifiers (Mantey et al., 2026), seasonal inputs (Díaz-Ireland et al., 2026) and temporal holdouts (Gbodjo & Ienco, 2026) show which controls are needed. These are distinct tests, not interchangeable evidence for general environmental prediction.

4.3 Experimental scope

These requirements motivate the controlled global comparisons and the separate Wuhan diagnostics. The global experiment matches targets, locations and evaluation budgets within declared input groups; the local study examines readout and partition sensitivity under its historical conditions. Neither design validates all application domains represented in the literature.

Figure 10 translates the preceding requirements into the tasks actually evaluated. Global dominant-class and fraction targets test discrete and continuous information at a shared footprint. Height, biomass and water-persistence references probe different environmental signals. Geographic holdouts, alternative readouts, label budgets and footprint sizes examine how observed gains depend on evaluation choices. The Wuhan case adds native-grid

mapping and local partition diagnostics, with its own inputs and references. Retrieval, forecasting, socioeconomic prediction and operational event monitoring remain outside these experiments.

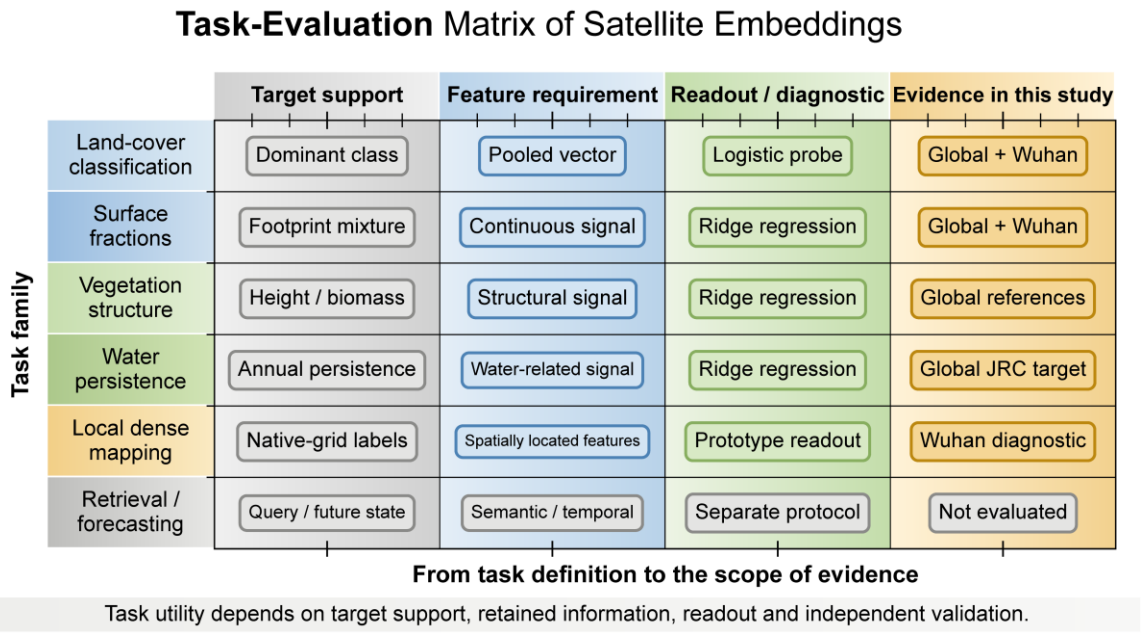


Figure 10. Task requirements and the scope of the empirical evaluation. The matrix links target support to the information required from a representation, the primary readout or diagnostic, and the evidence supplied in Section 5. Global comparisons use pooled representations; the Wuhan study additionally retains a native-grid prototype diagnostic. Annual JRC seasonality represents water persistence rather than event timing. Global and local tasks retain different input and reference contracts. The final row identifies retrieval and forecasting as requirements for separate evaluations, not completed experiments. Colours distinguish matrix dimensions and carry no performance ranking.

5. Experiments

5.1 Data and design

Figure 11 places the completed global comparison within the broader review-to-evaluation framework. The historical Wuhan case adds local spatial diagnostics; it does not independently validate the global results.

The global evaluation used a 9,132-location candidate frame derived from Major TOM Core-S2L2A (Francis & Czerkawski, 2024), with Natural Earth continent attribution (Natural Earth, n.d.) and RESOLVE 2017 biomes (Dinerstein et al., 2017) with sampling stratified by biome and merged land-cover class. A 200 km buffer excluded the Wuhan verification region. Input and target availability filters produced 4,409 annual single-scene locations and 3,014 monthly primary locations (Figure 12; Table 7). These cohorts have different geographic and class compositions; they are not an area-proportional sample of global land. Annual and monthly counts therefore describe separate evaluation populations, and their scores cannot isolate the benefit of temporal input. Target-specific availability masks were identical for every embedding and baseline within each subgroup and target.

The primary footprint was an aligned 640 m square with observations from 2021. G2a, G2b and G3 are input-comparison groups, distinct from the release classes: G2a combines eligible A2 and A3 image encoders, G2b contains A4, and G3 contains A1. SatCLIP remains class B in both cohort-based comparisons. G2a contained SatMAE++ S2, TerraMind (Jakubik et al., 2025), DOFA, FoMo, THOR, TerraFM (Danish et al., 2026) and Prithvi. All received the same Sentinel-2 L2A acquisition (Drusch et al., 2011) and footprint, retaining their native channel subsets and preprocessing; classical image baselines used the complete shared 12-band source. G3 contained RemoteCLIP, SatMAE, SatMAE++ RGB, ScaleMAE and WildSAT (Daroya et al., 2025), using the RGB channels of the same acquisition. G2b contained Galileo, AnySat and AgriFM, using twelve within-month Sentinel-2 clear-pixel composites with the common ten-band selection. Consequently, G2a comparisons evaluate complete systems under shared acquisition conditions, rather than architecture alone under identical channel selection. SatCLIP (ViT16-L40 location branch), the only location encoder, received each location's centre coordinates and no imagery. It was evaluated on the annual cohort against the G2a baselines and on the monthly cohort against the G2b baselines, with

identical folds. These contrasts share target cohorts and readout protocols but compare different query-time information; SatCLIP is not an image-input-matched member of either subgroup. Checkpoint-required location and date encodings were retained, including Prithvi's location and time metadata.

GSE and TESSERA (class C1) are included in a separate product-performance extension on 2,513 common 2021 locations at 640 m, alongside the fifteen scored image encoders and SatCLIP. Identical source observations cannot be established for these annual products, so their reference-baseline differences are not same-input controlled gains. Of the twenty benchmarked systems, only SatVision-TOA and Copernicus-Embed-025deg remain outside this global predictive comparison. SatVision uses native 1 km MODIS observations; the available proxy-channel cache does not establish the required calibrated MOD021KM/MOD03 provenance. Copernicus has 0.25-degree native support (approximately 23 by 28 km in this cohort), and every 640 m footprint fails the native-pixel support rule. Both retain historical Wuhan diagnostic records, but these do not supply comparable 640 m global scores. Eligibility is an evaluation status, not a release class.

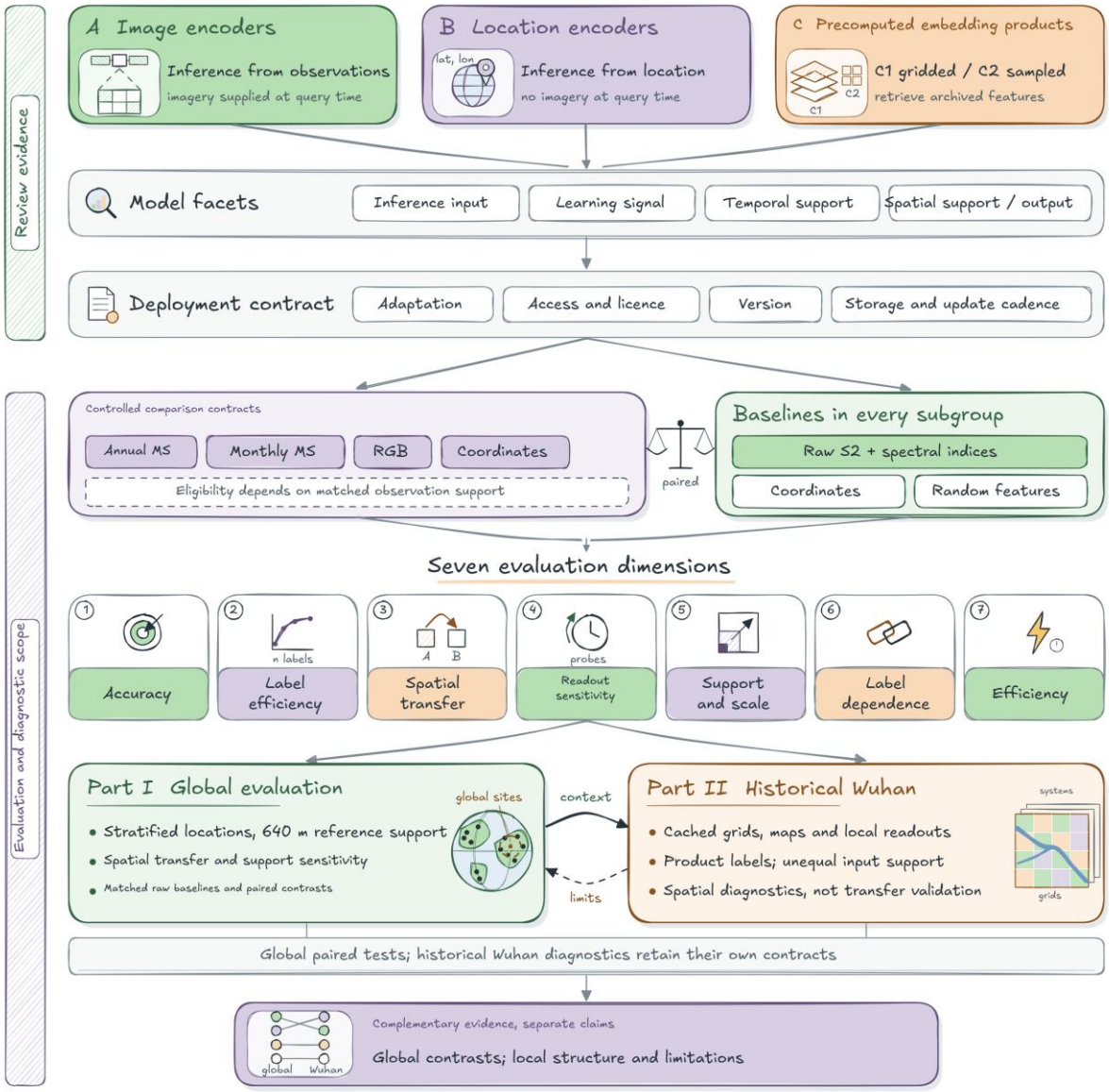


Figure 11. Review-to-evaluation framework aligned with the completed analysis. Release classes, model facets and deployment contracts define eligible matched global comparisons. Part I examines accuracy, label efficiency, spatial transfer, readout sensitivity, spatial support, label dependence and efficiency with matched raw-observation, coordinate and random-feature baselines. Part II retains the historical Wuhan caches as local spatial diagnostics: embedding appearance, grid maps, readout scores and paired controls. Its product labels and unequal input support do not provide independent dense validation or global-to-local ranking evidence. Global and historical local results retain separate comparison contracts and claims. Diagram construction used AI-assisted coding with OpenAI Codex and Anthropic Claude Code (October 2026 workflow); the editable artwork and provenance are retained.

Annual inputs required at least 95% original valid pixels at every evaluated support. For each calendar month, valid pixels were drawn from actual Sentinel-2 scenes in deterministic order, taking the first available clear observation at each pixel. Monthly composites required at least 90% original valid pixels in each of the twelve months; a nested 95% monthly sensitivity retained 2,830 locations. The validity mask accepted scene-classification categories 4–7 and 11, including unclassified surface and snow/ice. Residual invalid pixels were filled using that observation's per-band valid-pixel median, with the same resulting arrays used by all systems and image baselines. Missing months were not replaced by other months. Calendar-month identifiers or the fifteenth day of the month encoded the composite interval, not a common acquisition date for every pixel. The monthly threshold was fixed before the main predictive outcomes. The stricter sensitivity changes both quality threshold and cohort composition and therefore does not identify the effect of filling alone.

Twenty targets covered land cover, vegetation structure and water persistence. WorldCover 2021 (Zanaga et al., 2022) and Esri 2021 (Esri, 2022) were mapped to six classes: trees, low vegetation, crops, built, bare/snow and water. Each product supplied a dominant-class target and six within-footprint class fractions. Further targets were CCI 2021 aboveground biomass (Santoro & Cartus, 2024), ETH 2020 canopy height (Lang et al., 2023), quality-filtered 2021 GEDI rh98 and AGBD (Dubayah et al., 2020), and JRC 2021 water seasonality divided by 12 and averaged over valid pixels. The twentieth target was six-class classification restricted to locations where the two land-cover products' merged dominant labels agreed. JRC therefore measures temporal water persistence, not spatial water fraction. The six-class crosswalk retains the documented product definitions (Esri, 2022; Zanaga et al., 2022); fractions are aggregated at each evaluated support.

WorldCover, Esri, CCI, JRC and all twelve fractions retained the parent cohort counts. Annual/monthly availability was 3,910/2,790 for ETH, 2,127/1,785 for GEDI rh98,

1,441/1,178 for GEDI AGBD, and 3,507/2,235 for agreement-conditioned classification. ETH is explicitly a 2020 model-derived reference for 2021 imagery. GEDI targets retain their sampled footprint support; their available-pixel averages do not represent a complete inventory of every 640 m square. Table 7 records these target-specific denominators.

5.2 Evaluation protocol

Six baseline variants were constructed separately from each subgroup's input. B0 predicted the training-fold mean or majority class. B1 combined per-band statistics with NDVI, EVI, NDWI, MNDWI, NDBI and NBR; RGB controls used colour statistics and GLCM texture, while monthly controls used monthly features and Fourier harmonics. B2 encoded latitude/longitude, unit-sphere coordinates and angular sine/cosine terms. B3 used fixed Gaussian 3 × 3 convolutional filters, ReLU and spatial mean pooling at 1,024 and 4,096 dimensions. This was a MOSAIKS-style random-feature control, not a reproduction of its original sampling procedure. B4 concatenated B1 and B2. Monthly random filters received the ordered 120 month–band channels. NDVI and green–NIR NDWI follow their established spectral definitions (McFeeters, 1996; C. J. Tucker, 1979).

Embeddings remained frozen. Standardization and PCA were fitted only on training data, with both native dimensions and PCA-64 evaluated; feasible PCA rank was reduced when limited by training-set size. Logistic regression and ridge regression (Cox, 1958; Hoerl & Kennard, 1970) were the primary classification and regression readouts. kNN (Cover & Hart, 1967) and LightGBM tested readout dependence. Classification used fixed six-class macro-F1 and regression used R^2; these metrics were not pooled into a universal ranking.

Random evaluation comprised five-fold cross-validation repeated five times. Five-degree spatial-block and leave-one-continent-out (LOCO) cross-validation assessed geographic transfer. Shared source observations remained grouped in every split; geographic splits additionally excluded training footprints within 1,280 m of a held-out centre. Few-shot

experiments used shared nested subsets of 16, 32, 64, 128 and 256 total training locations per fold, plus all training locations. G2a and G3 footprint analyses used 160, 320, 640 and 1,280 m inputs with labels re-aggregated at each support. Footprint and monthly-quality sensitivities used the linear readout.

The headline quantity was Δ = score(embedding) − score(best matched baseline). Matching fixed the subgroup, target, footprint, readout, representation and split. Percentile intervals used 999 paired location-bootstrap draws, with every system evaluated on the same resampled locations and the strongest of the six baselines reselected within each draw. Repeated predictions for a location were kept together; random-CV scores averaged the five repeat-level scores. The intervals condition on fitted cross-validation models and retained reference values; models were not refitted during bootstrapping. They do not provide simultaneous inference across the result matrix or test differences between readouts, budgets or footprints. Observed winners are descriptive selections.

The product extension uses the pre-existing, source-verified 2021 GSE (64-dimensional) and TESSERA v1.1 (128-dimensional) features on the frozen 2,513-location common cohort. All eighteen systems and four reference controls (B0, B2, single-scene S2 B4 and monthly S2 B4) share target-specific locations, spatial five-fold and LOCO partitions, train-only standardization and native linear readouts. Training locations sharing either annual or monthly source groups with held-out locations are removed, in addition to the 1,280 m geographic buffer. WorldCover, Esri, CCI and JRC retain 2,513 locations; ETH retains 2,318. Product intervals use 999 paired spatial-block bootstrap draws, reselecting the strongest of the four controls; location-resampling sensitivity is also retained. This separately versioned comparison measures delivered-representation performance under differing input histories. The product sensitivity analyses use the same admitted features and native linear readouts (Figures 14–16). Nonlinear product readouts and matched GPU costs are not evaluated.

For GSE and TESSERA, label-efficiency analysis uses five repeats of random five-fold cross-validation, with shared nested training subsets of 16, 32, 64, 128, 256 and all available locations per fold. Both annual and monthly source groups are purged from training, and preprocessing is fitted within each training subset. Transfer contrasts subtract the existing spatial or LOCO reference delta from the random-CV delta on identical target-specific locations. Footprint sensitivity pools centred 16, 32 and 64 pixel windows from source-verified 10 m product grids, giving 160, 320 and 640 m supports. Both products must have at least 95% valid pixels at every support. Target labels are reaggregated to each footprint, and location cohorts and spatial partitions are fixed across supports. These curves use B0, B2 and same-support single-scene S2 B4 controls; the 640 m label comparisons use the four-control family defined above. Product intervals use 999 paired spatial-block bootstrap draws, retaining repeated predictions together and reselecting the strongest reference. The cached grids cover only 640 m, so no 1,280 m product point is estimated. Pooling support is not the receptive field of the provider encoder.

All 792 admitted evaluation jobs completed, producing 29,352 measured system cells and 326,202,930 out-of-fold prediction records. A separate 320-job location-encoder extension used the same evaluator on the annual and monthly cohorts. It contains 1,120 SatCLIP cells and 6,720 repeated baseline cells, which are kept separate from the original 29,352-cell count. All 3,360 native-feature baseline cells reproduced the published G2a or G2b values exactly; 27 of 3,360 PCA-64 baseline cells differed by at most 0.004 through the PCA solver. The original 29,352-cell total includes the separately identified strict monthly sensitivity. Coverage and integrity checks passed, and an independent reconstruction checked every published score against saved predictions and authoritative reference tables. Prediction records repeat locations across evaluation settings and are not independent sample counts. The complete result tables retain baseline failures and negative embedding deltas. The

common-cohort product extension completed a further 220 system-target-split evaluations, including the controls, with 544,280 saved out-of-fold prediction rows. Paired fold identities, annual and monthly source-group separation, readout convergence and scores recomputed with an independent metric implementation all passed. The product sensitivity extension adds 26 settings and 1,417,677 out-of-fold prediction rows; independent scoring, nested-budget identities and fixed footprint cohorts and partitions passed verification.

Centred linear CKA (Kornblith et al., 2019) and cosine-neighbour overlap at k = 20 use 2,513 common locations across 18 systems: fifteen scored image encoders, SatCLIP, GSE and TESSERA. The two products also enter the separate predictive extension; the geometry analysis itself assigns no predictive gain. CKA uses native unstandardized features and float64 accumulation. Cost records retain warm batch-one preprocessing and synchronized encoder execution on the shared RTX 4090 environment, peak allocated VRAM and native float32 vector storage.

The Wuhan study uses 567 adjacent 500 m tiles. Its fixed split and twenty repeated local splits measure different aspects of within-window readout and partition sensitivity. They complement the global analysis but do not independently validate its geographic transfer or provide a common model ranking.

Wuhan T1 linearly probes four WorldCover dominant classes from pooled tile embeddings; T2 uses validation-selected ridge for four fractions. Their fixed 341/113/113 split yields a final T2 fit on 454 training/validation representations after train-only standardization. T3 uses a tile-level binary head, JRC fraction threshold 0.5 and validation-IoU stopping. T4 uses four cached blocks: training pixels supply class prototypes, validation pixels calibrate thresholds, and test pixels are evaluated on native representation grids. Different grids, resampled labels and prompt counts preclude a matched-pixel or zero-shot interpretation. These four archived readouts ask different questions even within one window:

dominant tile class, continuous fraction, binary tile water and dense native-grid labels are distinct outcomes. Their original training, validation and testing roles are retained; the subsequent repeated-split controls do not overwrite the historical fixed-split results.

5.3 Global performance

The final annual and monthly cohorts exceeded 3,000 locations but represented different observation-availability filters (Figure 12). The annual cohort contained 1,398 tree, 1,782 low-vegetation, 503 crop, 27 built, 612 bare/snow and 87 water locations; the monthly cohort contained 548, 1,247, 345, 17, 815 and 42, respectively. Retaining all six classes in macro-F1 prevented dominant classes from determining the metric alone, although sparse built and water samples constrain interpretation. ETH and GEDI coverage further changed the evaluated population (Table 7). Accordingly, comparisons below are within input subgroup and target, rather than rankings of modalities or estimates of area-weighted global map accuracy.

WorldCover (Zanaga et al., 2022) and Esri (Esri, 2022) provide alternative land-cover references. The CCI biomass (Santoro & Cartus, 2024) and ETH canopy-height (Lang et al., 2023) results quantify reconstruction of those products. Their source dependence and target-specific coverage constrain ecological interpretation, as discussed in Section 6.3.

Table 7. Global comparison groups and target-specific coverage at 640 m.

Group / systems	Parent n	ETH	GEDI rh98	GEDI AGBD	Agreement
G2a / 7 multispectral + SatCLIP (B)	4,409	3,910	2,127	1,441	3,507
G2b / 3 monthly + SatCLIP (B)	3,014	2,790	1,785	1,178	2,235
G3 / 5 RGB	4,409	3,910	2,127	1,441	3,507
Product extension / 18 systems incl. GSE, TESSERA (C1)	2,513	2,318	—	—	—

Group / systems	Parent n	ETH	GEDI rh98	GEDI AGBD	Agreement
GSE/TESSERA label sensitivity (C1)	2,513	2,318	1,468	—	1,939
Not eligible / SatVision-TOA (A2), Copernicus-Embed (C1)	Unavailable	—	—	—	—

Within each G2a, G2b or G3 subgroup, all systems and six baseline variants share target-specific locations. WorldCover, Esri, CCI, JRC and the twelve fractions retain parent counts; the strict monthly sensitivity has 2,830 locations. The primary product extension refits eighteen systems and four controls on 2,513 common locations, with 2,318 for ETH. The additional GSE/TESSERA label sensitivity has 1,468 GEDI rh98 and 1,939 agreement-conditioned locations; GEDI AGBD is not evaluated for these products. Annual, monthly and extension cohorts overlap and must not be added as distinct locations. Product results measure practical performance under different input histories. SatVision and Copernicus remain unavailable for support-matched 640 m global prediction.

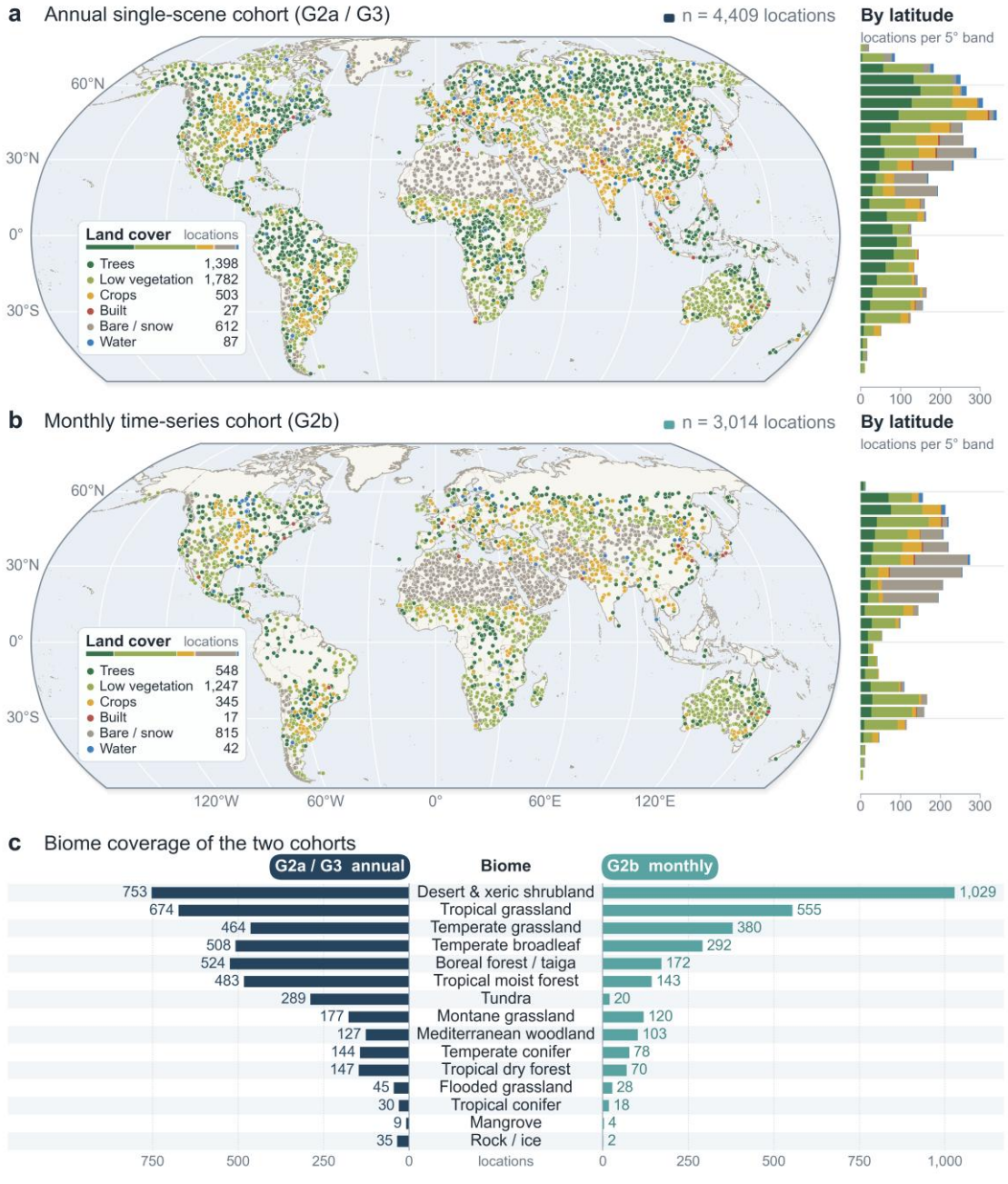


Figure 12. Global evaluation cohorts and biome coverage. The annual cohort contains 4,409 locations shared by G2a and G3; the monthly cohort contains 3,014 G2b locations. Panels a and b map the cohorts in a Robinson projection, with colours indicating merged WorldCover classes; side bars count locations per 5° latitude band. Panel c compares biome counts between the two cohorts. Biome–land-cover stratification, a 200 km Wuhan exclusion and input/target availability define these populations. Monthly availability changes their composition; the sample does not estimate area-weighted global map accuracy.

The G2a, G2b and G3 blocks of Figure 13 and Table 8 report primary spatial-CV contrasts at 640 m with native features, linear readouts and all training labels. The largest observed WorldCover delta was +0.1106 [0.0646, 0.1374] for TerraMind in G2a, +0.0977 [0.0500, 0.1374] for Galileo in G2b, and +0.1046 [0.0671, 0.1408] for SatMAE++ RGB in G3. Individual intervals were wholly positive for only three of seven G2a, one of three G2b and two of five G3 systems. Positive best-system results therefore did not establish a subgroup-wide advantage.

For CCI biomass, TerraMind reached $R^2 = 0.8092$ against B4 at 0.6519, giving Δ = +0.1573 [0.1404, 0.1732]. Galileo's G2b contrast was +0.3746 [0.2477, 0.5415], and SatMAE++ RGB's G3 contrast was +0.2166 [0.1901, 0.2442]. These gains show that the frozen representations retained useful predictive information beyond their matched controls for this reference. Their different baselines and populations prevent interpreting the delta magnitudes as a ranking across groups.

The positive G2a pattern also extended to Esri classification and JRC water persistence: TerraMind's spatial deltas were +0.1348 [0.0987, 0.1546] and +0.2380 [0.1954, 0.2851], respectively. For GEDI rh98, TerraMind reached $R^2 = 0.6527$ against B1 at 0.5518, giving Δ = +0.1009 [0.0527, 0.1453] on 2,127 locations. It was the only G2a system with a wholly positive spatial rh98 interval; the other six intervals were wholly negative. Useful height-

reference information was therefore accessible in a selected representation without extending to the full multispectral subgroup.

GEDI AGBD gave a contrasting result. Every G2a and G3 embedding had an individual interval wholly below zero in all three splits under the primary native linear readout. Even the observed spatial winners lost: TerraMind had $R^2 = -0.0710$ and $\Delta = -0.2919$ [−0.7308, −0.1309]; WildSAT had $R^2 = -0.0691$ and $\Delta = -0.1978$ [−0.4665, −0.1081], each on 1,441 locations. The failure was readout-specific: native LightGBM yielded a positive TerraFM contrast of +0.0539 [0.0143, 0.1534], with $R^2 = 0.2559$ versus B4 at 0.2021. Thus information accessible to a nonlinear readout cannot be inferred solely from the primary linear result.

SatCLIP, the location encoder, did not exceed the strongest matched baseline for WorldCover. Under spatial CV its annual macro-F1 was 0.4865 against B3-1024 at 0.6533, giving $\Delta = -0.1667$ [−0.2157, −0.1313]; the monthly contrast was −0.2306 [−0.2823, −0.1826]. On the annual cohort, where the controls summarize one 12-band acquisition, 18 of 20 spatial intervals were wholly negative and none was wholly positive. On the monthly cohort, whose controls are ten-band monthly summaries, 6 intervals were wholly positive, 7 wholly negative and 7 included zero; the positive cases were crop, low-vegetation and bare/snow fractions and GEDI rh98 ($\Delta = +0.1879$ [0.0954, 0.2389]), for which the coordinate control B2 was itself the strongest baseline. SatCLIP exceeded B2 for 14 annual and 14 monthly targets, for example by +0.2404 in annual WorldCover macro-F1. The learned location representation therefore supported better prediction than the specified raw-coordinate features on most targets, while positive intervals against the strongest of all six baselines were confined to six monthly-cohort targets.

The added product block in Figure 13 reports the separate common-cohort comparison. Spatial WorldCover macro-F1 was 0.8466 for GSE and 0.8119 for TESSERA, against 0.7088

for the strongest reference control, monthly S2 B4. Their differences were +0.1378 [0.0985, 0.1782] and +0.1032 [0.0586, 0.1455], respectively. Both products had individually positive reference-difference intervals for all five targets under spatial CV and LOCO. These are conditional, non-simultaneous intervals against the four specified controls. The complete eighteen-system common-cohort scores are retained with the extension; comparing these product deltas directly with the original subgroup deltas would conflate cohorts, input histories and baseline families.

Table 8. Selected native linear spatial-CV contrasts at 640 m, with all training labels.

Group / target	**System (n)**	**Score**	**Best baseline**	**Δ [95% CI]**
G2a / WorldCover	TerraMind (4,409)	0.7638	B3-1024: 0.6533	+0.1106 [0.0646, 0.1374]
G2b / WorldCover	Galileo (3,014)	0.8085	B4: 0.7108	+0.0977 [0.0500, 0.1374]
G3 / WorldCover	SatMAE++ RGB (4,409)	0.6384	B3-4096: 0.5338	+0.1046 [0.0671, 0.1408]
G2a / CCI	TerraMind (4,409)	0.8092	B4: 0.6519	+0.1573 [0.1404, 0.1732]
G2b / CCI	Galileo (3,014)	0.6985	B4: 0.3239	+0.3746 [0.2477, 0.5415]
G2a cohort / WorldCover	SatCLIP, B (4,409)	0.4865	B3-1024: 0.6533	−0.1667 [−0.2157, −0.1313]
G2a cohort / CCI	SatCLIP, B (4,409)	0.4412	B4: 0.6519	−0.2106 [−0.2470, −0.1795]
G2b cohort / WorldCover	SatCLIP, B (3,014)	0.4802	B4: 0.7108	−0.2306 [−0.2823, −0.1826]
G2b cohort / CCI	SatCLIP, B (3,014)	0.2979	B4: 0.3239	−0.0260 [−0.1546, 0.1236]
G3 / ETH	RemoteCLIP (3,910)	0.6867	B4: 0.4789	+0.2078 [0.1880, 0.2289]
G2a / AGBD	TerraMind (1,441)	−0.0710	B4: 0.2209	−0.2919 [−0.7308, −0.1309]
G3 / AGBD	WildSAT (1,441)	−0.0691	B4: 0.1287	−0.1978 [−0.4665, −0.1081]

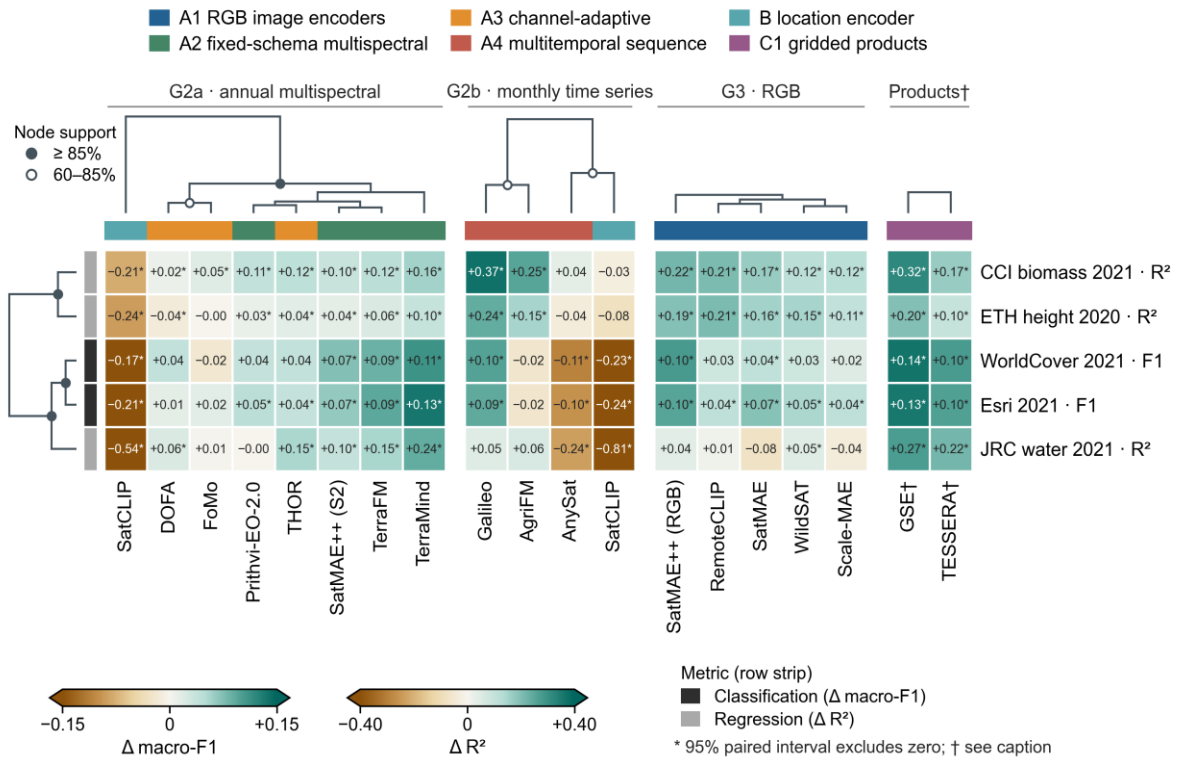


Figure 13. Embedding differences from reference baselines, shown as a clustered heatmap with separate input-comparison and product blocks. All cells use 640 m support, native features, linear readouts, spatial CV and all training labels. G2a, G2b and G3 report differences from the strongest of six subgroup baselines, reselected in 999 paired location-bootstrap draws; SatCLIP shares the G2a and G2b cohorts but receives coordinates only. The separated product block (†) shows GSE and TESSERA on 2,513 common locations (2,318 for ETH), relative to the strongest of four refitted controls: B0, B2, single-scene S2 B4 and monthly S2 B4. Its 999 paired spatial-block bootstrap draws reselect that reference. Product inputs are not matched to the controls; these are practical reference contrasts, not same-input gains. Asterisks mark intervals excluding zero using unrounded bounds. Colour retains signed differences on the original scales (macro-F1 clipped at ±0.15, R^2 at ±0.40); strips identify metric and release class. Ward trees for targets and G2a/G2b/G3 systems use row-standardized profiles of those seventeen columns; systems are clustered only within their subgroup. Filled/open circles mark at least 85%/60–85% recovery in 2,000 normal-perturbation draws; support is approximate because cells share locations. The two products form a separate branch. Table 7 supplies subgroup and product-extension counts, and Table 8 selected subgroup intervals. JRC measures water persistence; ETH is a 2020 reference. SatVision and Copernicus lack source-verified,

support-matched 640 m global inputs. Intervals condition on fitted models and are not simultaneous. Different input histories, cohort sizes, comparator families and resampling units preclude interpreting the blocks as a common ranking.

5.4 Label efficiency and transfer

Under repeated random CV, TerraMind's G2a WorldCover delta increased from +0.0505 [0.0378, 0.0620] with 16 training locations per fold to +0.1087 [0.0751, 0.1332] with all training locations (Figure 14). In contrast, AnySat's G2b CCI biomass intervals were wholly negative throughout budgets 16–256; its 256-label delta was −0.3807 [−0.5671, −0.2388], compared with +0.2062 [0.0149, 0.3219] at all-training. Frozen pretraining therefore did not guarantee an advantage in the low-label regime.

The corresponding secondary-readout results also constrain conclusions about representation quality. Galileo's positive native linear spatial WorldCover contrast became a native kNN delta of −0.0294 [−0.0770, 0.0239]. Training budget, feature dimension and the strongest baseline all affect delta. The curves describe each fixed representation–readout setting; neither non-monotonicity nor differences between interval endpoints constitute a formal test of changes across budgets or readouts.

The product block adds a distinct low-label pattern. With 16 training locations per fold, GSE had a WorldCover reference delta of +0.0453 [0.0257, 0.0629], whereas TESSERA had −0.0227 [−0.0418, −0.0043]. At all-training, their deltas were +0.1440 and +0.1042. These contrasts use the product-specific common cohort and four reference controls; they do not establish a ranking against the separate image-encoder cohorts.



Figure 14. Label efficiency relative to reference baselines. Native linear readouts use five repeats of random five-fold CV and shared nested budgets of 16–256 total training locations per fold; All is a separate category. (a–i) G2a, G2b and G3 use their six subgroup baselines. Black stars mark SatCLIP,

which shares the G2a and G2b cohorts, folds and references. (j–l) GSE and TESSERA use 2,513 common locations (2,318 for ETH) and four refitted controls: B0, B2, single-scene and monthly S2 B4. The product block (†) measures practical performance under different input histories. Shading and bars show paired 95% intervals, reselecting the strongest reference and retaining repeated predictions together: location resampling for the original subgroups and spatial-block resampling for the products. Intervals condition on fitted models and do not test changes across budgets. Different cohorts, inputs and reference families preclude a common cross-block ranking.

Figure 15 separates geographic changes in baseline-relative advantage from changes in absolute prediction. Galileo's G2b CCI R^2 decreased from 0.7028 under random CV to 0.6985 under spatial CV and 0.6238 under LOCO. Delta nevertheless rose from +0.5080 under random CV to +0.6631 under LOCO because the best baseline fell from 0.1947 to −0.0392. A larger transfer delta can therefore accompany poorer absolute prediction. Figure 15 reports point differences between protocols; it does not assign a paired causal interval to the transfer drop.

Readout dependence was pronounced in the same LOCO target. LightGBM increased Galileo's R^2 to 0.7262, but increased the strongest baseline to 0.7819, reversing delta to −0.0558 [−0.0913, −0.0184] from the linear value of +0.6631 [0.3943, 0.6869]. GEDI AGBD exposed a further transfer limitation: Galileo's spatial delta was +0.0519 [0.0100, 0.2518], with a low absolute R^2 of 0.0539, whereas its LOCO delta was −0.4870 [−2.5590, −0.1885]. Geographic robustness must therefore be assessed jointly from the embedding score, matched baseline and reference target.

For both products, random-to-spatial loss of delta was small on WorldCover (+0.0062 for GSE and +0.0010 for TESSERA). On CCI, random minus LOCO delta was negative (−0.2373 and −0.1485), indicating a larger reference-relative advantage under LOCO, not an improvement in absolute ecological accuracy. These point differences share exactly the same target-specific locations and are not significance tests.

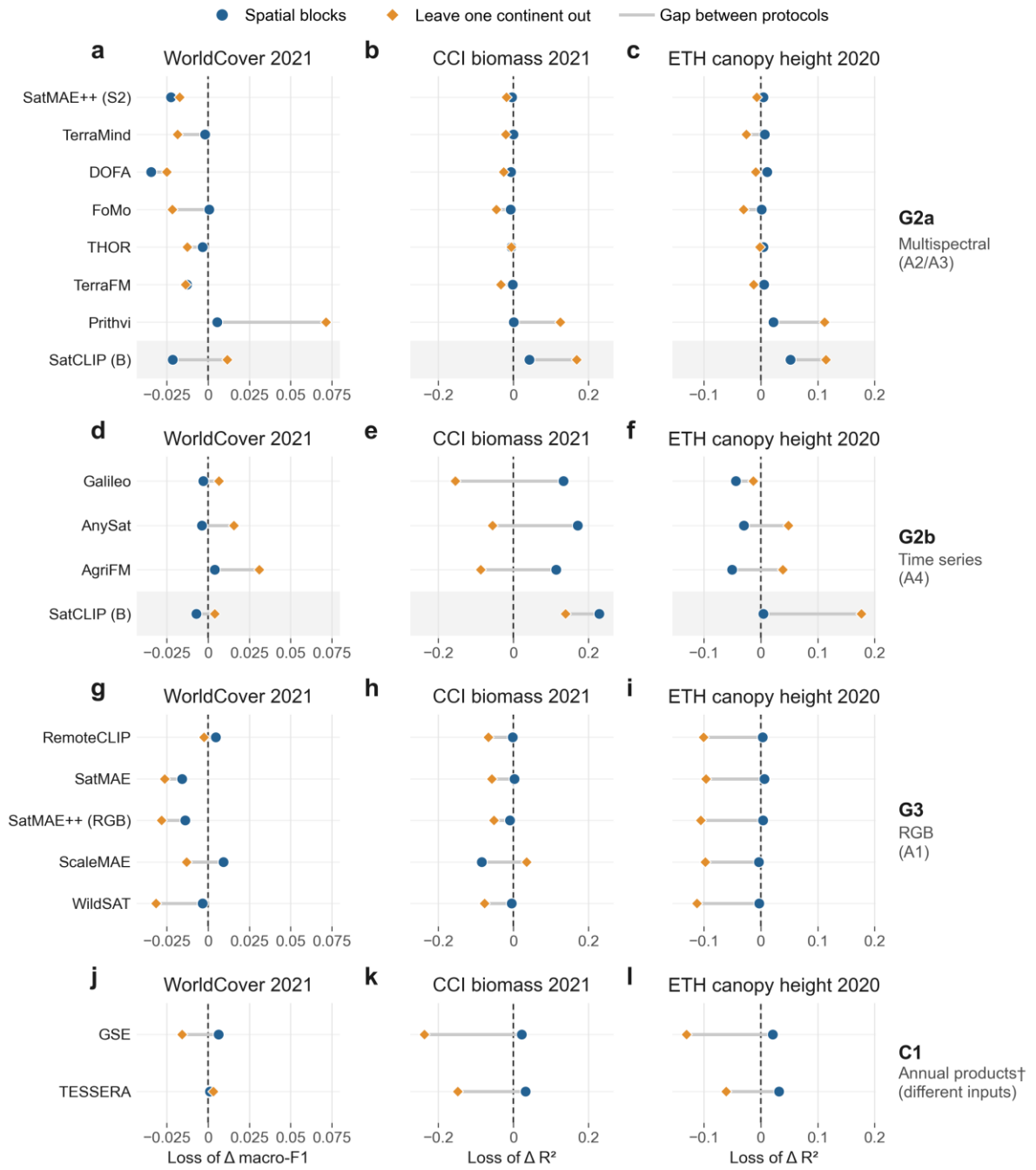


Figure 15. Change in baseline-relative advantage under geographic transfer. Points show random-CV Δ minus spatial-block or leave-one-continent-out Δ. Positive values indicate narrowing advantage; each protocol selects its own strongest reference. Target-specific locations, support, representation and readout are fixed within each comparison. Source groups are purged from training, with a 1,280 m exclusion buffer in geographic splits. These are point differences without confidence intervals for the transfer difference. Absolute embedding and baseline score drops are retained with the results. SatCLIP appears in the G2a and G2b rows. The C1 product row (†) adds GSE and TESSERA on

2,513 locations (2,318 for ETH), using B0, B2, single-scene and monthly S2 B4 controls; both annual and monthly source groups are purged. Different inputs, cohorts and reference families preclude a common ranking across blocks.

5.5 Spatial support and references

On the same 4,400-location WorldCover footprint cohort, TerraMind's spatial native linear delta increased from +0.0584 [0.0254, 0.0802] at 160 m to +0.1340 [0.0904, 0.1667] at 1,280 m; DOFA's intervals included zero at all four supports (Figure 16). Because both input context and aggregated reference support changed, this pattern cannot isolate a causal benefit of larger image context. Extreme failures remain visible: ScaleMAE at 160 m on the paired spatial CCI target had $\Delta = -87.9544$ [−278.6438, 0.2666], whose interval includes zero. Full-range panels retain this result alongside labelled detail views.

Fraction targets likewise mixed gains and failures. Spatial examples were +0.3963 [0.2853, 0.4658] for G2a SatMAE++ S2 on WorldCover built fraction and +0.5235 [0.3793, 0.5540] for G2b Galileo on WorldCover crop fraction. Conversely, AgriFM's spatial WorldCover built delta was −0.8531 [−1.6802, −0.4049]. Agreement-conditioned classification produced positive observed winner contrasts in all three groups, yet AnySat's spatial delta remained negative at −0.1174 [−0.1736, −0.0750]. Product agreement selects a different population and does not independently validate labels; the twelve fractions are compositional within products and correlated across them.

GSE and TESSERA also enter the footprint and reference-label comparisons. Their support curves use fixed cohorts of 2,508 WorldCover and 2,513 CCI locations at 160, 320 and 640 m. Only the pooled product features and aggregated references change support; the provider encoder context is not manipulated. The 1,280 m points remain unavailable because the admitted product grids contain no pixels beyond 640 m. At 640 m, GEDI rh98 reference deltas were +0.2736 [0.2246, 0.3312] for GSE and +0.0823 [0.0342, 0.1274] for TESSERA

on 1,468 locations. Agreement-conditioned land-cover deltas were +0.1616 [0.1243, 0.1978] and +0.1280 [0.0851, 0.1646] on 1,939 locations. Positive contrasts with these reference products do not supply independent ecological validation.

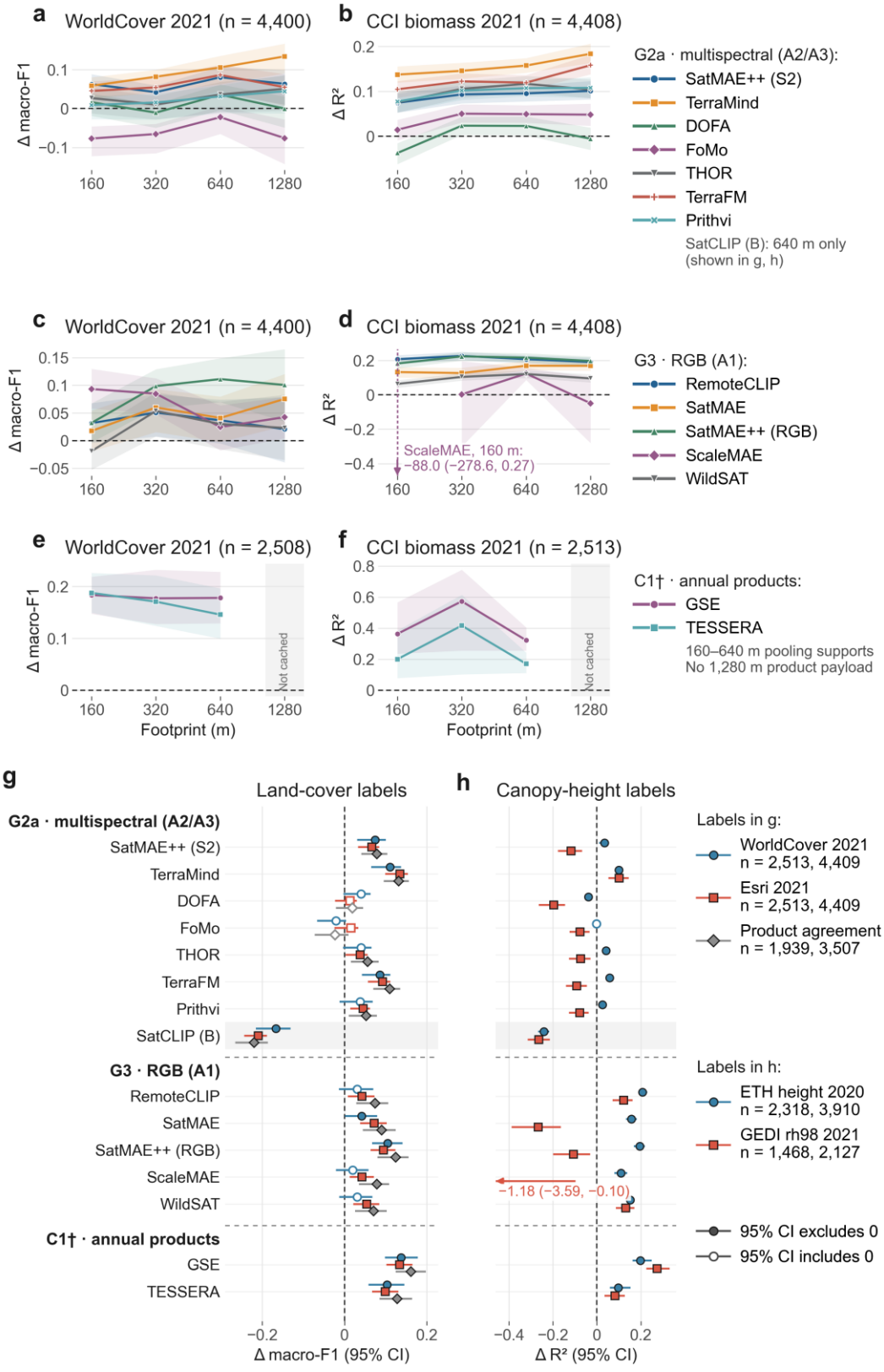


Figure 16. Footprint and reference-label dependence. (a–d) G2a and G3 support curves use 4,400 WorldCover or 4,408 CCI locations and fixed partitions across 160–1,280 m; inputs and labels both change support. (e, f) GSE and TESSERA use 2,508 WorldCover or 2,513 CCI locations at 160, 320 and 640 m, with fixed spatial partitions, reaggregated labels and B0, B2 and same-support single-scene S2 B4 references. Their 1,280 m points are marked Not cached; pooling support does not represent encoder receptive field. (g, h) At 640 m, WorldCover, Esri, their agreement subset, ETH 2020 height and GEDI 2021 rh98 are compared at their actual coverage. Products use four references including monthly S2 B4. Open symbols mark intervals including zero. Native linear spatial-CV intervals use paired location resampling for G2a/G3 and paired spatial-block resampling for C1, reselecting each block's strongest reference. Product agreement is not independent validation. Arrows and printed intervals retain the two ScaleMAE values outside the plotted windows. SatCLIP appears in g and h at 640 m only. The C1 product block (†) has different inputs and comparator families and is not a common ranking with the image encoders.

5.6 Geometry and efficiency

Figure 17 compares centred linear CKA and cosine-neighbour overlap for all 18 systems with 640 m support on the common 2,513-location cohort: 15 image encoders (class A), SatCLIP (B) and the GSE and TESSERA products (C1). The 16- and 17-system extensions share this exact cohort; joining them adds only the SatCLIP–GSE and SatCLIP–TESSERA pairs, and every previously computed pair reproduces (maximum CKA difference 1.2×10^{-15}; identical neighbour overlap). SatMAE–ScaleMAE had the largest observed CKA, 0.855614, while their mean 20-neighbour overlap was 0.282511. High representation similarity is therefore a descriptive property, not evidence of equal task performance or robustness. SatCLIP's CKA with the image encoders ranged from 0.152 to 0.409. Among the 153 distinct pairs, GSE–TESSERA had the highest neighbour overlap (0.464306; CKA = 0.421894), followed by SatCLIP–GSE (0.401015; CKA = 0.515565, GSE's largest CKA with any system). Averaged by class, both products shared more local neighbours with the location

encoder (0.401 for GSE, 0.283 for TESSERA) than with the image encoders (0.141 and 0.143), indicating similar local-neighbour structure in these feature spaces. This comparison does not isolate geographic position from the spatial distribution of environmental conditions. These descriptive comparisons do not establish controlled predictive gains for B or C1.

The efficiency panels retain separate within-subgroup point-estimate Pareto fronts. Measured costs comprise warm batch-one encoder latency on the shared RTX 4090 environment, process-allocated peak VRAM and native float32 vector bytes. Timing includes preprocessing and synchronized encoder execution but excludes acquisition, payload loading and readout fitting; concurrent host activity was not isolated. These measurements quantify the observed inference setting and storage burden, without claiming deployment throughput or end-to-end acquisition cost.

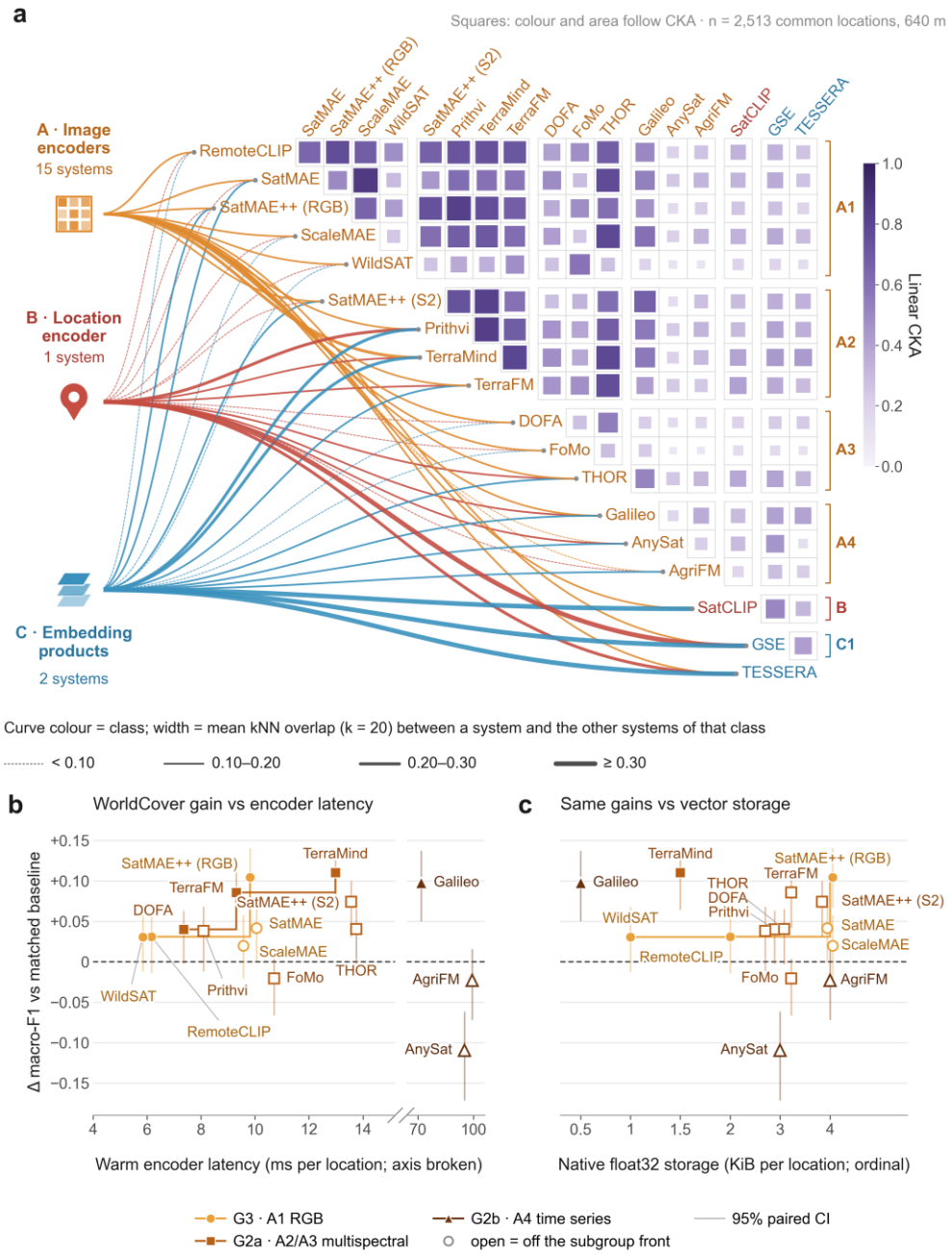


Figure 17. Representation similarity and measured efficiency. (a) Upper triangle of centred linear CKA for the 18 benchmarked systems with 640 m support on 2,513 common locations; square colour and area follow CKA, and brackets mark subclasses. Curves link each class (A image encoders, B location encoder, C precomputed embedding products) to every system; curve width bins the mean cosine 20-neighbour overlap between that system and the other members of the class (dashed below 0.10). Self pairs are excluded, so B has no curve to SatCLIP. (b, c) Native linear spatial WorldCover Δ against warm encoder latency (broken axis) and native float32 vector storage (ordinal classes; systems with equal storage are offset horizontally). Vertical lines are paired 95% intervals; staircases

are within-subgroup point-estimate Pareto fronts, and open markers lie off their front. SatCLIP, GSE and TESSERA have no matched GPU cost record and are absent from b and c. Timing includes preprocessing and synchronized encoding, excludes acquisition/loading/readout fitting, and was not isolated from concurrent host activity.

5.7 Wuhan case study

The Wuhan experiment uses 567 adjacent 500 m tiles. Its historical split has 341 training, 113 validation and 113 test tiles. The original 19-system records and prompt counts remain in Supplementary Methods S4; the SatCLIP extension increases the current catalogue to 20 systems. SatCLIP was added on 9 October 2026 with the same frozen split, using only tile-centre coordinates. Retrospective audit confirms Scale-MAE's centre crop reduced input support while exported arrays retained the full bounding box without crop offsets; per-axis coverage depends on aspect ratio. SatMAE intensity-scaling effects remain unresolved. Archived orderings therefore do not establish matched support/preprocessing; the raw-observation–GSE pairing has separate provenance.

Figure 18 shows the historical Wuhan window and, for every cached system, the first three principal components of its own embedding grid. The contrast between 10 m C1 fields, patch-token grids and SatCLIP's smooth coordinate field makes differences in spatial support visible before any readout is fitted; colours are not comparable between systems.

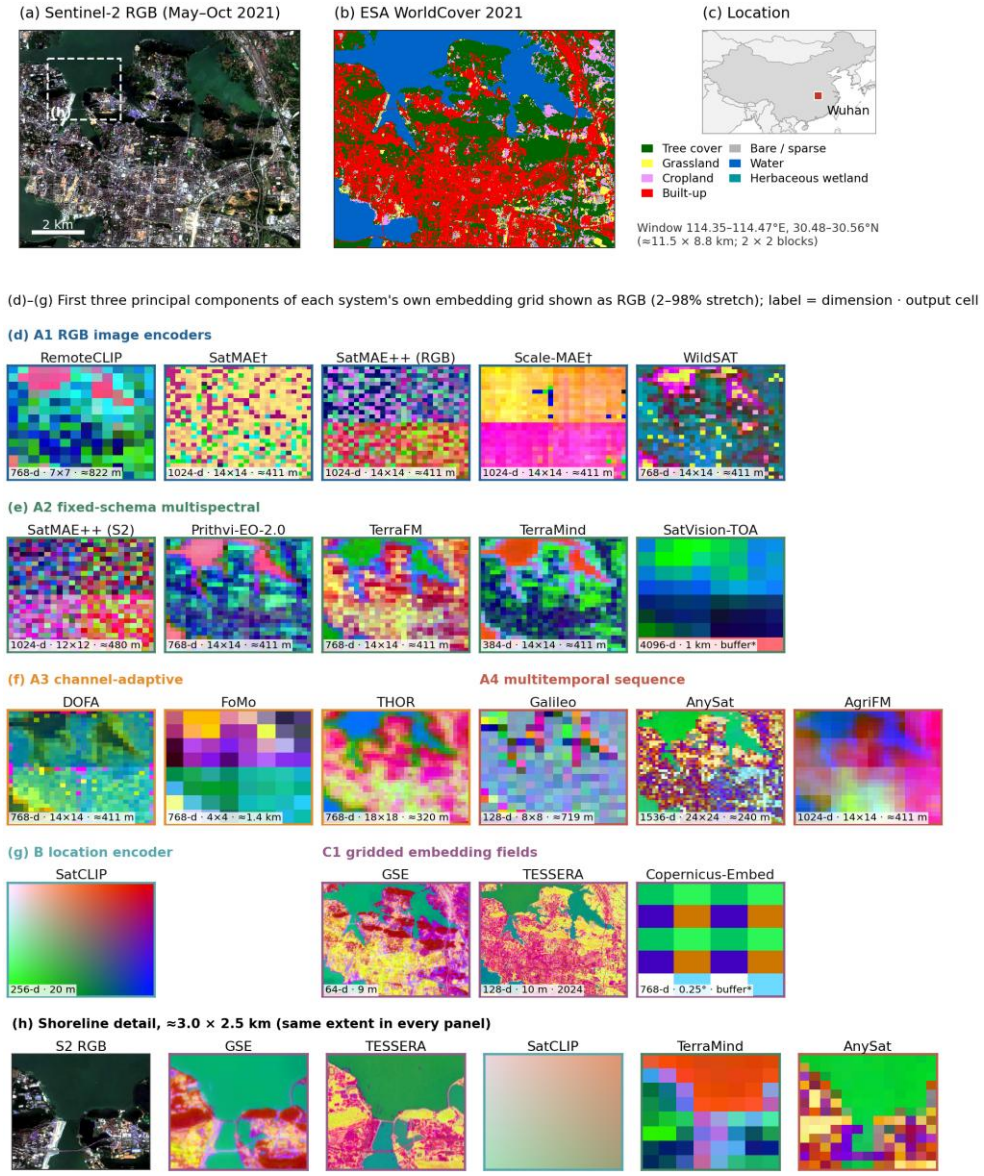


Figure 18. Historical Wuhan window and map-level appearance of the 20 cached representations. (a) Sentinel-2 RGB median composite for May–October 2021 and (b) ESA WorldCover 2021 in its original map legend, before aggregation to the four historical Wuhan target classes, over the 2 × 2-block window (114.35–114.47°E, 30.48–30.56°N; about 11.5 × 8.8 km); (c) location. (d)–(g) For each system, the first three principal components of its own cached embedding grid over the same window are shown as RGB with a 2–98% stretch per component. PCA was fitted separately for every system on up to 200,000 of its own valid cells, so colours are not comparable between panels; only spatial structure is. Frames and headings follow the frozen release classes (A1–A4 image encoders, B location encoder, C1 gridded embedding fields). Labels give the embedding dimension, the output grid per block and the approximate output cell implied by that grid; image encoders received each

block (about 5.8 × 4.4 km) resized to their input size, so their token cells (about 240 m–1.4 km) are set by the adapter configuration rather than by a native product resolution. Asterisks mark SatVision-TOA (1 km MODIS input) and Copernicus-Embed (0.25° product), whose grids were sampled with 3 km and 15 km buffers and are not co-registered with the window. The cached TESSERA map layer is the 2024 product, whereas the other dated inputs refer to 2021; SatCLIP has no temporal input. SatCLIP receives only the coordinates of a 20 m grid, so its smooth gradient shows location dependence rather than land-surface content. (h) The same 3.0 × 2.5 km shoreline extent in six panels shows the difference between 10 m fields, a 20 m coordinate grid and patch-token outputs. † Quarantined adapters (SatMAE, unresolved radiometric provenance; Scale-MAE, confirmed crop/bounding-box support mismatch). The panels are visual diagnostics, not accuracy measures, and imply no ranking.

Figures S8 and S9 map the fixed-split tile predictions and the native-grid prototype predictions of every system beside the reference; training tiles in Figure S8 are in-sample fits. In Figure S10, fixed-split tile macro-F1 is 0.890 (GSE), 0.836 (AnySat) and 0.830 (TESSERA). The four classes include just five cropland tiles, making macro-averages sensitive to very few examples. Figure S10 keeps each metric as a separate row instead of collapsing the metrics into one aggregate ordering; its dendrograms group similar score profiles and do not rank systems. They characterize the archived pipelines under their original local conditions; displaying all systems does not certify equal extraction support or independently validate the unquarantined adapters.

Four-target mean Spearman is 0.881 (GSE), 0.866 (TESSERA) and 0.852 (THOR). SatCLIP reaches macro-F1 0.408, above only Copernicus and the three SatMAE-family representations, and Spearman 0.598 (built-up) to 0.285 (vegetation). Its embedding varies only slightly within the window, so these random-split scores mainly reflect interpolation between adjacent tiles (Figures 18g and S8). Figure S10b shows built-up, vegetation, cropland and water separately; their mapped fractions are not independent field

measurements or a task-independent quality score. Supplementary Figure S7 preserves reference-versus-prediction scatter plots for six illustrative systems on the 113 fixed test tiles.

The pooled-tile supervised binary water head (Figures S8b and S10c) yields IoU 0.895 (DOFA), 0.868 (THOR) and 0.846 (TerraMind) on 36 water and 77 non-water test tiles. These labels do not measure dense shoreline recovery. SatCLIP's water IoU is 0.394.

Native-grid class prototypes (Figures S9 and S10d) yield mean IoU 0.615 (GSE), 0.503 (TESSERA) and 0.402 (AnySat). Different grids and prototype counts prevent common-pixel interpretation. SatCLIP, evaluated on a 20 m coordinate grid, reaches mean IoU 0.090. In the separate binary prompt/threshold diagnostic, FoMo IoU 1.000 used three positive and 22 negative prompts. Supplementary Methods S4 records all prompt counts and the JRC rule; no prompt-budget-independent ordering follows.

The cache-only controls use 20 deterministic stratified seeds, 339/114/114 splits (distinct from the fixed 341/113/113 split), and 400 test-tile bootstrap resamples per run. After adding SatCLIP, the merged records contain 440 classification rows, 1,760 regression rows, 22 row-block rows, 115 dimension-sensitivity rows, eight label-sensitivity rows and 190 geometry pairs. The original rows are preserved; the SatCLIP extension adds only its own records. Figures S11a and S11b show each system and target in release-class order, with quarantined adapters marked. Whiskers show one sample SD across the reused-data splits, not uncertainty across independent regions. Comparing systems requires paired scores because marginal whiskers do not describe uncertainty in a difference.

Repeated macro-F1 (mean $\pm$ SD) is 0.7785 ± 0.1124 (GSE), 0.7341 ± 0.0775 (raw Sentinel-2), 0.7315 ± 0.1169 (TerraMind) and 0.7159 ± 0.0845 (TESSERA). GSE–raw is $+0.0444$ (95% paired-bootstrap interval $[-0.0092, 0.0969]$, sign-flip $p = 0.1482$, original-family BH $q = 0.1743$). Nondetection is not equivalence; the interval permits a practically relevant positive difference. Four-target mean Spearman is 0.8803 ± 0.0103 (GSE),

0.8756 ± 0.0120 (raw), 0.8628 ± 0.0143 (TESSERA) and 0.8448 ± 0.0145 (THOR). GSE–raw is $+0.0047$ (95% interval $[-0.0016, 0.0104]$, $p = q = 0.1559$); TESSERA–raw is -0.0128 ($q = 0.0027$).

Tests use 100,000 sign flips and 10,000 bootstrap resamples of 20 paired seed differences, with Benjamini–Hochberg correction within metric. They differ from 400 within-run test-tile resamples and Supplementary Figure S4's seed quantiles. The original 20-comparison family includes both suspect adapters. Retrospectively excluding SatMAE/Scale-MAE leaves 18 comparisons and GSE $q = 0.1778/0.1559$ for classification/regression, without changing conclusions. This is a sensitivity, not a prespecified family. Raw/GSE features were separately verified. Reused local tiles make these intervals split sensitivity rather than independent-region uncertainty. Figures 19a and 19b pair the same splits, while retaining the different raw-observation and precomputed-product information contracts.

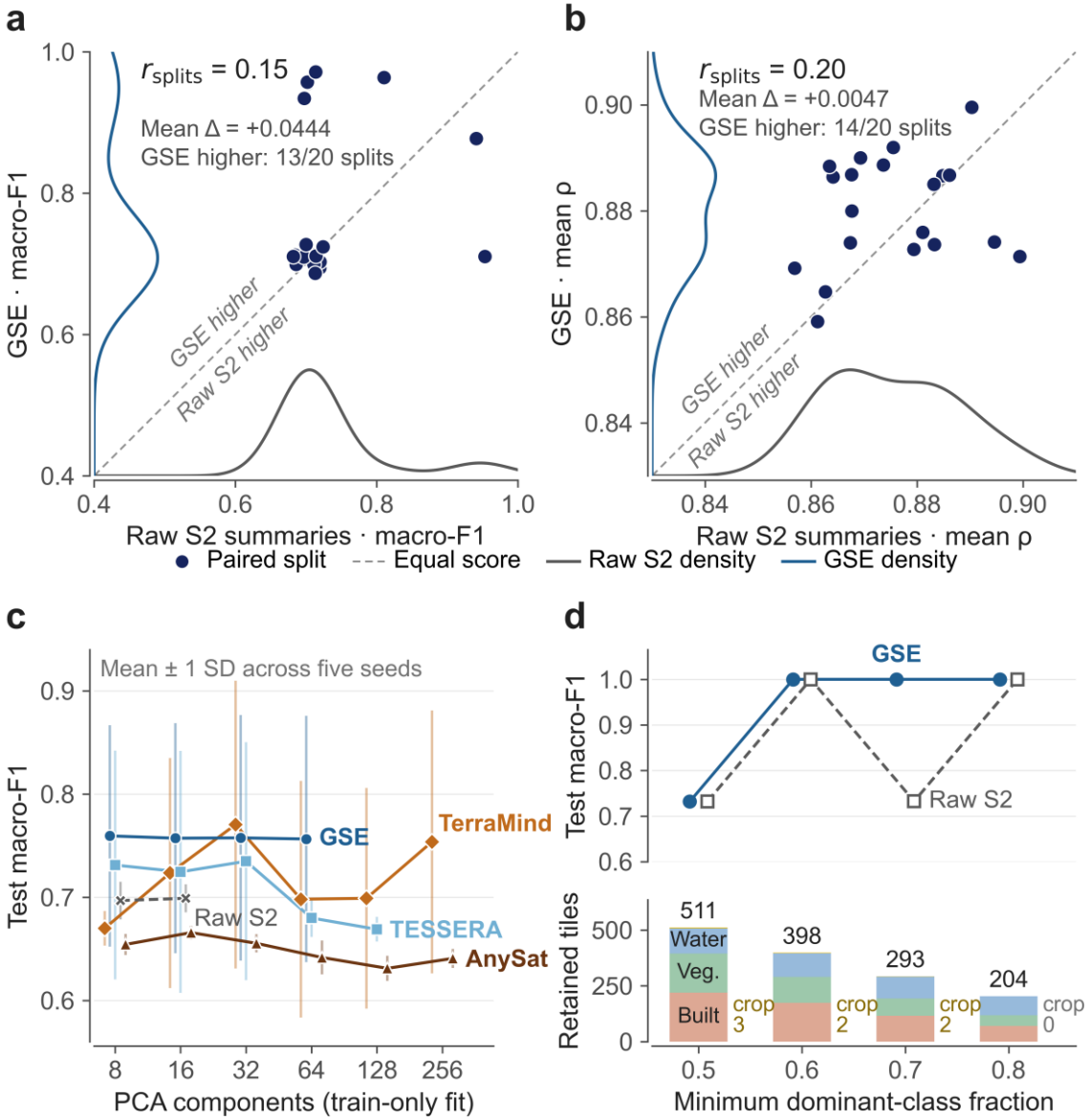


Figure 19. Paired controls and sensitivity analyses in the Wuhan window. (a, b) GSE versus raw Sentinel-2 summaries on the same 20 reused-data splits of 567 tiles: (a) land-cover macro-F1 and (b) mean Spearman correlation over four fraction targets. The dashed identity line marks equal scores; r_splits is the Pearson correlation between paired scores across splits. Marginal Gaussian kernel densities use Scott bandwidths and are separately peak-scaled for display. The mean paired differences (GSE minus raw S2) are +0.0444 and +0.0047. Splits reuse tiles, so no inferential confidence band is shown. (c) Train-only PCA dimension sensitivity for five prespecified representations: mean test macro-F1 and one SD across seeds 0-4. Standardization and PCA are fitted on the 339 training tiles; a fixed C = 1 logistic classifier is fitted on the 453 training and validation tiles and tested on 114 tiles. Only feasible dimensions are shown (115 recorded seed-level rows); the

five-feature index control has no eligible point. (d) Label-purity sensitivity: macro-F1 for GSE and raw S2 at minimum dominant-class fractions of 0.5-0.8, with one stratified 75/25 split per threshold (seed 123; fixed C = 1 classifier). Stacked bars show retained tiles by source class (built-up, vegetation, water, and cropland); totals are 511, 398, 293, and 204, with 3, 2, 2, and 0 cropland tiles, respectively. Macro-F1 averages observed test classes; a value of 1.0 does not establish perfect generalization as class support shrinks. Small horizontal offsets in (c, d) separate overlapping marks; nominal dimensions and thresholds are given by the ticks. Neither quarantined adapter enters (c) or (d). All results are local split diagnostics, not evidence of equivalence, architecture effects under matched information, or independent-region transfer.

The Wuhan row-block holdout trains on rows 10-22, validates on rows 23-25 and tests on rows 26-30 (351/80/131 tiles). Cropland lacks training support and is excluded. Three-class macro-F1 is 0.9711 for raw observations and 0.9615 for GSE; Figure S11c includes 20 cached systems and the two controls. SatCLIP reaches 0.2885, compared with a repeated random-split mean of 0.4559 ± 0.0313. Because the class sets and retained cases differ, this contrast cannot isolate an effect of spatial separation. It does show that the location-only representation performs poorly in this specific local holdout.

Of six prespecified systems, five supply 115 PCA sensitivity rows at dimensions 8–256; the spectral-index vector has fewer than eight features (Figure 19c). In five splits, standardization/PCA fit 339 training tiles; fixed $C = 1$ logistic regression fits 453 combined training/validation representations and tests on 114 tiles. This differs from validation-selected repeated classification and establishes no universal optimal dimension.

Label-purity thresholds 0.5/0.6/0.7/0.8 retain 511/398/293/204 tiles, with cropland counts three/two/two/zero (Figure 19d). Each subset has a separate stratified 75/25 split (seed 123), train-fitted standardization and fixed $C = 1$; tests contain 128/100/74/51 tiles. Macro-F1 averages observed truth/prediction labels: values of 1.0 condition on changing class support, not perfect generalization or an independent label audit.

Of 190 geometry pairs, including 19 added with SatCLIP, 37 touching suspect adapters remain quarantined; Supplementary Figure S6 shows the other 153 pairs among 18 systems, with CKA and neighbour overlap in separate triangles; Figure 17 gives the global counterpart. GSE–TESSERA has linear CKA 0.9273 but 10-nearest-neighbour Jaccard 0.2363; similarity does not establish task causality. The two geometry summaries describe different aspects of these feature spaces: centred linear similarity of the feature matrices and overlap of local cosine neighbourhoods. Their disagreement is retained rather than compressed into a single quality score. Neither summary measures downstream accuracy or transfer to another region.

The retained Wuhan diagnostics characterize local readout and split sensitivity under their historical extraction contracts. They do not provide independent-label validation, cross-biome replication or a product lifecycle cost comparison. Their scope remains separate from the controlled global evaluation in Sections 5.3–5.6.

6. Challenges and Outlooks

The controlled comparisons identify where pretrained representations add value beyond strong observation-based and geographic controls. Positive CCI biomass and land-cover contrasts coexist with losses for GEDI AGBD and several fraction targets. These patterns rule out a single general-purpose ranking: the relevant unit of evidence is the input subgroup, reference, geographic split and readout. The nonlinear TerraFM AGBD counterexample further shows why a linear-probe failure should not be equated with an absence of predictive information. Conversely, Galileo's LOCO CCI result demonstrates that higher embedding accuracy can coincide with a negative delta when the baseline benefits more from the same readout.

Figure 9b condenses these contrasts into a decision sequence. Across the 300 image-encoder cells of Part I (spatial CV, linear readout, all training labels, 640 m), 176 intervals lay wholly above the matched baseline, 70 included zero and 54 lay below it. Gains concentrated

in land-cover classes (28 of 45 cells), class fractions (110 of 180) and CCI biomass (14 of 15), whereas sparse GEDI AGBD gave losses in 14 of 15 cells and the coordinate-only SatCLIP had wholly negative intervals against the strongest of all six baselines in 25 of 40 cohort–target cells. Counts also varied with readout, label budget and geographic protocol: with LightGBM, losses outnumbered gains (149 versus 52), and budgets of 16–256 labels gave 814 losses and 472 gains, whereas gains declined only from 185 under random CV to 161 under leave-one-continent-out CV. These summaries identify settings with more positive contrasts in this design; they do not test the relative causal importance of readout, label budget or geography. The 16–256-label tally pools five budgets and is not directly comparable in size with a single all-label tally. These counts characterize the global design; the historical Wuhan case does not independently validate them.

6.1 Information and support

A common grid does not equalize native footprints, output strides, pooling or dimensions, as the ViT, SatMAE and Scale-MAE designs illustrate (Cong et al., 2022; Dosovitskiy et al., 2021; Reed et al., 2023). Compression and reduced-model analyses add further differences (Gomes et al., 2025; Hackel et al., 2026). Pooling may erase boundaries and minority classes; dense readout may preserve them at greater cost. These mechanisms remain unisolated here.

Dimension and interpretability analyses show how much of this budget is accessible. Individual AlphaEarth dimensions relate to specific land-surface properties, and the full 64-dimensional space reconstructs 12 of 26 environmental variables with R^2 above 0.90 (Rahman, 2026). Geographic implicit neural representations with 256–512 ambient dimensions have intrinsic dimensions of roughly 2–10 that change with pretraining resolution and input modality (Rao, Rußwurm, et al., 2026), and concept decompositions are being used to audit what location embeddings encode (Betti et al., 2026). For canopy biochemistry,

retrieval accuracy saturated at 17–33 embedding channels or 5–14 principal components (Alam & Milas, 2025), and spatial scale effects have been examined for embedding-based wildfire-exposure prediction (Berg & Leyk, 2026). These analyses describe information content; they do not show that a frozen linear readout can exploit it.

The global comparisons establish target- and readout-specific gains, not a common advantage across encoders. Annual GEDI AGBD losses under native linear probing coexist with the positive TerraFM LightGBM contrast. A linear-probe failure therefore does not establish that a representation lacks predictive information. Differences between systems remain differences between complete checkpoint and preprocessing contracts, rather than isolated effects of architecture or pretraining. The location-encoder extension marks a further boundary: SatCLIP exceeded raw coordinate features for most targets, but had wholly negative intervals against the strongest of all six baselines in 18 of 20 annual spatial contrasts. Its six wholly positive monthly-cohort intervals show task-specific utility of the learned location prior; they do not make it a substitute for contemporaneous observations.

In Wuhan, paired GSE–raw differences were $+0.0444$ macro-F1 (95% interval $[-0.0092, 0.0969]$) and $+0.0047$ four-target mean Spearman ($[-0.0016, 0.0104]$). Neither was significant after multiplicity correction; this is not equivalence, and the classification interval permits a relevant gain. Optical summaries may already expose much local map-label signal; missing-data tolerance, invariance and geographic transfer require separate tests.

The paired footprint experiments hold locations and evaluation partitions fixed across 160–1,280 m supports. They change both image context and aggregated reference support, so their curves do not isolate either mechanism. The Wuhan 500 m design is a separate local setting and is not another level of this controlled global support analysis.

6.2 Temporal context

Pretraining and inference inputs differ across temporal and multimodal designs (Astruc et al., 2025; Dumeur et al., 2025; Jakubik et al., 2023; Mañas et al., 2021; Qin et al., 2025; Szwarcman et al., 2026; Tseng et al., 2025; Wang et al., 2023; Wang, Xiong, et al., 2025). Cross-modal objectives may suppress event-specific signals, and sequence-trained models can change semantics under single-date queries. Additional information does not necessarily improve representation efficiency.

Annual and monthly inputs use different retained populations and information budgets. Their within-subgroup deltas therefore cannot identify a causal benefit of temporal context. The twelve within-month composites characterize one year; cross-year and event transfer remain untested. The 2020 canopy-height reference is a lagged, model-derived target for 2021 imagery.

Application studies outside this benchmark point in the same direction. In Alpine tree-species mapping, the embedding advantage required a nonlinear classifier: a linear classifier on the embeddings underperformed a neural network on conventional composites, and transfer across years reduced weighted F1 by 9% for TESSERA and 14% for AlphaEarth (Ball et al., 2026). For burned-area mapping, neither embedding matched a pre- and post-fire Sentinel-2 spectral baseline (mean F1 0.860 for TESSERA with a support vector machine versus 0.895), and both declined when features came from the year after the fire (Silva & Gonçalves, 2026). Proxy features distilled from Sentinel-1/2 can retain part of the cross-year advantage when an embedding year is unavailable (Jing et al., 2026). Event timing, not the existence of an annual layer, determines whether an embedding can replace a dated observation.

Forecasting makes temporal requirements explicit in ocean prediction (Zheng et al., 2020), satellite assimilation (X. Xu et al., 2025) and radar nowcasting (Ravuri et al., 2021), as

well as Pangu-Weather (K. Bi et al., 2023), GraphCast (Lam et al., 2023), GenCast (Price et al., 2025) and Aurora (Bodnar et al., 2025). Their time-dependent inputs and forecast horizons define a different problem from decoding a static embedding.

EarthPT predicts future reflectance and vegetation indices (Smith et al., 2023), while COSMO aligns meteorological imagery and language (Kim & Park, 2026). These examples require temporal or semantic tests that are absent from our benchmark. They identify future evaluation needs, not capabilities established by annual feature fields.

Following the physical-process perspectives of Reichstein et al. (2019) and Irrgang et al. (2021), extending reusable features to prediction of evolving systems requires out-of-period validation, calibrated uncertainty and relevant physical constraints. The present experiments remain limited to the recorded surface targets and local spatial diagnostics.

6.3 Labels and independence

RemoteCLIP uses image–text contrast, while SatMAE and ScaleMAE employ masked reconstruction in the evaluated RGB families (Cong et al., 2022; Liu et al., 2024; Reed et al., 2023). Grouping shared benchmark observations prevents those observations from crossing evaluation folds, but does not establish absence from checkpoint pretraining. Missing training coordinates and dates leave indirect model–target dependence unresolved. The released checkpoint and input identities support traceability without certifying pretraining independence.

WorldCover, Esri and ETH canopy height use Sentinel-2 information; ETH and CCI also draw on GEDI-related sources (Esri, 2022; Lang et al., 2023; Santoro & Cartus, 2024; Zanaga et al., 2022). ETH is a model-derived 2020 canopy-height reference with land-cover-related missingness. GEDI AGBD is itself model-derived and sparsely sampled. Its retained observations do not form a complete areal inventory of each 640 m square. Differences between CCI and GEDI performance can reflect support, sampling and reference construction;

this benchmark does not identify their separate causal contributions. JRC 2021 seasonality describes temporal water persistence, rather than spatial water fraction.

Product agreement selects a different population and does not independently validate the labels. The paired WorldCover–Esri comparisons and agreement-conditioned target quantify reference dependence while retaining each target's actual coverage. Historical Wuhan purity filtering likewise changes class support: its dominant-class-fraction threshold reduced 511 tiles to 204 and removed cropland at 0.8. Neither procedure establishes field accuracy.

Label construction constrains application studies in the same way. Displaced survey coordinates required a probabilistic label loss for wealth prediction (Pettersson & Daoud, 2026); correcting field-plot locations with a canopy-height model reduced geolocation bias in biomass mapping (Sohrabi, 2026); and peatland embeddings reproduced in situ water-table observations but not expert-generated synthetic labels (Koch et al., 2026). Independent field or survey labels, recorded at the support of the embedding, remain the decisive control.

6.4 Geographic transfer

Adjacent Wuhan tiles share conditions, so random splits estimate local interpolation. The row-block control strengthens within-window validation but retains only three classes after excluding cropland absent from training; high scores cannot establish cross-climate/ biome robustness.

Dependence-aware holdouts test prediction away from calibration observations (Roberts et al., 2017); biomass results can collapse beyond spatial dependence ranges (Ploton et al., 2020). Transfer differs from population map accuracy: neither random nor blocked validation of convenience samples guarantees design-unbiased map accuracy, which requires probability sampling and design-based inference (Wadoux et al., 2021). Our tests address transfer within declared distances and frames.

Benchmarks and application studies report the same transfer gap. MMEarth-Bench finds that multimodal pretraining improves robustness with limited labels while geographic generalization remains poor (Gordon et al., 2026); PANGAEA notes that most earlier benchmarks are geographically concentrated in North America and Europe (Marsocci et al., 2026); a five-continent crop-type study examines whether models pretrained in data-rich regions transfer to data-scarce ones (Chang et al., 2025); and CNN classification accuracy declines with geographic distance (Fei et al., 2021). An agricultural benchmark of AlphaEarth reported performance comparable to local models but limited transferability (Ma et al., 2026), and stratified selection of scarce labels improved cross-region generalization over random sampling (Jungbluth et al., 2026). Geographic holdouts and the regions represented in pretraining therefore belong in every comparative claim, consistent with the argument that satellite data require their own machine-learning practice (Rolf et al., 2024).

The 90% monthly input threshold admitted a larger and compositionally different cohort than the nested 95% sensitivity. Rare classes, target-specific missingness and non-area-proportional sampling limit extrapolation beyond the recorded cohorts. Source-group separation prevents benchmark observations from crossing evaluation folds but does not establish absence from checkpoint pretraining. Paired bootstrap intervals condition on fitted readouts and retained reference values; they neither propagate all source-product uncertainty nor provide familywise inference across systems and targets. These boundaries qualify the generalization of the findings while preserving the measured gains and failures within each controlled setting.

6.5 Deployment

Products offer queries; checkpoints offer local observation/temporal control, with different storage, licensing and maintenance obligations (Brown et al., 2025; Fang et al., 2026; Feng, Atzberger, et al., 2026; Gomes et al., 2025; Gorelick et al., 2017; Klemmer et al., 2026;

Ye et al., 2026). Providers absorb some product computation and version risk; local users bear extraction costs. Encoder updates can invalidate predictors without changing dimension.

Storage and transfer costs motivate compressed and queryable representations. Neural embedding compression reported similar accuracy with 75–90% less data than compressing raw imagery (Gomes & Brunschwiler, 2024); the ESD database distributes quantized 30 m embeddings for 2000–2024 (Chen et al., 2026); an embedding-only uplink study evaluated onboard retrieval with under 1 kB of telemetry per query on an edge-computing surrogate (Sim, 2026); and approximate nearest-neighbour search trades accuracy against memory through product quantization (Jégou et al., 2010). Operational adoption further depends on application requirements and resource constraints that standard evaluation tasks rarely capture (Butsko et al., 2025).

Figure 17 relates predictive gains to warm batch-one encoder latency and native float32 vector storage; the associated cost records also retain process-allocated peak VRAM in the shared RTX 4090 environment. The within-subgroup Pareto fronts are descriptive point estimates. Acquisition, payload loading and downstream fitting are outside the timing boundary, and concurrent host activity was not isolated. These observations do not establish end-to-end throughput or product–encoder lifecycle savings. Versioned preprocessing, numeric encoding, checksums and update policies remain necessary for deployment compatibility.

The completed global comparisons cover the admitted input subgroups and evaluation settings. Independent-label validity, future-year transfer, independently labelled local validation and lifecycle cost remain separate questions. The literature synthesis has additional limits from capped retrieval and purposive selection. Mixed, negative and unavailable results therefore remain part of the evidence used to interpret representation utility.

6.6 Review limitations

The reference inventory accompanying this revision contains 400 unique records in the Zotero AI/Embedding collection, with metadata frozen on 7 October 2026. It combines the existing source library with a purposive supplement of 40 publications from *Nature*, *Science* and their associated journals. DOI and normalized-title matching resolve duplicate records. The inventory includes journal and conference articles, preprints, datasets and supporting technical resources; it is broader than the claim-level bibliography and the screened evidence described in the review protocol. Journal affiliation was used to broaden the application context, not as a substitute for methodological appraisal.

Figures 3 and 5 provide complementary views of the literature: title-term frequencies, release relationships and cumulative growth in a merged bibliographic corpus, and keyword co-occurrence and co-authorship within the 400-record collection. The collection export contains 400 titles, 399 dated records and 183 abstracts. Counts include preprints and supporting resources; 2026 is partial through 7 October. Zotero record dates are not necessarily first-release dates. Keyword matching uses abstracts only where they are available, so keyword frequencies partly reflect metadata coverage, and inventory tags are not treated as topical evidence. Source keys, term rules and plotting code make the descriptive panels reproducible.

These purposive distributions do not estimate field-wide prevalence or study quality. Selective citations and collection membership do not imply systematic inclusion or full-text eligibility assessment.

7. Conclusion

Satellite embeddings are reusable geospatial representations whose meaning depends on their observations, spatial and temporal support, output geometry and deployment contract. A

release-based hierarchy distinguishes image encoders, location encoders and precomputed embedding products; input, learning signal, temporal support, spatial support and geometry describe their technical properties. Adaptation and access are recorded separately. The 20-entry executable catalogue illustrates this framework without defining or statistically representing the literature.

The original image-encoder benchmark provides 29,352 audited system cells across 4,409 single-acquisition and 3,014 monthly-composite locations; the separate location-encoder extension adds 1,120 SatCLIP cells. Matched-input comparisons demonstrate substantial land-cover and vegetation-reference gains for selected frozen representations, but also identify negative and inconclusive contrasts, readout reversals and failures under geographic transfer. Accordingly, embedding selection should be based on absolute accuracy and the gain over the strongest relevant classical baseline at the intended support, label budget and transfer regime. The archived predictions, confidence intervals and figures make these distinctions reproducible, while unsupported same-input product and coarse-system comparisons remain explicitly unavailable. The location encoder SatCLIP exceeded raw coordinate features for most targets but had a wholly positive interval against the strongest of all six baselines in 6 of 40 cohort–target spatial contrasts, so location encoders supply regional context rather than current observations.

The complementary Wuhan case characterizes local readout and partition sensitivity under its historical extraction conditions. Its paired controls establish neither equivalence nor geographic generalization. A useful comparison must identify the target, input subgroup, geographic population, support, readout and uncertainty. Independent environmental validity, future-year transfer and lifecycle costs require evidence beyond prediction of reference products.

Supplementary material

The Supplementary Material provides the completed global protocol and its source-to-result records, explicitly separated from earlier pilot and engineering diagnostics. Table S1 preserves the historical 19-system implementation inventory. Figures S1-S5 document earlier review or diagnostic stages; Figure S6 shows local representation geometry, Figure S7 shows fixed-test fraction-regression scatter plots, and Figures S8-S11 provide the local prediction maps, recorded task scores and repeated-split diagnostics. Main Figures 12-17 report the principal global analyses, and Figures 18 and 19 summarize the local spatial context and paired controls. Additional readout, PCA, reference-target and input-quality results remain in the versioned benchmark package.

CRediT authorship contribution statement

Longhao Wang: Conceptualization, Methodology, Software, Validation, Formal analysis, Investigation, Data curation, Writing–original draft, Writing–review and editing, Visualization.

Declaration of competing interest

The author declares that there are no known competing financial interests or personal relationships that could have appeared to influence the work reported in this paper.

Funding

This research did not receive any specific grant from funding agencies in the public, commercial, or not-for-profit sectors.

Data availability

The study uses publicly available Earth-observation products and model artifacts. Source code is available at https://github.com/GISWLH/rs-embed. The original global evaluation archive contains 29,352 system cells and 326,202,930 prediction records; the location-encoder extension is recorded separately. The versioned archives retain cohort and target manifests, prediction records, plotting scripts and verification receipts. Reconstruction checks compared published scores with saved predictions and reference tables; they did not independently recompute every bootstrap interval. The Supplementary Material identifies the relevant archive paths and evidence records. The complete revision package is available from the author for reproducibility review; a persistent public archive identifier has not been assigned.

Acknowledgments

The author acknowledges the public remote sensing and Earth observation model communities whose released models, data products, and documentation made this review and benchmark possible.

Declaration of generative AI and AI-assisted technologies

OpenAI Codex and Anthropic Claude Code assisted manuscript organization and editing, software development, figure construction, citation integration and the literature-screening workflow. AI-assisted screening and adjudication are described in Section 2 and Supplementary Methods S2 and are not independent human dual screening. Quantitative figures were produced by reproducible code from the recorded data; no text-to-image system generated observations, predictions or quantitative results. Explanatory diagrams were constructed as editable Excalidraw or Adobe Illustrator artwork with AI-assisted coding. An archived APIYI gpt-image-2.5-vip concept served as a layout reference for Figure 2; its

generated pixels and traced paths are absent from the manuscript. Figure provenance records preserve source data, scripts and hashes. The author is responsible for checking the scientific interpretation, source support and final submitted content.

References

Ahn, D., Yang, J., Cha, M., Yang, H., Kim, J., Park, S., Han, S., Lee, E., Lee, S., & Park, S. (2023). A human-machine collaborative approach measures economic development using satellite imagery. *Nature Communications*, *14*(1), 6811. https://doi.org/10.1038/s41467-023-42122-8

Alam, M. M. T., & Milas, A. S. (2025). Dimensionality optimized machine learning retrieval of canopy chlorophyll, nitrogen, and phosphorus from google satellite embeddings. *Smart Agricultural Technology*. https://doi.org/10.1016/j.atech.2025.101601

Alvarez, C. I., Schneider, P., & Wurm, M. (2026). *Evaluating geospatial foundation-model embeddings for tropomi-based annual surface no2 estimation across europe* [Preprint]. ESS Open Archive. https://doi.org/10.22541/essoar.15005949/v1

Alvarez, C. I., Vaca, C. A. U., & Llumipanta, N. A. E. (2025). Machine learning for urban air quality prediction using google alphaearth foundations satellite embeddings: A case study of quito, ecuador. *Remote Sensing*. https://doi.org/10.3390/rs17203472

Astruc, G., Gonthier, N., Mallet, C., & Landrieu, L. (2025). AnySat: One earth observation model for many resolutions, scales, and modalities. *2025 IEEE/CVF Conference on Computer Vision and Pattern Recognition (CVPR)*, 19530–19540. https://doi.org/10.1109/CVPR52734.2025.01819

Augustyn, B., Kluczek, M., Bojanowski, J., & Czerkawski, M. (2026). *Similarity search of earth observation data using foundation model embeddings* [Preprint]. https://doi.org/10.5194/egusphere-egu26-14376

Ayush, K., Uzkent, B., Meng, C., Tanmay, K., Burke, M., Lobell, D., & Ermon, S. (2021). Geography-aware self-supervised learning. *2021 IEEE/CVF International Conference on Computer Vision (ICCV)*. https://doi.org/10.1109/iccv48922.2021.01002

Ball, J. G., Wicklein, J. A., Feng, Z., Knezevic, J., Jaffer, S., Madhavapeddy, A., Atzberger, C., Dalponte, M., & Coomes, D. A. (2026). Geospatial foundation models enable data-efficient tree species mapping in temperate mountain forests. *Science of Remote Sensing*. https://doi.org/10.1016/j.srs.2026.100466

Bastani, F., Wolters, P., Gupta, R., Ferdinando, J., & Kembhavi, A. (2023). Satlaspretrain: A large-scale dataset for remote sensing image understanding. *2023 IEEE/CVF International Conference on Computer Vision (ICCV)*. https://doi.org/10.1109/iccv51070.2023.01538

Bazi, Y., Bashmal, L., Al Rahhal, M. M., Al Dayil, R., & Al Ajlan, N. (2021). Vision transformers for remote sensing image classification. *Remote Sensing*, *13*(3), 516. https://doi.org/10.3390/rs13030516

Berg, A., & Leyk, S. (2026). *Spatial scale effects in foundation model earth embeddings: A case study on predicting the exposure of structures to wildfire in colorado, usa* [Preprint]. SSRN. https://doi.org/10.2139/ssrn.7026253

Betti, L., Ricke, S., Obadic, I., Stewart, A. J., & Rolf, E. (2026). *What's in an earth embedding? An explainability analysis of location encoders* [Preprint]. arXiv. https://arxiv.org/abs/2606.24997

Betz, F., Arisoy, B., Lauermann, M., Egger, G., Belletti, B., Bizzi, S., & Piégay, H. (2026). *Analyzing the potential of geospatial foundation models and earth embeddings for assessing dynamic riverine processes* [Preprint]. https://doi.org/10.5194/egusphere-egu26-14002

Bi, H., Feng, Y., Tong, B., Wang, M., Yu, H., Mao, Y., Chang, H., Diao, W., Wang, P., Yu, Y., Peng, H., Zhang, Y., Fu, K., & Sun, X. (2026). Ringmoe: Mixture-of-modality-experts multi-modal foundation models for universal remote sensing image interpretation. *IEEE Transactions on Pattern Analysis and Machine Intelligence*, *48*(4), 4388–4405. https://doi.org/10.1109/tpami.2025.3643453

Bi, K., Xie, L., Zhang, H., Chen, X., Gu, X., & Tian, Q. (2023). Accurate medium-range global weather forecasting with 3D neural networks. *Nature*, *619*(7970), 533–538. https://doi.org/10.1038/s41586-023-06185-3

Bodnar, C., Bruinsma, W. P., Lucic, A., Stanley, M., Allen, A., Brandstetter, J., Garvan, P., Riechert, M., Weyn, J. A., Dong, H., Gupta, J. K., Thambiratnam, K., Archibald, A. T., Wu, C.-C., Heider, E., Welling, M., Turner, R. E., & Perdikaris, P. (2025). A foundation model for the Earth system. *Nature*, *641*(8065), 1180–1187. https://doi.org/10.1038/s41586-025-09005-y

Bountos, N. I., Ouaknine, A., Papoutsis, I., & Rolnick, D. (2025). FoMo: Multi-modal, multi-scale and multi-task remote sensing foundation models for forest monitoring. *Proceedings of the AAAI Conference on Artificial Intelligence*, *39*, 27858–27868. https://doi.org/10.1609/aaai.v39i27.35002

Bourgoin, C., Ceccherini, G., Girardello, M., Vancutsem, C., Avitabile, V., Beck, P. S. A., Beuchle, R., Blanc, L., Duveiller, G., Migliavacca, M., Vieilledent, G., Cescatti, A., & Achard, F. (2024). Human degradation of tropical moist forests is greater than previously estimated. *Nature*, *631*(8021), 570–576. https://doi.org/10.1038/s41586-024-07629-0

Brandt, M., Tucker, C. J., Kariryaa, A., Rasmussen, K., Abel, C., Small, J., Chave, J., Rasmussen, L. V., Hiernaux, P., Diouf, A. A., Kergoat, L., Mertz, O., Igel, C., Gieseke, F., Schöning, J., Li, S., Melocik, K., Meyer, J., Sinno, S., … Fensholt, R. (2020). An

1893 unexpectedly large count of trees in the West African Sahara and Sahel. *Nature*, *587*(7832),
1894 78–82. https://doi.org/10.1038/s41586-020-2824-5
1895 Breiman, L. (2001). Random forests. *Machine Learning*, *45*(1), 5–32.
1896 https://doi.org/10.1023/A:1010933404324
1897 Brinkhoff, J., & McGavin, S. L. (2026). *Comparing AlphaEarth foundations*
1898 *embeddings and satellite time-series for rice crop event prediction* [Preprint]. SSRN.
1899 https://doi.org/10.2139/ssrn.7228924
1900 Brown, C. F., Brumby, S. P., Guzder-Williams, B., Birch, T., Hyde, S. B., Mazzariello,
1901 J., Czerwinski, W., Pasquarella, V. J., Haertel, R., Ilyushchenko, S., Schwehr, K., Weisse, M.,
1902 Stolle, F., Hanson, C., Guinan, O., Moore, R., & Tait, A. M. (2022). Dynamic World, Near
1903 real-time global 10 m land use land cover mapping. *Scientific Data*, *9*(1), 251.
1904 https://doi.org/10.1038/s41597-022-01307-4
1905 Brown, C. F., Kazmierski, M. R., Pasquarella, V. J., Rucklidge, W. J., Samsikova, M.,
1906 Zhang, C., Shelhamer, E., Lahera, E., Wiles, O., Ilyushchenko, S., Gorelick, N., Zhang, L. L.,
1907 Alj, S., Schechter, E., Askay, S., Guinan, O., Moore, R., Boukouvalas, A., & Kohli, P. (2025).
1908 *AlphaEarth Foundations: An embedding field model for accurate and efficient global*
1909 *mapping from sparse label data* (Version 1) [Preprint]. arXiv.
1910 https://doi.org/10.48550/ARXIV.2507.22291
1911 Burke, M., Driscoll, A., Lobell, D. B., & Ermon, S. (2021). Using satellite imagery to
1912 understand and promote sustainable development. *Science*, *371*(6535), eabe8628.
1913 https://doi.org/10.1126/science.abe8628
1914 Butsko, C., Tseng, G., Tricht, K. V., Milli, G., Rolnick, D., Cartuyvels, R., Becker-
1915 Reshef, I., Szantoi, Z., & Kerner, H. (2025). *Deploying geospatial foundation models in the*
1916 *real world: Lessons from worldcereal*. https://proceedings.mlr.press/v292/butsko25a.html

Cardoso, A. W., Hestir, E. L., Slingsby, J. A., Forbes, C. J., Moncrieff, G. R., Turner, W., Skowno, A. L., Nesslage, J., Brodrick, P. G., Gaddis, K. D., & Wilson, A. M. (2025). The biodiversity survey of the Cape (BioSCape), integrating remote sensing with biodiversity science. *Npj Biodiversity*, *4*(1), 2. https://doi.org/10.1038/s44185-024-00071-5

Castelluccio, M., Poggi, G., Sansone, C., & Verdoliva, L. (2015). *Land use classification in remote sensing images by convolutional neural networks* [Preprint]. arXiv. https://arxiv.org/abs/1508.00092

Cava, J. E., Navarro, J. A., Morán, J. L. T., & González, I. G. (2026). Aplicaciones de google satellite embeddings en la cartografía de plantaciones forestales en uganda. *Congresos UEX Actas de Congresos*. https://doi.org/10.17398/3101-7177.2.201

Cepeda, V. V., Nayak, G. K., & Shah, M. (2023). Geoclip: Clip-inspired alignment between locations and images for effective worldwide geolocalization. *Advances in Neural Information Processing Systems 36*. https://doi.org/10.52202/075280-0379

Cerna, S., Si-Moussi, S., Calderón-Sanou, I., Miele, V., & Thuiller, W. (2026). Limits and promises of earth observation foundation models in predicting multi-trophic soil biodiversity. In *Advances in ecological research/Advances in Ecological Research*. Advances in ecological research/Advances in Ecological Research. https://doi.org/10.1016/bs.aecr.2026.02.005

Cha, K., Seo, J., & Lee, T. (2026). A billion-scale foundation model for remote sensing images. *IEEE Journal of Selected Topics in Applied Earth Observations and Remote Sensing*, *19*, 16363–16378. https://doi.org/10.1109/JSTARS.2024.3401772

Chang, Y.-C., Stewart, A. J., Bastani, F., Wolters, P., Kannan, S., Huber, G. R., Wang, J., & Banerjee, A. (2025). On the generalizability of foundation models for crop type mapping. *IGARSS 2025 - 2025 IEEE International Geoscience and Remote Sensing Symposium*. https://doi.org/10.1109/igarss55030.2025.11242260

Chen, S., Wang, J., Yuan, S., Li, J., Xia, Y., Liao, Y., Wei, J., Yuan, J., Xu, X., Zhu, X., Zhu, P., Zhang, H., Zhou, Y., Fu, H., Huang, H., Chen, B., Dai, F., & Gong, P. (2026). Democratizing planetaryscale analysis: An ultra-lightweight earth embedding database for accurate and flexible global land monitoring. *Earth System Science Data*. https://doi.org/10.5194/essd-18-5375-2026

Cheng, C., You, N., Zhao, P., & Dong, J. (2026). Limited local classification performance but promising spatial transferability of AlphaEarth Foundations for crop mapping across thermal gradients. *Remote Sensing of Environment*, *347*, 115694. https://doi.org/10.1016/j.rse.2026.115694

Cheng, Y., Zhu, Q., & Fan, L. (2026). *From landslide conditioning factors to satellite embeddings: Evaluating the utilisation of google alphaearth for landslide susceptibility mapping using deep learning* [Preprint]. arXiv. https://doi.org/10.48550/arxiv.2601.07268

Cher, D., Iqbal, H., Xing, E., Wei, B., & Jacobs, N. (2026). *Tessellating the earth: Learnable spherical voronoi partitions for location encoding* [Preprint]. arXiv. https://arxiv.org/abs/2606.27514

Choudhury, S., Suvarna, C., Tsogsuren, I., Kreidieh, A. R., Aharoni, E., Lu, C.-T., & Arora, N. (2026). S2vec: Self-supervised geospatial embeddings for the built environment. *ACM Transactions on Spatial Algorithms and Systems*. https://doi.org/10.1145/3787217

Chowdhury, A. I., Ahishali, M., Vastaranta, M., Uddin, M. J., & Junttila, S. (2026). *Satellite embeddings as complementary predictors of standing dead-tree volume fraction in boreal forests* [Preprint]. SSRN. https://doi.org/10.2139/ssrn.6922442

Cole, E., Horn, G. V., Lange, C., Shepard, A., Leary, P., Perona, P., Loarie, S., & Aodha, O. M. (2023). *Spatial implicit neural representations for global-scale species mapping*. https://proceedings.mlr.press/v202/cole23a.html

Cong, Y., Khanna, S., Meng, C., Liu, P., Rozi, E., He, Y., Burke, M., Lobell, D. B., & Ermon, S. (2022). SatMAE: Pre-training transformers for temporal and multi-spectral satellite imagery. *Advances in Neural Information Processing Systems*, *35*, 197–211. https://doi.org/10.52202/068431-0015

Corley, I., Robinson, C., Becker-Reshef, I., & Ferres, J. M. L. (2026). *From pixels to patches: Pooling strategies for earth embeddings*. https://openreview.net/forum?id=oPfOVLFIrU

Corley, I., Sharma, L., & Crasto, R. (2025). *Landsat-bench: Datasets and benchmarks for landsat foundation models* [Preprint]. arXiv. https://doi.org/10.48550/arxiv.2506.08780

Cover, T., & Hart, P. (1967). Nearest neighbor pattern classification. *IEEE Transactions on Information Theory*. https://doi.org/10.1109/tit.1967.1053964

Cox, D. R. (1958). The regression analysis of binary sequences. *Journal of the Royal Statistical Society Series B (Statistical Methodology)*. https://doi.org/10.1111/j.2517-6161.1958.tb00292.x

Cropp, A. (2026). *What can satellite embedding fields tell us about shallow coral-reef habitats? A decodability survey of AlphaEarth over the Great Barrier Reef* [Preprint]. EarthArXiv. https://doi.org/10.31223/x50v35

Cui, Y., Shi, K., & Liang, S. (2026). *Earth embedding products for geospatial analysis: Foundations, applications, and open challenges* [Preprint]. EarthArXiv. https://doi.org/10.31223/x5qn40

Czerkawski, M., Kluczek, M., & Bojanowski, J. S. (2024). *Global and dense embeddings of earth: Major tom floating in the latent space* [Preprint]. arXiv. https://doi.org/10.48550/arxiv.2412.05600

Dai, Q., Zhu, J., Lv, G., Kalin, L., Yao, Y., Zhang, J., & Han, D. (2023). Radar remote sensing reveals potential underestimation of rainfall erosivity at the global scale. *Science Advances*, *9*(32), eadg5551. https://doi.org/10.1126/sciadv.adg5551

Dalei, D. K., Shrivastava, S., & Panigrahi, N. (2025). Geographic places to semantic spaces: Analysis of geospatial embeddings. *ISPRS Annals of the Photogrammetry, Remote Sensing and Spatial Information Sciences*. https://doi.org/10.5194/isprs-annals-x-5-w2-2025-131-2025

Danish, M. S., Munir, M. A., Shah, S. R. A., Khan, M. H., Anwer, R. M., Laaksonen, J., Khan, F. S., & Khan, S. (2026). *Terrafm: A scalable foundation model for unified multisensor earth observation*. https://openreview.net/forum?id=cBxuzdUDNx

Daroya, R., Cole, E., Aodha, O. M., Horn, G. V., & Maji, S. (2025). Wildsat: Learning satellite image representations from wildlife observations. *2025 IEEE/CVF International Conference on Computer Vision (ICCV)*. https://doi.org/10.1109/iccv51701.2025.00580

de Conto, T., Armston, J., & Dubayah, R. (2024). Characterizing the structural complexity of the Earth's forests with spaceborne lidar. *Nature Communications*, *15*(1), 8116. https://doi.org/10.1038/s41467-024-52468-2

Dhakal, A., Sastry, S., Khanal, S., Ahmad, A., Xing, E., & Jacobs, N. (2025). Range: Retrieval augmented neural fields for multi-resolution geoembeddings. *2025 IEEE/CVF Conference on Computer Vision and Pattern Recognition (CVPR)*. https://doi.org/10.1109/cvpr52734.2025.02298

Díaz-Ireland, G., Gülçin, D., López-Sánchez, A., Peces, M. G., Prieto-Herráez, D., & Velázquez, J. (2026). *Comparative evaluation of alphaearth annual embeddings vs. Seasonal remote sensing layers with u-net segmentation for california crop and land-use mapping* [Preprint]. SSRN. https://doi.org/10.2139/ssrn.6667132

Dinerstein, E., Olson, D., Joshi, A., Vynne, C., Burgess, N. D., Wikramanayake, E., Hahn, N., Palminteri, S., Hedao, P., Noss, R., Hansen, M., Locke, H., Ellis, E. C., Jones, B., Barber, C. V., Hayes, R., Kormos, C., Martin, V., Crist, E., … Saleem, M. (2017). An ecoregion-based approach to protecting half the terrestrial realm. *BioScience*, *67*(6), 534–545. https://doi.org/10.1093/biosci/bix014

Do, M. K., Han, K., Lai, P., Phan, K. T., & Xiang, W. (2025). Robsense: A robust multi-modal foundation model for remote sensing with static, temporal, and incomplete data adaptability. *2025 IEEE/CVF Conference on Computer Vision and Pattern Recognition (CVPR)*, 7427–7436. https://doi.org/10.1109/cvpr52734.2025.00696

Doerksen, K., & Kerner, H. (2026). *Earthshift: A benchmark for measuring robustness to real-world distribution shifts in earth observation* [Preprint]. arXiv. https://arxiv.org/abs/2605.29330

Dollinger, J., Robert, D., Plekhanova, E., Drees, L., & Wegner, J. D. (2025). *Climplicit: Climatic implicit embeddings for global ecological tasks*. https://www.climatechange.ai/papers/iclr2025/44

Dosovitskiy, A., Beyer, L., Kolesnikov, A., Weissenborn, D., Zhai, X., Unterthiner, T., Dehghani, M., Minderer, M., Heigold, G., Gelly, S., Uszkoreit, J., & Houlsby, N. (2021). An image is worth 16x16 words: Transformers for image recognition at scale. *International Conference on Learning Representations (ICLR)*. https://openreview.net/forum?id=YicbFdNTTy

Drusch, M., Bello, U. D., Carlier, S., Colin, O., Fernandez, V., Gascon, F., Hoersch, B., Isola, C., Laberinti, P., Martimort, P., Meygret, A., Spoto, F., Sy, O., Marchese, F., & Bargellini, P. (2011). Sentinel-2: Esa's optical high-resolution mission for gmes operational services. *Remote Sensing of Environment*. https://doi.org/10.1016/j.rse.2011.11.026

Du, P., Cui, L., Lian, Y., Li, H., Fan, J., Zhou, X., & Chen, Y. (2026). Global inversion of terrestrial net ecosystem exchange: Integrating explicit multi-source predictors and high-dimensional remote-sensing embeddings. *Remote Sensing*. https://doi.org/10.3390/rs18091390

Dubayah, R., Blair, J. B., Goetz, S., Fatoyinbo, L., Hansen, M., Healey, S., Hofton, M., Hurtt, G., Kellner, J., Luthcke, S., Armston, J., Tang, H., Duncanson, L., Hancock, S., Jantz, P., Marselis, S., Patterson, P. L., Qi, W., & Silva, C. (2020). The global ecosystem dynamics investigation: High-resolution laser ranging of the earth's forests and topography. *Science of Remote Sensing*. https://doi.org/10.1016/j.srs.2020.100002

Dumeur, I., Valero, S., & Inglada, J. (2025). Paving the way toward foundation models for irregular and unaligned satellite image time series. *IEEE Transactions on Geoscience and Remote Sensing*. https://doi.org/10.1109/tgrs.2025.3589013

Engstrom, C. B., & Quarmby, L. M. (2023). Satellite mapping of red snow on North American glaciers. *Science Advances*, *9*(47), eadi3268. https://doi.org/10.1126/sciadv.adi3268

Esri. (2022). *Esri releases updated land-cover map with new sets of global data*. https://www.esri.com/about/newsroom/announcements/esri-releases-updated-land-cover-map-with-new-sets-of-global-data

Esri. (2026). *Global Location Encoder (Sentinel-2)*. Esri. https://www.arcgis.com/home/item.html?id=b0664ef297c04d4aaa44191cf21e07f3

Fang, H., Stewart, A. J., Corley, I., Zhu, X. X., & Azizpour, H. (2026). *Earth embeddings as products: Taxonomy, ecosystem, and standardized access* [Preprint]. arXiv. https://arxiv.org/abs/2601.13134

Fei, X., Wessels, K., Pfoser, D., Zufle, A., & Gkountouna, O. (2021). Influence of geographic distance on CNN generalization for satellite image classification. *2021 IEEE*

International Geoscience and Remote Sensing Symposium IGARSS. https://doi.org/10.1109/igarss47720.2021.9553363

Feng, Z., Atzberger, C., Jaffer, S., Knezevic, J., Sormunen, S., Young, R., Lisaius, M. C., Immitzer, M., Jackson, T., Ball, J., Coomes, D. A., Madhavapeddy, A., Blake, A., & Keshav, S. (2026). *TESSERA: Temporal embeddings of surface spectra for earth representation and analysis* [Preprint]. arXiv. https://arxiv.org/abs/2506.20380v7

Feng, Z., Jaffer, S., Shokar, I., Knezevic, J., Ball, J., Sousa, P., Elvers, M., Lisaius, M., Atzberger, C., Young, R., Naik, A., Robinson, N., Coomes, D., Madhavapeddy, A., & Keshav, S. (2026). *TESSERA v2: Scaling pixel-wise earth foundation models* [Preprint]. arXiv. https://doi.org/10.48550/arxiv.2607.03949

Fibaek, C., Camilleri, L., Luyts, A., Dionelis, N., & Saux, B. L. (2024). Phileo bench: Evaluating geo-spatial foundation models. *IGARSS 2024 - 2024 IEEE International Geoscience and Remote Sensing Symposium*, 2739–2744. https://doi.org/10.1109/igarss53475.2024.10642780

Francis, A., & Czerkawski, M. (2024). Major tom: Expandable datasets for earth observation. *IGARSS 2024 - 2024 IEEE International Geoscience and Remote Sensing Symposium*, 2935–2940. https://doi.org/10.1109/igarss53475.2024.10640760

Fuller, A., Millard, K., & Green, J. (2023). Croma: Remote sensing representations with contrastive radar-optical masked autoencoders. *Advances in Neural Information Processing Systems 36*, 5506–5538. https://doi.org/10.52202/075280-0241

Gao, X., Pasquarella, V., Laflower, D., & Thompson, J. R. (2025). *Mapping forest communities, including species composition, structure, and carbon, at 10-m resolution using geospatial embeddings* [Preprint]. SSRN. https://doi.org/10.2139/ssrn.5936862

Gbodjo, Y. J. E., & Ienco, D. (2026). *Assessing the generalization of geospatial embeddings for temporaltransfer in land cover classification* [Preprint]. SSRN. https://doi.org/10.2139/ssrn.6890917

Gomes, C., & Brunschwiler, T. (2024). Neural embedding compression for efficient multi-task earth observation modelling. *IGARSS 2024 - 2024 IEEE International Geoscience and Remote Sensing Symposium*. https://doi.org/10.1109/igarss53475.2024.10642535

Gomes, C., Wittmann, I., Robert, D., Jakubik, J., Reichelt, T., Maurogiovanni, S., Vinge, R., Hurst, J., Scheurer, E., Sedona, R., Brunschwiler, T., Kesselheim, S., Batic, M., Stier, P., Wegner, J. D., Cavallaro, G., Pebesma, E., Marszalek, M., Belenguer-Plomer, M. A., … Albrecht, C. M. (2025). Lossy neural compression for geospatial analytics: A review. *IEEE Geoscience and Remote Sensing Magazine*, *13*(3), 97–135. https://doi.org/10.1109/mgrs.2025.3546527

Gonzalez-Calabuig, M., Cohrs, K.-H., Nedungadi, V., Osika, Z., Cartuyvels, R., Knoblauch, S., Massant, J., Nath, S., Ebel, P., & Sitokonstantinou, V. (2026). *Shrug-fm: Reliability-aware foundation models for earth observation* [Preprint]. https://doi.org/10.5194/egusphere-egu26-9940

Gordon, L., Belongie, S., Igel, C., & Lang, N. (2026). *Mmearth-bench: Global model adaptation via multimodal test-time training* [Preprint]. arXiv. https://arxiv.org/abs/2602.06285

Gorelick, N., Hancher, M., Dixon, M., Ilyushchenko, S., Thau, D., & Moore, R. (2017). Google earth engine: Planetary-scale geospatial analysis for everyone. *Remote Sensing of Environment*, *202*, 18–27. https://doi.org/10.1016/j.rse.2017.06.031

Guo, X., Lao, J., Dang, B., Zhang, Y., Yu, L., Ru, L., Zhong, L., Huang, Z., Wu, K., Hu, D., He, H., Wang, J., Chen, J., Yang, M., Zhang, Y., & Li, Y. (2024). Skysense: A multi-modal remote sensing foundation model towards universal interpretation for earth

observation imagery. *2024 IEEE/CVF Conference on Computer Vision and Pattern Recognition (CVPR)*. https://doi.org/10.1109/cvpr52733.2024.02613

Hackel, L., Burgert, T., & Demir, B. (2026). *How much of a model do we need? Redundancy and slimmability in remote sensing foundation models* [Preprint]. arXiv. https://arxiv.org/abs/2601.22841

Hansen, M. C., Potapov, P. V., Moore, R., Hancher, M., Turubanova, S. A., Tyukavina, A., Thau, D., Stehman, S. V., Goetz, S. J., Loveland, T. R., Kommareddy, A., Egorov, A., Chini, L., Justice, C. O., & Townshend, J. R. G. (2013). High-Resolution Global Maps of 21st-Century Forest Cover Change. *Science*, *342*(6160), 850–853. https://doi.org/10.1126/science.1244693

Hao, X., Chen, W., Zou, X., & Liang, Y. (2025). Nature makes no leaps: Building continuous location embeddings with satellite imagery from the web. *Proceedings of the ACM on Web Conference 2025*. https://doi.org/10.1145/3696410.3714629

He, K., Chen, X., Xie, S., Li, Y., Dollár, P., & Girshick, R. (2022). Masked autoencoders are scalable vision learners. *2022 IEEE/CVF Conference on Computer Vision and Pattern Recognition (CVPR)*. https://doi.org/10.1109/cvpr52688.2022.01553

Herzog, H., Bastani, F., Zhang, Y., Tseng, G., Redmon, J., Sablon, H., Park, R., Morrison, J., Buraczynski, A., Farley, K., Hansen, J., Howe, A., Johnson, P. A., Otterlee, M., Schmitt, T., Pitelka, H., Daspit, S., Ratner, R., Wilhelm, C., … Beukema, P. (2026). *Olmoearth: Stable latent image modeling for multimodal earth observation* [Preprint]. arXiv. https://doi.org/10.48550/arxiv.2511.13655

Hoerl, A. E., & Kennard, R. W. (1970). Ridge regression: Biased estimation for nonorthogonal problems. *Technometrics*. https://doi.org/10.1080/00401706.1970.10488634

Hong, D., Li, C., Li, X., Camps-Valls, G., & Chanussot, J. (2026). Foundation models in remote sensing: Evolving from unimodality to multimodality. *IEEE Geoscience and Remote Sensing Magazine*, *14*(2), 10–35. https://doi.org/10.1109/mgrs.2026.3669086

Hong, D., Zhang, B., Li, X., Li, Y., Li, C., Yao, J., Yokoya, N., Li, H., Ghamisi, P., Jia, X., Plaza, A., Gamba, P., Benediktsson, J. A., & Chanussot, J. (2024). Spectralgpt: Spectral remote sensing foundation model. *IEEE Transactions on Pattern Analysis and Machine Intelligence*, *46*(8), 5227–5244. https://doi.org/10.1109/tpami.2024.3362475

Hou, S., Liu, Z., Jiao, H., Xie, L., Qing, Y., Zhang, X., Xu, Q., Xu, Z., Guan, X., & Wu, H. (2026). *Aef-econ: Toward plug-and-play socioeconomic foundation embeddings from alphaearth for urban remote sensing* [Preprint]. EarthArXiv. https://doi.org/10.31223/x51f6g

Huang, Z., Yan, H., Zhan, Q., Yang, S., Zhang, M., Zhang, C., Lei, Y., Liu, Z., Liu, Q., & Wang, Y. (2025). *A survey on remote sensing foundation models: From vision to multimodality* [Preprint]. arXiv. https://doi.org/10.48550/arXiv.2503.22081

Huo, C., Chen, K., Zhang, S., Wang, Z., Yan, H., Shen, J., Hong, Y., Qi, G., Fang, H., & Wang, Z. (2025). When remote sensing meets foundation model: A survey and beyond. *Remote Sensing*, *17*(2), 179. https://doi.org/10.3390/rs17020179

Irrgang, C., Boers, N., Sonnewald, M., Barnes, E. A., Kadow, C., Staneva, J., & Saynisch-Wagner, J. (2021). Towards neural Earth system modelling by integrating artificial intelligence in Earth system science. *Nature Machine Intelligence*, *3*(8), 667–674. https://doi.org/10.1038/s42256-021-00374-3

Irvin, J., Tao, L., Zhou, J., Ma, Y., Nashold, L., Liu, B., & Ng, A. Y. (2023). *Usat: A unified self-supervised encoder for multi-sensor satellite imagery* [Preprint]. arXiv. https://doi.org/10.48550/arxiv.2312.02199

Jakubik, J., Roy, S., Phillips, C. E., Fraccaro, P., Godwin, D., Zadrozny, B., Szwarcman, D., Gomes, C., Nyirjesy, G., Edwards, B., Kimura, D., Simumba, N., Chu, L., Mukkavilli, S.

K., Lambhate, D., Das, K., Bangalore, R., Oliveira, D., Muszynski, M., … Ramachandran, R. (2023). *Foundation models for generalist geospatial artificial intelligence* [Preprint]. arXiv. https://arxiv.org/abs/2310.18660

Jakubik, J., Yang, F., Blumenstiel, B., Scheurer, E., Sedona, R., Maurogiovanni, S., Bosmans, J., Dionelis, N., Marsocci, V., Kopp, N., Ramachandran, R., Fraccaro, P., Brunschwiler, T., Cavallaro, G., Bernabe-Moreno, J., & Longépé, N. (2025). Terramind: Large-scale generative multimodality for earth observation. *2025 IEEE/CVF International Conference on Computer Vision (ICCV)*. https://doi.org/10.1109/iccv51701.2025.00693

Jean, N., Burke, M., Xie, M., Davis, W. M., Lobell, D. B., & Ermon, S. (2016). Combining satellite imagery and machine learning to predict poverty. *Science*, *353*(6301), 790–794. https://doi.org/10.1126/science.aaf7894

Jean, N., Wang, S., Samar, A., Azzari, G., Lobell, D., & Ermon, S. (2019). Tile2vec: Unsupervised representation learning for spatially distributed data. *Proceedings of the AAAI Conference on Artificial Intelligence*, *33*(01), 3967–3974. https://doi.org/10.1609/aaai.v33i01.33013967

Jégou, H., Douze, M., & Schmid, C. (2010). Product quantization for nearest neighbor search. *IEEE Transactions on Pattern Analysis and Machine Intelligence*. https://doi.org/10.1109/tpami.2010.57

Jia, Y., Marsocci, V., Gong, Z., Yang, X., Vergauwen, M., & Nascetti, A. (2025). Can generative geospatial diffusion models excel as discriminative geospatial foundation models? *Proceedings of the IEEE/CVF International Conference on Computer Vision (ICCV)*, 8429–8440. https://doi.org/10.1109/ICCV51701.2025.00789

Jiang, J., Zhao, W., Yan, C., Qiu, G. Y., Yan, W., Li, K., Mo, D., Zhu, B., & Xiong, Y. (2026). *Transformer-based mapping of 10 m spatiotemporally seamless daily urban*

evapotranspiration using geospatial foundation embeddings [Preprint]. SSRN. https://doi.org/10.2139/ssrn.6539464

Jin, C., Jiang, X., Wen, L., Wu, C., Xu, X., & Jiao, J. (2026). Assessing the utility of satellite embedding features for biomass prediction in subtropical forests with machine learning. *Remote Sensing*. https://doi.org/10.3390/rs18030436

Jing, K., Zhang, M., Wu, B., Xie, Y., Li, M., Ma, H., & Li, Y. (2026). Distilling geospatial foundation model semantics into interpretable sentinel-1/2 proxies for few-shot and cross-year crop type classification. *Big Earth Data*. https://doi.org/10.1080/20964471.2026.2691477

Johnson, D. (2026). *Calibrated spatial uncertainty for earth observation foundation models via matérn-motivated latent stochastic regularization* [Preprint]. EarthArXiv. https://doi.org/10.31223/x5rx9z

Joseph, M. B., De Souza Mendes, F., Nguyen, D. M. T., Sothe, C., & Anderson, C. B. (2026). *Continuous biome representations from earth observation embeddings* [Preprint]. arXiv. https://arxiv.org/abs/2606.11510v1

Jungbluth, A., Martínez-Ferrer, L., Allen, M., Gallego-Mejia, J. A., Dorr, F., Kalaitzis, F., & Ramos-Pollan, R. (2026). *Strategic data sampling for spatial generalization of earth observation foundation models* [Preprint]. ESS Open Archive. https://doi.org/10.22541/essoar.176840671.10772073/v1

Kennedy, E. V., Roelfsema, C. M., Lyons, M. B., Kovacs, E. M., Borrego-Acevedo, R., Roe, M., Phinn, S. R., Larsen, K., Murray, N. J., Yuwono, D., Wolff, J., & Tudman, P. (2021). Reef Cover, a coral reef classification for global habitat mapping from remote sensing. *Scientific Data*, *8*(1), 196. https://doi.org/10.1038/s41597-021-00958-z

Khajuria, V., Singh, S., Paro, L., Spagnolo, M., & Ribolini, A. (2026). Rock glacier detection using satellite embeddings and machine learning on google earth engine. *Earth Systems and Environment*. https://doi.org/10.1007/s41748-026-01139-x

Khan, H., & Ahmad, A. (2025). *Evaluating alphaearth foundation embeddings for pixel- and object-based land cover classification in google earth engine* [Preprint]. https://doi.org/10.20944/preprints202511.2172.v1

Khanna, S., Liu, P., Zhou, L., Meng, C., Rombach, R., Burke, M., Lobell, D., & Ermon, S. (2024). *DiffusionSat: A generative foundation model for satellite imagery*. https://openreview.net/forum?id=I5webNFDgQ

Kim, M.-H., & Park, H.-M. (2026). Cosmo: Contrastive satellite image embedding techniques reflecting expert weather bulletins. *IEEE Access*. https://doi.org/10.1109/access.2026.3702845

Klemmer, K., Rolf, E., Robinson, C., Mackey, L., & Rußwurm, M. (2025). Satclip: Global, general-purpose location embeddings with satellite imagery. *Proceedings of the AAAI Conference on Artificial Intelligence*, *39*, 4347–4355. https://doi.org/10.1609/aaai.v39i4.32457

Klemmer, K., Rolf, E., Rußwurm, M., Camps-Valls, G., Czerkawski, M., Ermon, S., Francis, A., Jacobs, N., Kerner, H., Mackey, L., Mai, G., Aodha, O. M., Reichstein, M., Robinson, C., Rolnick, D., Shelhamer, E., Sitzmann, V., Tuia, D., & Zhu, X. (2026). Earth embeddings: Toward artificial intelligence-centric representations of our planet. *IEEE Geoscience and Remote Sensing Magazine*, 2–15. https://doi.org/10.1109/mgrs.2026.3710416

Koch, J., Denager, T., Stisen, S., Greve, M. H., Møller, A. B., & Beucher, A. M. (2026). *Modelling carbon and groundwater in peatlands using alphaearth embeddings* [Preprint]. ESS Open Archive. https://doi.org/10.22541/essoar.177135853.32181864/v1

Kornblith, S., Norouzi, M., Lee, H., & Hinton, G. (2019). Similarity of neural network representations revisited. *Proceedings of the 36th International Conference on Machine Learning*, *97*, 3519–3529. https://doi.org/10.48550/arxiv.1905.00414

Kruitwagen, L., Story, K. T., Friedrich, J., Byers, L., Skillman, S., & Hepburn, C. (2021). A global inventory of photovoltaic solar energy generating units. *Nature*, *598*(7882), 604–610. https://doi.org/10.1038/s41586-021-03957-7

Kuckreja, K., Danish, M. S., Naseer, M., Das, A., Khan, S., & Khan, F. S. (2024). GeoChat:grounded large vision-language model for remote sensing. *2024 IEEE/CVF Conference on Computer Vision and Pattern Recognition (CVPR)*. https://doi.org/10.1109/cvpr52733.2024.02629

Lacoste, A., Lehmann, N., Rodriguez, P., Sherwin, E., Kerner, H., Lütjens, B., Irvin, J., Dao, D., Alemohammad, H., Drouin, A., Gunturkun, M., Huang, G., Vazquez, D., Newman, D., Bengio, Y., Ermon, S., & Zhu, X. (2023). Geo-bench: Toward foundation models for earth monitoring. *Advances in Neural Information Processing Systems 36*, 51080–51093. https://doi.org/10.52202/075280-2223

Lam, R., Sanchez-Gonzalez, A., Willson, M., Wirnsberger, P., Fortunato, M., Alet, F., Ravuri, S., Ewalds, T., Eaton-Rosen, Z., Hu, W., Merose, A., Hoyer, S., Holland, G., Vinyals, O., Stott, J., Pritzel, A., Mohamed, S., & Battaglia, P. (2023). Learning skillful medium-range global weather forecasting. *Science*, *382*(6677), 1416–1421. https://doi.org/10.1126/science.adi2336

Lane, K., & Karimzadeh, M. (2026). A genealogy of foundation models in remote sensing. *ACM Transactions on Spatial Algorithms and Systems*. https://doi.org/10.1145/3789505

Lang, N., Jetz, W., Schindler, K., & Wegner, J. D. (2023). A highresolution canopy height model of the earth. *Nature Ecology & Evolution*, *7*(11), 1778–1789. https://doi.org/10.1038/s41559-023-02206-6

Lauvaux, T., Giron, C., Mazzolini, M., d'Aspremont, A., Duren, R., Cusworth, D., Shindell, D., & Ciais, P. (2022). Global assessment of oil and gas methane ultra-emitters. *Science*, *375*(6580), 557–561. https://doi.org/10.1126/science.abj4351

Lee-Burkhart, K., Hatanaka, Y., Sadowski, P., & Chen, Q. (2026). *Geospatial foundation model embeddings improve land surface temperature recovery in the hawaiian islands* [Preprint]. SSRN. https://doi.org/10.2139/ssrn.6462445

Leonardi, J. A., Marsocci, V., Yordanov, V., & Brovelli, M. A. (2025). Integration of geospatial foundation models in unsupervised change detection workflows for landslide identification. *International Journal of Digital Earth*. https://doi.org/10.1080/17538947.2025.2547292

Li, W., Liang, S., Chen, K., Chen, Y., Ma, H., Xu, J., Ma, Y., Zhang, Y., Guan, S., Fang, H., & Shi, Z. (2026). *AgriFM: A multi-source temporal remote sensing foundation model for agriculture mapping*. https://www.sciencedirect.com/science/article/pii/S0034425726000040

Li, X., Li, C., Ghamisi, P., Hong, D., Benediktsson, J. A., & Chanussot, J. (2026). FlexiMo: A flexible remote sensing foundation model. *IEEE Transactions on Geoscience and Remote Sensing*, *64*, 1–16. https://doi.org/10.1109/TGRS.2026.3656362

Li, X., Tao, Y., Zhang, S., Liu, S., Xiong, Z., Luo, C., Liu, L., Pechenizkiy, M., Zhu, X. X., & Huang, T. (2025). REOBench: Benchmarking robustness of earth observation foundation models. *Advances in Neural Information Processing Systems*, *38*, 68313–68334. https://doi.org/10.52202/085713-2052

Li, X., & Yu, L. (2026). Mapping complex cropping patterns in china (2018–2021) at 10 m resolution: A data-driven framework based on multi-product integration and google

satellite embedding. *Earth System Science Data*, *18*, 5601–5626. https://doi.org/10.5194/essd-18-5601-2026

Lin, H., Lin, P., Zhang, F., Slater, L., Yang, Y., Pan, M., Qin, Q., & Hou, A. (2026). *Fusing satellite embeddings to improve streamflow reconstruction across river networks* [Preprint]. https://doi.org/10.5194/egusphere-2026-1834

Lisaius, M. C., Keshav, S., Blake, A., & Atzberger, C. (2026). *Embeddingbased crop type classification in the groundnut basin of senegal* [Preprint]. arXiv. https://arxiv.org/abs/2601.16900

Liu, F., Chen, D., Guan, Z., Zhou, X., Zhu, J., Ye, Q., Fu, L., & Zhou, J. (2024). RemoteCLIP: A vision language foundation model for remote sensing. *IEEE Transactions on Geoscience and Remote Sensing*, *62*, 1–16. https://doi.org/10.1109/TGRS.2024.3390838

Lu, S., Guo, J., Zimmer-Dauphinee, J. R., Nieusma, J. M., Wang, X., vanValkenburgh, P., Wernke, S. A., & Huo, Y. (2025). Vision foundation models in remote sensing: A survey. *IEEE Geoscience and Remote Sensing Magazine*, *13*(3), 190–215. https://doi.org/10.1109/MGRS.2025.3541952

Ma, Y., Shen, Y., Swatantran, A., & Lobell, D. B. (2026). Harvesting alphaearth: Benchmarking the geospatial foundation model for agricultural downstream tasks. *International Journal of Applied Earth Observation and Geoinformation*. https://doi.org/10.1016/j.jag.2026.105258

Mahato, T., Sarkar, S., Parida, B. R., & Bar, S. (2026). *Beyond multispectral limits: Satellite embeddings for fire severity estimation across global biomes* [Preprint]. https://doi.org/10.21203/rs.3.rs-9849270/v1

Mai, G., Huang, W., Sun, J., Song, S., Mishra, D., Liu, N., Gao, S., Liu, T., Cong, G., Hu, Y., Cundy, C., Li, Z., Zhu, R., & Lao, N. (2024). On the opportunities and challenges of

foundation models for geoai (vision paper). *ACM Transactions on Spatial Algorithms and Systems*. https://doi.org/10.1145/3653070

Mai, G., Janowicz, K., Yan, B., Zhu, R., Cai, L., & Lao, N. (2020). Multi-scale representation learning for spatial feature distributions using grid cells. *Bristol Research (University of Bristol)*. https://doi.org/10.48550/arxiv.2003.00824

Mai, G., Lao, N., He, Y., Song, J., & Ermon, S. (2023). *CSP: Self-supervised contrastive spatial pre-training for geospatial-visual representations*. https://proceedings.mlr.press/v202/mai23a.html

Mai, G., Xuan, Y., Zuo, W., He, Y., Song, J., Ermon, S., Janowicz, K., & Lao, N. (2023). Sphere2vec: A general-purpose location representation learning over a spherical surface for large-scale geospatial predictions. *ISPRS Journal of Photogrammetry and Remote Sensing*. https://doi.org/10.1016/j.isprsjprs.2023.06.016

Mall, U., Hariharan, B., & Bala, K. (2023). Change-aware sampling and contrastive learning for satellite images. *2023 IEEE/CVF Conference on Computer Vision and Pattern Recognition (CVPR)*. https://doi.org/10.1109/cvpr52729.2023.00509

Mañas, O., Lacoste, A., Giró-i-Nieto, X., Vazquez, D., & Rodríguez, P. (2021). Seasonal contrast: Unsupervised pre-training from uncurated remote sensing data. *Proceedings of the IEEE/CVF International Conference on Computer Vision (ICCV)*, 9414–9423. https://doi.org/10.1109/ICCV48922.2021.00928

Mantey, S., Attipoe, I. S. K., & Lawerteh, J. K. (2026). Boosting algorithm: An ensemble learning tool for land use land cover classification using google alpha earth foundations satellite embeddings. *Advances in Remote Sensing*. https://doi.org/10.4236/ars.2026.151001

Marsocci, V., Jia, Y., Bellier, G. L., Kerekes, D., Zeng, L., Hafner, S., Gerard, S., Brune, E., Yadav, R., Shibli, A., Fang, H., Ban, Y., Vergauwen, M., Audebert, N., & Nascetti, A.

(2026). Pangaea: Assessing geospatial foundation models capabilities through a global and inclusive benchmark. *IEEE Geoscience and Remote Sensing Magazine*, *14*(1), 245–285. https://doi.org/10.1109/mgrs.2025.3628194

McCallum, I., Kyba, C. C. M., Bayas, J. C. L., Moltchanova, E., Cooper, M., Cuaresma, J. C., Pachauri, S., See, L., Danylo, O., Moorthy, I., Lesiv, M., Baugh, K., Elvidge, C. D., Hofer, M., & Fritz, S. (2022). Estimating global economic well-being with unlit settlements. *Nature Communications*, *13*(1), 2459. https://doi.org/10.1038/s41467-022-30099-9

McFeeters, S. K. (1996). The use of the normalized difference water index (ndwi) in the delineation of open water features. *International Journal of Remote Sensing*, *17*(7), 1425–1432. https://doi.org/10.1080/01431169608948714

Michail, D., Saka, E., Giannopoulos, I., & Papoutsis, I. (2026). *Osmgraphclip: Learning global location representations from openstreetmap graphs* [Preprint]. arXiv. https://arxiv.org/abs/2606.08046

Misra, A., White, K., Nsutezo, S. F., Straka, W., & Lavista, J. (2025). Mapping global floods with 10 years of satellite radar data. *Nature Communications*, *16*(1), 5762. https://doi.org/10.1038/s41467-025-60973-1

Mura, M., Mura, M., Puletti, N., & Scotti, R. (2026). *Operational deployment of satellite embeddings for forestry: An evaluation* [Preprint]. SSRN. https://doi.org/10.2139/ssrn.6362220

Narimani, M., Pourreza, A., & Farajpoor, P. (2026). Mapping tomato cropping systems in california using alphaearth geospatial embeddings and deep learning analysis. *2026 Indianapolis, Indiana, July 12-15, 2026*. https://doi.org/10.13031/aim.202600545

Natural Earth. (n.d.). *1:10m cultural vectors: Admin 0 – countries, version 5.1.1* [Data set]. Retrieved https://www.naturalearthdata.com/downloads/10m-cultural-vectors/10m-admin-0-countries/

Nedungadi, V., Kariryaa, A., Oehmcke, S., Belongie, S., Igel, C., & Lang, N. (2025). Mmearth: Exploring multi-modal pretext tasks for geospatial representation learning. *Lecture Notes in Computer Science*. https://doi.org/10.1007/978-3-031-73039-9_10

Noman, M., Naseer, M., Cholakkal, H., Anwer, R. M., Khan, S., & Khan, F. S. (2024). Rethinking transformers pre-training for multi-spectral satellite imagery. *Proceedings of the IEEE/CVF Conference on Computer Vision and Pattern Recognition (CVPR)*, 27811–27819. https://doi.org/10.1109/cvpr52733.2024.02627

Ou, Z., & Zheng, Y. (2025). Foundation-scale satellite embeddings reframe hydrological generalization as a representation problem. *Geophysical Research Letters*. https://doi.org/10.1029/2025gl121604

Paluba, D., Marsocci, V., Onacillová, K., Quintana, Y. T. P., & Hastie, A. (2026). *Gem-forest: A global satellite embedding–based map of forests and tree crops for 2020* [Preprint]. https://doi.org/10.5194/egusphere-2026-1401-v1

Paolo, F. S., Kroodsma, D., Raynor, J., Hochberg, T., Davis, P., Cleary, J., Marsaglia, L., Orofino, S., Thomas, C., & Halpin, P. (2024). Satellite mapping reveals extensive industrial activity at sea. *Nature*, *625*(7993), 85–91. https://doi.org/10.1038/s41586-023-06825-8

Payne, M. (2021). Satellite remote sensing of deforestation for oil palm. *Nature Reviews Earth & Environment*, *2*(4), 230–230. https://doi.org/10.1038/s43017-021-00159-7

Pekel, J.-F., Cottam, A., Gorelick, N., & Belward, A. S. (2016). High-resolution mapping of global surface water and its long-term changes. *Nature*, *540*(7633), 418–422. https://doi.org/10.1038/nature20584

Pettersson, M. B., & Daoud, A. (2026). *Leveraging compact satellite embeddings and graph neural networks for large-scale poverty mapping* [Preprint]. arXiv. https://doi.org/10.48550/arxiv.2511.01408

Plas, T. L., Bakermans, J. J., Nedungadi, V., Tijūnaityte, G., Rußwurm, M., & Athanasiadis, I. N. (2026). *Better together: Evaluating the complementarity of earth embedding models* [Preprint]. arXiv. https://arxiv.org/abs/2605.18667

Ploton, P., Mortier, F., Réjou-Méchain, M., Barbier, N., Picard, N., Rossi, V., Dormann, C., Cornu, G., Viennois, G., Bayol, N., Lyapustin, A., Gourlet-Fleury, S., & Pélissier, R. (2020). Spatial validation reveals poor predictive performance of large-scale ecological mapping models. *Nature Communications*, *11*, 4540. https://doi.org/10.1038/s41467-020-18321-y

Price, I., Sanchez-Gonzalez, A., Alet, F., Andersson, T. R., El-Kadi, A., Masters, D., Ewalds, T., Stott, J., Mohamed, S., Battaglia, P., Lam, R., & Willson, M. (2025). Probabilistic weather forecasting with machine learning. *Nature*, *637*(8044), 84–90. https://doi.org/10.1038/s41586-024-08252-9

Puriy, N., Jakubik, J., Blumenstiel, B., & Schindler, K. (2026). *Terraflow: Multimodal, multitemporal representation learning for earth observation* [Preprint]. arXiv. https://doi.org/10.48550/arxiv.2603.12762

Qi, W., Yu, L., Liu, T., Wang, Y., Zhou, X., Zhang, Y., Li, X., Zhao, Q., Wu, H., Zheng, S., Zeng, Y., & Xu, M. (2026). Integrating hyperspectral data and google satellite embedding features for aquatic fish biodiversity prediction. *Journal of Remote Sensing*. https://doi.org/10.34133/remotesensing.1069

Qin, X., Wang, D., Zhang, J., Wang, F., Su, X., Du, B., & Zhang, L. (2025). *Timo: Spatiotemporal foundation model for satellite image time series* [Preprint]. arXiv. https://arxiv.org/abs/2505.08723

Radford, A., Kim, J. W., Hallacy, C., Ramesh, A., Goh, G., Agarwal, S., Sastry, G., Askell, A., Mishkin, P., Clark, J., Krueger, G., & Sutskever, I. (2021). *Learning transferable*

visual models from natural language supervision [Preprint]. arXiv. https://doi.org/10.48550/arxiv.2103.00020

Radman, A., Mahdianpari, M., Varon, D. J., & Mohammadimanesh, F. (2023). S2MetNet: A novel dataset and deep learning benchmark for methane point source quantification using sentinel-2 satellite imagery. *Remote Sensing of Environment*. https://doi.org/10.1016/j.rse.2023.113708

Rahman, M. (2026). Physically interpretable alphaearth foundation model embeddings enable llm-based land surface intelligence. *Remote Sensing Applications Society and Environment*. https://doi.org/10.1016/j.rsase.2026.102045

Ramachandran, N., Irvin, J., Omara, M., Gautam, R., Meisenhelder, K., Rostami, E., Sheng, H., Ng, A. Y., & Jackson, R. B. (2024). Deep learning for detecting and characterizing oil and gas well pads in satellite imagery. *Nature Communications*, *15*(1), 7036. https://doi.org/10.1038/s41467-024-50334-9

Ramachandran, R., Roy, S., Maskey, M., Szwarcman, D., & Fraccaro, P. (2025). *A primer for assessing foundation models for earth observation* [Preprint]. https://ntrs.nasa.gov/citations/20250005271

Rao, A., Crasto, R., Ooms, T., Rolnick, D., Klemmer, K., & Rußwurm, M. (2026). *Localized, high-resolution geographic representations with slepian functions*. https://icml.cc/virtual/2026/poster/62670

Rao, A., Rußwurm, M., Klemmer, K., & Rolf, E. (2026). *Measuring the intrinsic dimension of earth representations*. https://openreview.net/forum?id=gQPD83DrGp

Ravuri, S., Lenc, K., Willson, M., Kangin, D., Lam, R., Mirowski, P., Fitzsimons, M., Athanassiadou, M., Kashem, S., Madge, S., Prudden, R., Mandhane, A., Clark, A., Brock, A., Simonyan, K., Hadsell, R., Robinson, N., Clancy, E., Arribas, A., & Mohamed, S. (2021).

Skilful precipitation nowcasting using deep generative models of radar. *Nature*, *597*(7878), 672–677. https://doi.org/10.1038/s41586-021-03854-z

Reed, C. J., Gupta, R., Li, S., Brockman, S., Funk, C., Clipp, B., Keutzer, K., Candido, S., Uyttendaele, M., & Darrell, T. (2023). Scale-MAE: A scale-aware masked autoencoder for multiscale geospatial representation learning. *Proceedings of the IEEE/CVF International Conference on Computer Vision (ICCV)*, 4065–4076. https://doi.org/10.1109/ICCV51070.2023.00378

Reichstein, M., Camps-Valls, G., Stevens, B., Jung, M., Denzler, J., Carvalhais, N., & Prabhat. (2019). Deep learning and process understanding for data-driven Earth system science. *Nature*, *566*(7743), 195–204. https://doi.org/10.1038/s41586-019-0912-1

Roberts, D. R., Bahn, V., Ciuti, S., Boyce, M. S., Elith, J., Guillera-Arroita, G., Hauenstein, S., Lahoz-Monfort, J. J., Schröder, B., Thuiller, W., Warton, D. I., Wintle, B. A., Hartig, F., & Dormann, C. F. (2017). Cross-validation strategies for data with temporal, spatial, hierarchical, or phylogenetic structure. *Ecography*, *40*(8), 913–929. https://doi.org/10.1111/ecog.02881

Rolf, E., Klemmer, K., Robinson, C., & Kerner, H. (2024). *Position: Mission critical—Satellite data is a distinct modality in machine learning*. https://proceedings.mlr.press/v235/rolf24a.html

Rolf, E., Klemmer, K., & Rußwurm, M. (2025). Earth embeddings: Harnessing the information in earth observation data with machine learning. *Proceedings of the Special Interest Group on Computer Graphics and Interactive Techniques Conference Frontiers*. https://doi.org/10.1145/3736539.3754446

Rolf, E., Proctor, J., Carleton, T., Bolliger, I., Shankar, V., Ishihara, M., Recht, B., & Hsiang, S. (2021). A generalizable and accessible approach to machine learning with global

satellite imagery. *Nature Communications*, *12*(1), 4392. https://doi.org/10.1038/s41467-021-24638-z

Rußwurm, M., Wang, S., Kellenberger, B., Roscher, R., & Tuia, D. (2024). Meta-learning to address diverse Earth observation problems across resolutions. *Communications Earth & Environment*, *5*(1), 37. https://doi.org/10.1038/s43247-023-01146-0

Santoro, M., & Cartus, O. (2024). *ESA biomass climate change initiative (Biomass_cci): Global datasets of forest above-ground biomass for the years 2010, 2015, 2016, 2017, 2018, 2019, 2020 and 2021, v5.01* [Data set]. https://doi.org/10.5285/bf535053562141c6bb7ad831f5998d77

Schmitt, M., Hughes, L. H., Qiu, C., & Zhu, X. X. (2019). Sen12ms – a curated dataset of georeferenced multi-spectral sentinel-1/2 imagery for deep learning and data fusion. *ISPRS Annals of the Photogrammetry, Remote Sensing and Spatial Information Sciences*, *IV-2/W7*, 153–160. https://doi.org/10.5194/isprs-annals-iv-2-w7-153-2019

Sherman, L., Proctor, J., Druckenmiller, H., Tapia, H., & Hsiang, S. (2026). Global high-resolution estimates of the un human development index using satellite imagery and machine learning. *Nature Communications*, *17*(1), 1315. https://doi.org/10.1038/s41467-026-68805-6

Silva, L., & Gonçalves, J. (2026). *Evaluating alphaearth and tessera geospatial embeddings for machine learning-based burned area mapping in portugal*. Zenodo (CERN European Organization for Nuclear Research). https://doi.org/10.5281/zenodo.21252157

Sim, S. (2026). Embedding-only uplink for onboard retrieval under shift in remote sensing. *IEEE Geoscience and Remote Sensing Letters*. https://doi.org/10.1109/lgrs.2026.3718430

Simard, M., Fatoyinbo, L., Smetanka, C., Rivera-Monroy, V. H., Castañeda-Moya, E., Thomas, N., & Van der Stocken, T. (2019). Mangrove canopy height globally related to

precipitation, temperature and cyclone frequency. *Nature Geoscience*, *12*(1), 40–45. https://doi.org/10.1038/s41561-018-0279-1

Simumba, N., Lehmann, N., Fraccaro, P., Alemohammad, H., Mel, G. D., Khan, S., Maskey, M., Longepe, N., Zhu, X. X., Kerner, H., Bernabe-Moreno, J., & Lacoste, A. (2026). *Geo-bench-2: From performance to capability, rethinking evaluation in geospatial ai* [Preprint]. arXiv. https://arxiv.org/abs/2511.15658v2

Smith, M. J., Fleming, L., & Geach, J. (2023). *Earthpt: A foundation model for earth observation* [Preprint]. https://doi.org/10.5194/egusphere-egu24-1760

Sohrabi, H. (2026). Integrating satellite embeddings and national forest inventory data to map above-ground biomass of temperate deciduous old-growth forests. *Advances in Space Research*. https://doi.org/10.1016/j.asr.2026.04.018

Stewart, A. J., Fang, H., Corley, I. A., & Zhu, X. X. (2026). *Earth embeddings* [Preprint]. arXiv. https://arxiv.org/abs/2608.03410

Strelnikov, I., Ostapko, V., & Ibatulina, Y. (2025). Testing the applicability of foundational satellite data embedding models for remote identification of dominant species in herbaceous communities. *Zenodo (CERN European Organization for Nuclear Research)*. https://doi.org/10.5281/zenodo.17800714

Sumbul, G., Charfuelan, M., Demir, B., & Markl, V. (2019). Bigearthnet: A large-scale benchmark archive for remote sensing image understanding. *IGARSS 2019 - 2019 IEEE International Geoscience and Remote Sensing Symposium*. https://doi.org/10.1109/igarss.2019.8900532

Sun, Y., Xue, Z., Wu, H., & Nie, X. (2026). The first map of planted mangrove forests in china derived from time-series landsat and google satellite embeddings. *Remote Sensing of Environment*. https://doi.org/10.1016/j.rse.2026.115541

Szwarcman, D., Roy, S., Fraccaro, P., Gíslason, orsteinn E., Blumenstiel, B., Ghosal, R., Oliveira, P. H., Sousa Almeida, J. L., Sedona, R., Kang, Y., Chakraborty, S., Wang, S., Gomes, C., Kumar, A., Gaur, V., Truong, M., Godwin, D., Khallaghi, S., Lee, H., … Moreno, J. B. (2026). Prithvi-EO-2.0: A versatile multitemporal foundation model for earth observation applications. *IEEE Transactions on Geoscience and Remote Sensing*, *64*, 1–20. https://doi.org/10.1109/TGRS.2025.3642610

Tellman, B., Sullivan, J. A., Kuhn, C., Kettner, A. J., Doyle, C. S., Brakenridge, G. R., Erickson, T. A., & Slayback, D. A. (2021). Satellite imaging reveals increased proportion of population exposed to floods. *Nature*, *596*(7870), 80–86. https://doi.org/10.1038/s41586-021-03695-w

Thoreau, R., Marsocci, V., & Derksen, D. (2025). Parameter-efficient adaptation of geospatial foundation models through embedding deflection. *2025 IEEE/CVF International Conference on Computer Vision (ICCV)*. https://doi.org/10.1109/iccv51701.2025.00895

Tseng, G., Cartuyvels, R., Zvonkov, I., Purohit, M., Rolnick, D., & Kerner, H. R. (2023). *Lightweight, pre-trained transformers for remote sensing timeseries* [Preprint]. arXiv. https://doi.org/10.48550/arxiv.2304.14065

Tseng, G., Fuller, A., Reil, M., Herzog, H., Beukema, P., Bastani, F., Green, J. R., Shelhamer, E., Kerner, H., & Rolnick, D. (2025). Galileo: Learning global & local features of many remote sensing modalities. *Proceedings of the 42nd International Conference on Machine Learning*, *267*, 60280–60300. https://proceedings.mlr.press/v267/tseng25a.html

Tucker, C., Brandt, M., Hiernaux, P., Kariryaa, A., Rasmussen, K., Small, J., Igel, C., Reiner, F., Melocik, K., Meyer, J., Sinno, S., Romero, E., Glennie, E., Fitts, Y., Morin, A., Pinzon, J., McClain, D., Morin, P., Porter, C., … Fensholt, R. (2023). Sub-continental-scale carbon stocks of individual trees in African drylands. *Nature*, *615*(7950), 80–86. https://doi.org/10.1038/s41586-022-05653-6

Tucker, C. J. (1979). Red and photographic infrared linear combinations for monitoring vegetation. *Remote Sensing of Environment*, *8*(2), 127–150. https://doi.org/10.1016/0034-4257(79)90013-0

Tuia, D., Roscher, R., Wegner, J. D., Jacobs, N., Zhu, X., & CampsValls, G. (2020). Toward a collective agenda on ai for earth science data analysis. *IEEE Geoscience and Remote Sensing Magazine*. https://doi.org/10.1109/mgrs.2020.3043504

Vinge, R., Wittmann, I., Schneider, J., Marszalek, M., Gilch, L., Brunschwiler, T., & Albrecht, C. M. (2026). *Neuco-bench: A novel benchmark framework for neural embeddings in earth observation* [Preprint]. arXiv. https://doi.org/10.48550/arxiv.2510.17914

Wadoux, A. M. J.-C., Heuvelink, G. B. M., Bruin, S., & Brus, D. J. (2021). Spatial cross-validation is not the right way to evaluate map accuracy. *Ecological Modelling*, *457*, 109692. https://doi.org/10.1016/j.ecolmodel.2021.109692

Waldmann, L., Shah, A., Wang, Y., Lehmann, N., Stewart, A., Xiong, Z., Zhu, X. X., Bauer, S., & Chuang, J. (2025). Panopticon: Advancing any-sensor foundation models for earth observation. *2025 IEEE/CVF Conference on Computer Vision and Pattern Recognition Workshops (CVPRW)*, 2195–2205. https://doi.org/10.1109/cvprw67362.2025.00207

Walsh, J., Fawcett, W., Colvard, G., & Ramos-Pollán, R. (2026). *Zero-shot satellite image retrieval through joint embeddings: Application to crisis response*. Trillium Technologies. https://doi.org/10.56272/a2c9ee39

Wang, Y., Braham, N. A. A., Xiong, Z., Liu, C., Albrecht, C. M., & Zhu, X. X. (2023). Ssl4eo-s12: A large-scale multimodal, multitemporal dataset for self-supervised learning in earth observation [software and data sets]. *IEEE Geoscience and Remote Sensing Magazine*, *11*(3), 98–106. https://doi.org/10.1109/mgrs.2023.3281651

Wang, Y., Hernandez Hernandez, H., Albrecht, C. M., & Zhu, X. X. (2025). Feature guided masked autoencoder for self-supervised learning in remote sensing. *IEEE Journal of*

Selected Topics in Applied Earth Observations and Remote Sensing, *18*, 321–336. https://doi.org/10.1109/JSTARS.2024.3493237

Wang, Y., Xiong, Z., Liu, C., Stewart, A. J., Dujardin, T., Bountos, N. I., Zavras, A., Gerken, F., Papoutsis, I., Leal-Taixe, L., & Zhu, X. X. (2025). *Towards a unified copernicus foundation model for earth vision* [Preprint]. arXiv. https://arxiv.org/abs/2503.11849

Watt, M. S., Holdaway, A., Marchant, J. S., Mohan, M., Watt, P., & Baboolall, M. (2026). National-scale forest aboveground biomass mapping in guyana using stability-based feature selection and geospatial embeddings. *Forests*. https://doi.org/10.3390/f17060725

Wei, Y. (2026). *Uncertainty quantification for earth observation foundation models* [Preprint]. https://doi.org/10.5194/egusphere-egu26-20813

Weiss, M., Jacob, F., & Duveiller, G. (2020). Remote sensing for agricultural applications: A meta-review. *Remote Sensing of Environment*, *236*, 111402. https://doi.org/10.1016/j.rse.2019.111402

Wen, Y., Cai, J., Ma, Q., Li, L., Chen, X., Webster, C., & Zhou, Y. (2026). *MoRA: Mobility as the backbone for geospatial representation learning at scale*. https://openreview.net/forum?id=IlBr5JJsCj

Wu, K., Zhang, Y., Ru, L., Dang, B., Lao, J., Yu, L., Luo, J., Zhu, Z., Sun, Y., Zhang, J., Zhu, Q., Wang, J., Yang, M., Chen, J., Zhang, Y., & Li, Y. (2025). A semantic-enhanced multi-modal remote sensing foundation model for earth observation. *Nature Machine Intelligence*, *7*(8), 1235–1249. https://doi.org/10.1038/s42256-025-01078-8

Xiao, A., Xuan, W., Wang, J., Huang, J., Tao, D., Lu, S., & Yokoya, N. (2025). Foundation models for remote sensing and earth observation: A survey. *IEEE Geoscience and Remote Sensing Magazine*, *13*(4), 297–324. https://doi.org/10.1109/MGRS.2025.3576766

Xiong, Z., Wang, Y., Zhang, F., Stewart, A. J., Hanna, J., Borth, D., Papoutsis, I., Saux, B. L., Camps-Valls, G., & Zhu, X. X. (2024). *Neural plasticity-inspired multimodal foundation model for earth observation* [Preprint]. arXiv. https://arxiv.org/abs/2403.15356

Xu, X., Sun, X., Han, W., Zhong, X., Chen, L., Gao, Z., & Li, H. (2025). FuXi-DA: A generalized deep learning data assimilation framework for assimilating satellite observations. *Npj Climate and Atmospheric Science*, *8*(1), 156. https://doi.org/10.1038/s41612-025-01039-3

Xu, Y., Gao, S., Huang, Q., Göçmen, A., Zhu, Q., & Zhang, F. (2025). Predicting human mobility flows in cities using deep learning on satellite imagery. *Nature Communications*, *16*(1), 10372. https://doi.org/10.1038/s41467-025-65373-z

Xue, X., & Zhu, X. (2026). Regression in earth observation: Are vision–language models up to the challenge? *IEEE Geoscience and Remote Sensing Magazine*, *14*(1), 121–150. https://doi.org/10.1109/MGRS.2025.3596243

Yang, L., Chen, N., Yue, J., Liu, Y., Ma, J., Ghamisi, P., Plaza, A., & Fang, L. (2025). *Survey of multimodal geospatial foundation models: Techniques, applications, and challenges* [Preprint]. arXiv. https://arxiv.org/abs/2510.22964

Ye, D., Kiv, D., Hu, W., Shi, J., & Wang, S. (2026). *Any model, any place, any time: Get remote sensing foundation model embeddings on demand* [Preprint]. arXiv. https://arxiv.org/abs/2602.23678

Yeh, C., Perez, A., Driscoll, A., Azzari, G., Tang, Z., Lobell, D., Ermon, S., & Burke, M. (2020). Using publicly available satellite imagery and deep learning to understand economic well-being in Africa. *Nature Communications*, *11*(1), 2583. https://doi.org/10.1038/s41467-020-16185-w

Yuan, Y., & Lin, L. (2021). Self-supervised pretraining of transformers for satellite image time series classification. *IEEE Journal of Selected Topics in Applied Earth*

Observations and Remote Sensing, *14*, 474–487. https://doi.org/10.1109/JSTARS.2020.3036602

Yue, X., Zhao, Z., & Hu, K. (2026). Estimating economic activity from satellite embeddings. *Applied Sciences*. https://doi.org/10.3390/app16020582

Zanaga, D., Kerchove, R. V. D., Daems, D., Keersmaecker, W. D., Brockmann, C., Kirches, G., Wevers, J., Cartus, O., Santoro, M., Fritz, S., Lesiv, M., Herold, M., Tsendbazar, N.-E., Xu, P., Ramoino, F., & Arino, O. (2022). *Esa worldcover 10 m 2021 v200* [Data set]. https://doi.org/10.5281/zenodo.7254221

Zbontar, J., Jing, L., Misra, I., LeCun, Y., & Deny, S. (2021). *Barlow twins: Self-supervised learning via redundancy reduction* [Preprint]. arXiv. https://doi.org/10.48550/arxiv.2103.03230

Zhang, Z., Zhao, T., Guo, Y., & Yin, J. (2024). Rs5m and georsclip: A largescale vision-language dataset and a large vision-language model for remote sensing. *IEEE Transactions on Geoscience and Remote Sensing*. https://doi.org/10.1109/tgrs.2024.3449154

Zheng, G., Li, X., Zhang, R.-H., & Liu, B. (2020). Purely satellite data–driven deep learning forecast of complicated tropical instability waves. *Science Advances*, *6*(29), eaba1482. https://doi.org/10.1126/sciadv.aba1482

Zhou, G., Qian, L., & Gamba, P. (2025). Advances on multimodal remote sensing foundation models for earth observation downstream tasks: A survey. *Remote Sensing*, *17*(21), 3532. https://doi.org/10.3390/rs17213532

Zhu, X. X., Xiong, Z., Wang, Y., Stewart, A. J., Heidler, K., Wang, Y., Yuan, Z., Dujardin, T., Xu, Q., & Shi, Y. (2026). On the foundations of earth foundation models. *Communications Earth & Environment*, *7*(1), 103. https://doi.org/10.1038/s43247-025-03127-x

Zvonkov, I., Tseng, G., Becker-Reshef, I., & Kerner, H. (2026). *Cropland mapping using geospatial embeddings*. https://openreview.net/forum?id=tqxUPNhQSI